

**Slurry Deposited Environmental and Thermal Barrier Coatings and Design of Microchannel Cooling System for Enhanced Efficiency of Gas Turbine Engine Application**



**Maria Sattar**

**MS Energy Systems Engineering- 00000118255**

**Session 2015-17**

**Supervisor**

**Prof. Dr. Zuhair S. Khan**

**U.S. Pakistan Center for Advanced Studies in Energy (USPCAS-E)**

**National University of Sciences and Technology (NUST), H-12,**

**Islamabad 44000, Pakistan**

**March 2018**

**Slurry Deposited Environmental and Thermal Barrier Coatings and Design of Microchannel Cooling System for Enhanced Efficiency of Gas Turbine Engine Application**



**By**

**Maria Sattar**

**Reg# 00000118255**

**Session 2015-17**

**Supervised by**

**Prof. Dr. Zuhair S. Khan**

**This Thesis is submitted to the US. Pakistan Center for Advanced Studies in Energy (USPCAS-E) NUST in partial fulfillment of the requirements for the degree of MASTER of SCIENCE in ENERGY SYSTEMS ENGINEERING**

**U.S. Pakistan Center for Advanced Studies in Energy (USPCAS-E)**

**National University of Sciences and Technology (NUST), H-12,**

**Islamabad 44000, Pakistan**

**March 2018**

# THESIS ACCEPTANCE CERTIFICATE

Certified that final copy of MS/MPhil thesis written by Miss Maria Sattar, (Registration No. 00000118255, of USPCAS-E NUST has been vetted by undersigned, found complete in all respects as per NUST Statues/Regulations, is free of plagiarism, errors, and mistakes and is accepted as partial fulfillment for award of MS/MPhil degree. It is further certified that necessary amendments as pointed out by GEC members of the scholar have also been incorporated in the said thesis.

Signature: \_\_\_\_\_

Name of Supervisor: Prof. Dr. Zuhair S. Khan

Date: \_\_\_\_\_

Signature (HoD): \_\_\_\_\_

Date: \_\_\_\_\_

Signature (Dean/Principal): \_\_\_\_\_

Date: \_\_\_\_\_

# Certificate

This is to certify that work in this thesis has been carried out by **Miss. Maria Sattar** and completed under my supervision in Advanced Energy Materials and Systems laboratory, US. Pakistan Centre for Advanced studies in Energy, National University of Sciences and Technology, H-12, Islamabad, Pakistan.

Supervisor:

\_\_\_\_\_

Prof. Dr. Zuhair S. Khan

USPCAS-E, NUST, Islamabad

GEC member # 1:

\_\_\_\_\_

Dr. Majid Ali

USPCAS-E, NUST, Islamabad

GEC member # 2:

\_\_\_\_\_

Dr. Saifullah-Awan

National Centre for Physics, Islamabad

HoD-USPCAS-E

\_\_\_\_\_

Prof. Dr. Zuhair S. Khan

USPCAS-E, NUST, Islamabad

A/Principal/ Dean

\_\_\_\_\_

Prof. Dr. Zuhair S. Khan

USPCAS-E, NUST, Islamabad

## **Acknowledgements**

All the thanks and gratitude to Almighty Allah for providing me this auspicious and esteemed opportunity and helped me across the endeavor, provided me guidance and patience to complete project.

After this, I am very grateful to my research supervisor Prof. Dr Zuhair S. Khan for offering me the opportunity between the years of August 2016-Oct 2017 at Advanced Energy Materials & Systems Lab, U.S. PCAS-E NUST Islamabad. His motivation, confidence, and valuable guidance helped me to accomplish and achieve the goal of project.

I would thankful to my GEC members Dr. Majid Ali (USPCASE-E) & Dr. Saifullah Awan (NCP) for their support and valuable comments during project. I would also thank to Dr. Naseem for providing Synthesis lab facilities for conducting experiments.

I would thank to Operators of Combined Lab, Mr. Qamaruddin & Engr. Naveed Ali. I would acknowledge the support of my lab fellows, PhD scholars and my friends to support me during hard times of research. I would like to thank my co-authors for their valuable support. My sincere thanks.

I would also acknowledge research supervisor at OSU, Dr. Brian Fronk for his guidance and valuable suggestion during Exchange visit at Oregon State University USA. I would also thank to Tabeel Jacob for his time, support and guidance. Special thanks to Meredith for her valuable suggestions during the preparation of my presentation and manuscript.

Finally, I would like to express my all love to my father to keep me motivated, energetic, and for all the trust. I would also thank to all my siblings for providing their support and encouragement. I would also express my deepest gratitude to my beloved mother (late).

Warm thanks also to the research students of Humanitarian Engineering and TEST lab OSU University for generously sharing their experiences and support during exchange visit at Oregon State University United States.

## Abstract

In this era, energy technologies are suitable to meet the challenges of fuel depletion and global warming. Energy generation from natural resources such as coal, natural gas, and oil is an approach to fulfill the electricity demand. Depletion of non-renewable resources put an emphasis to increase the efficiency of thermal power plants. Gas turbine engine efficiency can only be increased after increasing the inlet gas temperature and reducing the cooling air flow. These attributes originated the need of thermal management for the combustor section in terms of material selection, protective coating and cooling or heat removal systems. Ni superalloy i.e. Monel 400 is the conventional material that exhibits good mechanical properties, is a potential candidate for the manufacture of gas turbine engine components e.g. turbine blade, vanes, etc. High-temperature oxidation and diffusion of deleterious elements reduced their applicability in power and aerospace industry. C/SiC composites are the materials of today engine world because of lightweight, high density, low CTE, and high thermal conductivity. Since C/SiC has poor oxidation resistance against high-temperature, a composite engine design will facilitate us to achieve higher efficiencies to meet the energy demands. The environmental and thermal barrier coating (ETBC) is the technique to combat thermal degradation risk to increase the endurance of materials against high thermal exposure. In this study, oxidation protective shield of  $\text{Al}_2\text{O}_3$  was developed on Monel 400 superalloy and C/SiC composite via an easy and cost-effective slurry dip coating route instead of expensive thermal spray process. Slurry was prepared after employing solution method and deposited after using dip-coater. After deposition, coating was vacuum dried and sintered to consolidate the surface structure. In case of Monel 400 superalloy, Isothermal oxidation testing at 600°C, 800°C, and 1000°C for several hours was performed. Reduction in weight gain was observed. Analytical techniques such as XRD, SEM, EDS and image analysis were performed for analyzing the microstructure and microchemistry to analyze the thermal performance of coating. For  $\text{Al}_2\text{O}_3$  coated C/SiC composite, reduction in porosity before and after sintering was analyzed by Image J software. SurfChar J analysis measured effective surface roughness  $R_a$  of about 7-16  $\mu\text{m}$  with positive skewness and kurtosis. Coating with 8-15% surface porosity proved sustainable after performing dynamic thermal shock testing (DTS). During testing corresponding weight loss was measured. SEM based cross-sectional analysis depicts a well-established and adherent interface. Coating was remained intact

without spallation or peeling. Slurry deposited  $\text{Al}_2\text{O}_3$  protected the C/SiC composite from surface oxidation with weight loss in fraction.

As part of exchange program at MIME (TEST lab), Oregon State University, research work was carried out on condensation across microchannels. For cooling of combustion section, an innovative microchannel cooling system at low mass fluxes  $75\text{-}150\text{kg/m}^2\text{-s}$  at saturation temperature of  $40^\circ\text{C}$  and  $55^\circ\text{C}$  for efficient heat transfer was studied. The study focused to analyze the transition of flow regimes and vapor quality at low mass fluxes. The experiments were performed at low mass fluxes  $75\text{-}150\text{kg/m}^2\text{-s}$  at saturation temperature of  $40^\circ\text{C}$  and  $55^\circ\text{C}$ . For all conditions, annular /annular wavy flow regimes observed, with no distinct intermittent flow. The experimental data was compared against the two-phase flow map of Taitel and Duckler which shows good agreement for condensation of R134a.

**Keywords: Gas Turbines, Monel 400 superalloy, C/SiC, ETBCs, Microchannel, Surface Roughness, DTC**

# Table of Contents

<b>Acknowledgements</b> .....	v
<b>Abstract</b> .....	vi
<b>List of Figures</b> .....	xii
<b>List of Tables</b> .....	xiv
<b>List of Journals</b> .....	xv
<b>Chapter 1</b> .....	16
<b>1. Introduction</b> .....	16
<b>1.1 Background</b> .....	16
<b>1.3. Materials for Hot Section Components of Gas Turbine Engine</b> .....	18
<b>1.3.1. Ni-Superalloy</b> .....	19
<b>1.3.2. C/SiC Composites</b> .....	20
<b>1.4. Research at Oregon State University</b> .....	20
<b>1.6. Microchannel heat transfer technology</b> .....	21
<b>References</b> .....	24
<b>Chapter 2</b> .....	28
<b>Why Environmental and thermal barrier coatings and Microchannel cooling system for gas turbine engine</b> .....	28
<b>2.1. Environmental and Thermal barrier coatings (ETBCs)</b> .....	28
<b>2.1.1. Bond Coat</b> .....	28
<b>2.1.2. Top coat</b> .....	29
<b>2.1.3 Key features of protective coatings system</b> .....	30
<b>2.2. Materials for ETBCs</b> .....	30
<b>2.3. Corundum or Alumina as ETBCs material</b> .....	31
<b>2.4. Microchannel Cooling System</b> .....	32
<b>2.4.1. Understanding of flow patterns</b> .....	33



<b>2.5. Problem Statement</b> .....	34
<b>2.6. Objectives of Study</b> .....	35
<b>Thesis Flow Chart</b> .....	36
<b>Summary</b> .....	37
<b>References</b> .....	38
<b>Chapter 3</b> .....	42
<b>Mechanism of Mass change in C/SiC Composite at high temperature sintering</b> .....	42
<b>3.1. Mode of C/SiC Oxidation</b> .....	42
<b>3.2. Antioxidation behavior with Thermal barrier Coatings</b> .....	43
<b>3.3. Effect of sintering at 1073K</b> .....	44
<b>Summary</b> .....	48
<b>References</b> .....	49
<b>Chapter 4</b> .....	51
<b>Development of slurry deposited ETBCs &amp; Designing of Microchannel</b> .....	51
<b>4.1. Substrate preparation</b> .....	51
<b>4.1.1. C/SiC Composite Slicing</b> .....	51
<b>4.1.2. Monel 400 Superalloy Sectioning</b> .....	52
<b>4.2. Surface preparation</b> .....	52
<b>4.2.1. Monel 400 Superalloy Surface preparation</b> .....	52
<b>4.2.2. C/SiC composite Surface preparation</b> .....	52
<b>4.3. Slurry Preparation</b> .....	53
<b>4.3.1. Rheology Properties of Slurry</b> .....	54
<b>4.4. Deposition of Alumina slurry</b> .....	54
<b>4.5. Heat Treatment/Curing/Sintering of coating</b> .....	55
<b>4.6. Sample Preparation for SEM Analysis</b> .....	56

<b>4.7. Isothermal Oxidation Testing</b> .....	56
<b>4.8. Thermal Shock Testing</b> .....	56
<b>4.9. Phase stability, microstructure and image analysis</b> .....	57
<b>4.9.1. Image J analysis for porosity, surface roughness, and coating thickness</b> .....	57
<b>4.10. Experimental Approach</b> .....	59
<b>4.10.1. Test Section Design</b> .....	59
<b>4.10.2. Refrigerant and Water Loops</b> .....	60
<b>4.11. Condensation system</b> .....	61
<b>4.12. Experimental Methods and Analysis</b> .....	62
<b>4.12.1. Heat transfer model</b> .....	64
<b>4.12.2. Two-Phase flow model</b> .....	65
<b>Summary</b> .....	66
<b>References</b> .....	67
<b>Chapter 5</b> .....	69
<b>Oxidation kinetics and microstructure analysis of slurry deposited alumina on Monel 400 Superalloy</b> .....	69
<b>5.1. Isothermal oxidation testing</b> .....	69
<b>5.2 XRD analysis</b> .....	70
<b>5.3 SEM analysis</b> .....	71
<b>5.4 Discussion</b> .....	73
<b>5.5 Thermal conductivity, porosity and pore distribution</b> .....	76
<b>References</b> .....	80
<b>Chapter 6</b> .....	83
<b>Thermal shock testing and microstructure analysis of slurry deposited alumina on C/SiC composite</b> .....	83
<b>6.1. Characteristics of as-deposited Al<sub>2</sub>O<sub>3</sub> coating</b> .....	83

<b>6.2. Characterization study of Al<sub>2</sub>O<sub>3</sub> Coating</b> .....	84
6.2.1. Sintering at 800°C for the densification of coating.....	84
<b>6.3. XRD analysis of powder and Sintered coating</b> .....	86
6.3.1. Effect of sintering on the microstructure of coating.....	86
<b>6.4. SEM analysis of Alumina coating</b> .....	87
<b>6.4. Thermal shock resistance of Al<sub>2</sub>O<sub>3</sub> coating</b> .....	90
<b>Summary</b> .....	93
<b>References</b> .....	95
<b>Chapter 7</b> .....	97
<b>Microchannel Heat Transfer</b> .....	97
<b>7.1. Flow Regimes at Saturation Temperature 40°C</b> .....	97
7.1.1 Barnea Two-Phase Flow Regime.....	97
7.1.2. Breber Two-Phase Flow Regime.....	98
<b>7.2. Flow Regimes at Saturation Temperature 55°C</b> .....	99
7.2.1. Barnea Two-Phase Flow Regime.....	100
7.2.2. Breber Two-Phase Flow Regime.....	101
<b>References</b> .....	104
<b>Chapter 8</b> .....	106
<b>8.1. Conclusion</b> .....	106
<b>8.2. Future Recommendations</b> .....	108
<b>References</b> .....	<b>Error! Bookmark not defined.</b>
<b>Annexure I</b> .....	<b>Error! Bookmark not defined.</b>
<b>Annexure II</b> .....	1

# List of Figures

Figure 1.1: Share of hydro and thermal power in national power generation	16
Figure 1.2: The evolution of gas turbine materials and thermal management for operating at High-Temperature (Source: Wadley Research Group – UVA)	18
Figure 2.1: Cross sectional description of TBCs coatings for high-temperature application	29
Figure 2.2: Thesis flow for the study	36
Figure 3.1: Schematic illustration of oxidation mechanism during high temperature sintering of alumina coated C/SiC composite.	46
Figure 4.1: Low-speed diamond saw in Advanced Energy Materials and Systems lab	51
Figure 4.2: Schematic for Alumina slurry preparation	54
Figure 4.3: Camera image of alumina slurry: Magnetically stirred at 60 rpm for 6 hrs.	54
Figure 4.4: a) Alumina slurry deposition via dip coating by using dip coater at C/SiC composite coupon, b) camera images of dip-coated substrate after overnight drying at room temperature	55
Figure 4.5: Flow diagram showing methodology for image analysis	58
Figure 4.6: Schematic of test facility	62
Figure 4.7: a) Schematic of test section, b) Photograph of uninsulated test section	63
Figure 5.1: Weight gain curve for uncoated and Al <sub>2</sub> O <sub>3</sub> coated Monel 400 alloy substrate with a surface area of 5.625 cm <sup>2</sup> . Duration of each cycle was 3 h.	69
Figure 6.1: a) Camera image of C/SiC composite coupon before slurry deposition; (b) SEM image of uncoated C/SiC composite coupon; (c) camera image of coated coupon; (d) inset is of as-deposited Al <sub>2</sub> O <sub>3</sub> coating vacuum dried at 250°C;	83
Figure 6.2: a) Al <sub>2</sub> O <sub>3</sub> particles before sintering, b) After sintering at 800°C, grain boundary shift	85
Figure 6.3: SEM micrograph and image analysis description of Al <sub>2</sub> O <sub>3</sub> coated coupon; a) After sintering at 800°C for 3 hrs. in static air (1-2) EDS analysis after sintering;	85
Figure 6.4: Mass change rate after air-sintering of Alumina-coated C/SiC composite at 1073 K for 3 h	86
Figure 6.5: XRD spectra of Al <sub>2</sub> O <sub>3</sub> coating (a) before and (b) after sintering at 1073 K	87
Figure 6.6: SEM image of (a) C/SiC; (b) As-deposited coating; (c) cross-section of sintered coating sintered coating, and (d) EDS spectra of alumina coating after sintering	87
Figure 6.7: SEM image, binary image, and surface plot of the: (a-c) as-deposited coating; (d-f)	89

Figure 6.8: Microstructure analysis of thermal shock tested Al <sub>2</sub> O <sub>3</sub> coated C/SiC specimen via SEM and ImageJ analysis: (a) SEM after 5 thermal cycles; (b) SEM image; (c) binary image (50 μm); (d) surface plot; (e) EDS analysis; after 26 thermal shock cycles respectively.	93
Figure 7.1: Comparison to Barnea et al. flow map for R134a at 40°C in 0.84mm channel	98
Figure 7.2: Comparison to Breber et al. flow map for R134a at 40°C in 0.84mm channel	99
Figure 7.3: Comparison to Barnea et al. flow map for R134a at 55°C	101
Figure 7.4: Comparison to Breber et al. flow map for R134a at 55°C in 0.84mm channel	102
Figure 7.5: Comparison of visualization data $G=100 \text{ Kg/m}^{-2} \text{ s}^{-1}$ , $T_{\text{sat}} = 40^\circ\text{C}$ , comparison of three different qualities	102
Figure 7.6: Comparison of visualization data $G=100 \text{ Kg/m}^{-2} \text{ s}^{-1}$ , $x=0.2$ at two saturation temperatures, comparison of three different qualities	103

## List of Tables

Table 2.1: Thermal properties of materials for gas turbines:	31
Table 3.1: Reported sintering temperature for Environmental and thermal barrier coatings	45
Table 4.1: Manual grinding of C/SiC composite for slurry deposition	53
Table 4.2: Test matrix for R134a condensation study	63
Table 7.1: Experimental results for flow visualization at 40°C saturation temperature	97
Table 7.2: Experimental results for flow visualization at 55°C saturation temperature	100

## List of publications

1- Authors: **Maria Sattar**, Mariah Batool, Zuhair S. Khan\*

Oxidation protection study for Monel 400 Superalloy via slurry deposition of Al<sub>2</sub>O<sub>3</sub> coating for gas turbine engine application” Presented in Conference “NanoSET 2017”.

Submitted to supervisor

2- Authors: **Maria Sattar**, Mariah Batool, Ijaz Tahir, Zuhair S. Khan\*

Al<sub>2</sub>O<sub>3</sub>-coated C/SiC composite for gas turbine applications: Thermal shock testing and microstructural analysis,

Submitted to supervisor

---

<sup>1</sup>Attached as Annexure I

<sup>2</sup>Attached as Annexure II

# Chapter 1

## 1. Introduction

### 1.1. Background

In present energy scenario of Pakistan, it aims to promote local manufacturing industry in Pakistan. Renewable energy technologies can only be adopted by reducing the costs associated with the manufacturing process of power plant infrastructure e.g. heat engines, gas turbines, etc. or repairing of defective parts. The production of engine parts or at least repairing of damaged parts should be carried out locally that can be helpful in establishing Pakistan manufacturing Industry.

Gas turbines have been in use for stationary electric power generation since the late 1930s. Turbines went on to revolutionize airplane propulsion in the 1940s, and since the 1990s through today, they have been a popular choice for new power generation plants in the United States. Gas turbines are also available in sizes ranging from 500 kilowatts (kW) to more than 300 megawatts (MW) for both power-only generation and combined heat and power (CHP) systems [1].

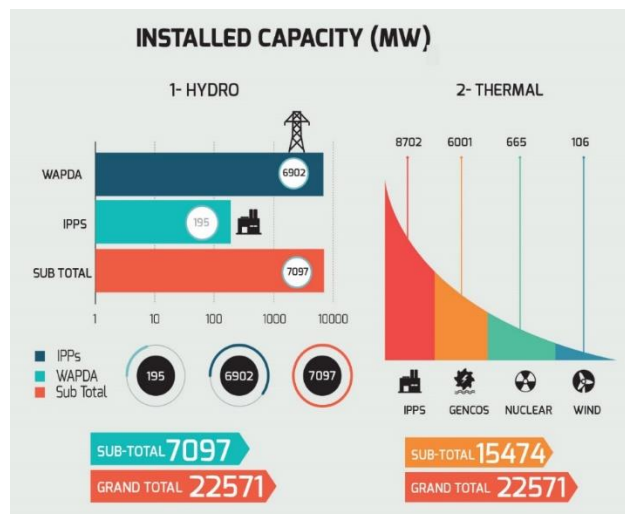


Figure 1.1: Share of hydro and thermal power in national power generation



The current generation of energy technologies focused on developing efficient and reliable energy infrastructure for efficient utilization of renewable and non-renewable energy resources. Technology upgrade propels the need of novel technology to increase the energy yield in electric and thermal prospects. Gas turbine engine is an efficient way of electrical and thermal energy generation. Present and upcoming demand of energy can only be meet after increasing the efficiency of gas turbine engine. Gas turbine engine a cheapest way of electricity generation needs to be efficient regarding GHGs emission and high fuel consumption. The efficiency of a gas turbine engine directly related with the inlet gas temperature [2]. High inlet temperature reduced the working life of gas turbine engine due to the degradation of the hot section component's e.g. turbine blade, nozzle, vane [3][4].

## **1.2. Gas turbine Engine**

Gas turbine engine as likely internal combustion engine in which working fluid flows continuously instead of occasionally. It converts the chemical energy of fuel into mechanical energy that serves as a mechanical power/drive for industrial applications as well as high thrust for aerospace industry and nuclear power plants [8]. Advances in gas turbine engine technology promoted its flexibility for power generation and for tolerating high thrust load in the aviation industry. Higher efficiencies, low fuel consumption, and reduced emissions are major challenges to address for gas turbine engine. In past decade, the major focus of engineers and researchers is to increase the inlet gas temperature, higher the temperature higher will be the efficiency. While operating temperature in combustion chamber of gas turbine  $\geq 1930$  °C, directly instigated the risk of gas turbine blade failure. When hot gas approaches the turbine blade section, it reduced to 1600-1700°C because of primary internal cooling passages in an aerospace engine. Still, yet such High-Temperature is beyond the endurance limit of turbine blade material [9].

Thermal exposure failure risk originated the concept of thermal management for gas turbine engine [10] which comprised of materials selection for turbine components e.g. blade and vane, internal convective cooling, external film cooling (surface), thermal barrier coatings, thermal & mechanical design, and choice of the coolant fluid [11], [12]. High-temperature challenge imposes the search of state-of-art materials for manufacturing of gas turbine engine

components, those can efficiently survive when exposed to the thermal environment. For the safeguard of base material from the harm of thermal environment, insulation by thermal barrier coatings and provision of internal cooling channels cast inside the base material are preferred approaches. In corresponding to material selection, opted material should have good mechanical strength and capable of the enduring aggressive thermochemical environment [12].

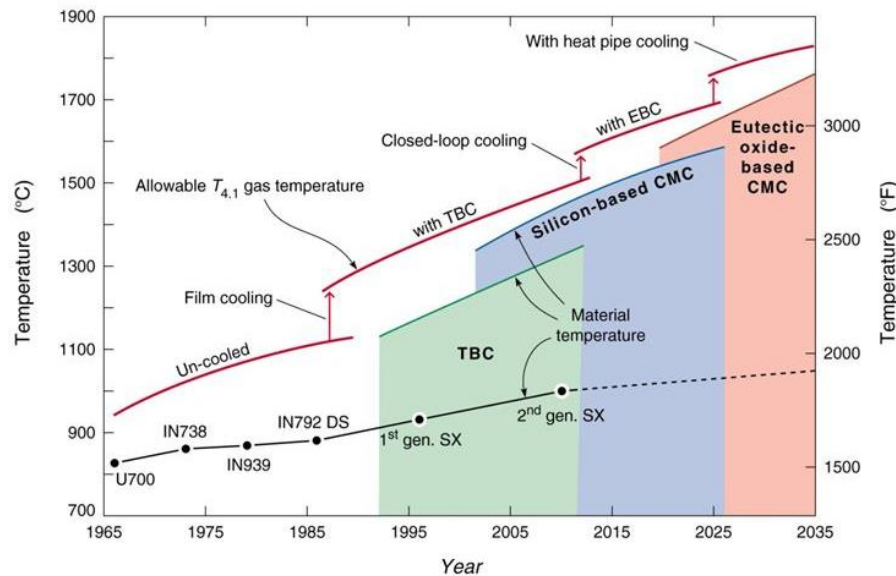


Figure 1.2: The evolution of gas turbine materials and thermal management for operating at High-Temperature (Source: Wadley Research Group – UVA)

### 1.3. Materials for Hot Section Components of Gas Turbine Engine

The conventional material used for gas turbine engine components was Ni-based superalloys, due to their stability in harsh environments, high heat resistance, corrosion, and acid resistance. However, at a temperature above than 1300°C, Ni-based superalloys have low creep resistance, poor phase stability and can't withstand thermal oxidation. To overcome these challenges, researchers are investigating advanced materials such as C/SiC composite as a potential candidate material for gas turbine engine hot section [13],[14]. Carbon fiber reinforced Silicon carbide matrix (C/SiC) composites are the state of the art material for hot section components of gas turbine engines. C/SiC composite exhibits distinct features such as high mechanical strength, high fracture toughness, low density, high hardness, high thermal conductivity and low coefficient of thermal expansion at High-Temperature [5][6]. Meanwhile, it has very poor

oxidation resistance as temperature goes above  $>400^{\circ}\text{C}$  which questioned its application in aerospace and power industry [3][7].

Thermal exposure to metallic components e.g. turbine blades reduced the component's workability due to thermal degradation. The high operating temperature caused environmental degradation of materials and deteriorating the mechanical properties which have its effect in shortening the lifetime of metallic components. Thermal and environmental concerns raise the modification of hot section components of high-temperature gas turbines [15]. Literature reported that; improved design [16] optimum efficiency and reducing emissions, are the main driving forces that originated the search of such materials those should be environmentally as well as thermally stable. Technology advances regarding materials, coatings, and cooling aspects are required to reach higher inlet temperatures [10].

### **1.3.1. Ni-Superalloy**

Ni-based superalloys are the most used material in industry for gas turbine components e.g. Blades, turbine disc, vanes etc. Because Ni superalloy can withstand harsh environments, and exhibit high heat resistance, corrosion resistance, and acid resistance, they are supreme materials for use in turbines and assemblies in the marine, chemical processing, oil and gas, aerospace and military industries.

Ni-base superalloys are the conventional material for the manufacturing of gas turbine and combustor's components operating at medium-High-Temperature. Oxidation and microstructure degradation at High-Temperature is still a challenge to address in consideration of Ni-Super alloy. Monel 400 superalloy in the class of Ni-base superalloy is the conventional material for gas turbine engine with the operating range of  $600-900^{\circ}\text{C}$  [17]. Monel 400 superalloy has its applications for steam generators, boiler components, nuclear reactors and fossil fuels thermal plants [18][17]. However, its high-temperature risk to oxidation and creep-fatigue limits its application in energy spectrum. Monel 400 superalloy needs thermal barrier coating that can protect it from the harm of high-temperature oxidation and corrosion under air atmosphere. Provision of TBCs can raise the working temperature above than melting point of Monel 400 superalloy [4].

### **1.3.2. C/SiC Composites**

C/SiC composite as a potential candidate material for gas turbine engine hot section [13],[14]. C/SiC composite exhibits high strength, good toughness, extremely high creep resistance, and good mechanical and environmental stability with a low coefficient of thermal expansion(CTE) that catalyze their applicability and lifetime [5], [21],[6]. The only thing that encumbers the C/SiC composite acceptance is their susceptibility to high-temperature oxidation as temperature goes beyond 400°C[22]. To combat this challenge, oxidation protective coatings are provided on external surfaces to reduce the oxidation of C/SiC composite.

The availability of protective coatings on Ni-super alloy and C/C-SiC composites resulted in protection of materials and turbine components against the detrimental risk of the environment [19] and act as a thermal shield against abrasion [20]. The usage of only 0.2mm thick ceramic thermal barrier coatings of low thermal conductivity can reduce the surface temperature of turbine blades about 100 to 150°C. Thermal barrier coatings can reduce the specific fuel consumption of about 2 to 3 % and a corresponding reduced emission in aerospace engines. The development of environmentally and thermally stable coatings (E/TBCs) is a necessity to cope the present challenges.

### **1.4. Research at Oregon State University**

Research at Oregon State University was based on studying the heat transfer during Two-Phase condensation of R-134a inside the micro-channels. Provision of micro-channels for the efficient heat transfer is a novel technology to increase the heat removal. Project objective was focused on formulating a database for future research regarding microchannel. There is no database available for heat transfer through the micro-channels. Internal cooling is provided with TBC system to further remove the heat before it starts the oxidation of base material [23] . Pinhole and hollow spaces are the approaches for developing heat sink inside the combustion chamber of gas turbine engine. For inlet temperature up-to 1500-1700°C, there is need of efficient heat transfer through cooling ways besides with thermal barrier coating system. Provision of micro-channels inside the turbine blades, vanes etc. will increase the heat transfer due to high surface area to volume ratio. Along this, this will reduce the weight of gas turbine engine.

## 1.5. Microchannel heat transfer technology

Predicting condensation two-phase flow regimes and the associated heat transfer and pressure drop in microchannels is critical for designing advanced heating, cooling, and refrigeration systems. It is well established that at small hydraulic diameters, the two-phase flow morphology deviates from that predicted for larger tubes at equivalent operating conditions. Namely, the importance of gravity dominated flow regimes including stratified and wavy flow decrease, while the preponderance of intermittent, slug-and- plug type flow increase [24]–[29]. In addition, it has been shown that flow maps and transition criteria developed for air/water flows do not yield good predictive capability for low surface tensions fluids such as R-134a [30].

Understanding the prevailing flow regime for condensing refrigerants is important for developing mechanistic models to predict heat transfer and pressure drop. In an attempt to characterize condensation flow regimes, there have been numerous qualitative and quantitative studies using high-speed visualization, capacitance, and other measurement techniques. Doretto et al. provided a review of condensation flow patterns inside plain and microfin tubes (all sizes) and found wide scatter in the data despite a large volume of archival literature [31]. For small channels, flow regime visualization for condensation of refrigerants is even more limited [27], [28], [30]. On the other hand, boiling/evaporation studies of flow regimes of refrigerants in mini/microchannels are more prevalent [31], [32]. However, caution should be used when extrapolating these results to condensation, as the flow regimes are influenced by the heating boundary condition. This is particularly true for boiling/evaporation where nucleating bubbles can be confined within mini/microchannels.

Most of the available work of mini/microchannel flow regime mapping has focused on adiabatic, air/water flows at relatively high superficial velocities or condensing/evaporating refrigerants, at large mass fluxes ( $G > 150 \text{ kg m}^{-2} \text{ s}^{-1}$ ). While these mass fluxes may be realistic for high-flux electronics cooling (i.e., short flow lengths), they are not representative of the flow conditions for high heat duty microchannel condensers in heating, cooling, and power generation. These applications are generally characterized by heat exchangers with multiple parallel microchannels with relatively low mass flux to effectively transfer heat while minimizing frictional pressure loss [33]–[42].

Thus, the objective of this study was to investigate flow regimes and the predictive capability of different flow maps for condensing refrigerants in small channels at low mass fluxes.

Qualitative flow regime data were obtained from high-speed visualization of condensing flows at nominal mass fluxes from 75 to 150 kg m<sup>-2</sup> s<sup>-1</sup> for a quality from 0.1 to 0.8 of R-134a in parallel rectangular microchannels ( $D_h = 0.84$  mm). Initially, superheated R-134a was distributed into multiple parallel microchannels and then condensed to the desired quality prior to the inlet of a visualization section. This experimental arrangement mitigates the potential for flow maldistribution and provides a more realistic simulation of what would happen inside an actual condenser. Despite the very small heat duties, a low uncertainty in the inlet quality is maintained by enforcing a large temperature difference on the water-side ( $\Delta T > 10$  K). Finally, the data were compared to flow regime maps from the literature.

R-134a was chosen as a working fluid due to its prevalence in the HVAC&R industry and the availability of prior work using this fluid. R-134a is in the process of being phased down due to its high global warming potential (GWP). However, the thermophysical properties are comparable to new low GWP replacements such as R-1234yf and R-513A, providing some confidence that the results of this study can be extended to new refrigerants.

## **Summary**

In this chapter, we introduced with gas turbine engine, evolution in engine technology and materials for gas turbine engine. We have also with the high-temperature challenges associated with rising demand of engine efficiency for fulfill the energy demand of civilizations. Cooling technologies regarding thermal barrier coating, internal cooling, pinholes and external cooling are discussed here. Overview of current energy technologies was taken to get how know about the clear picture of challenges. The possible solutions are suggested in the light of literature to resolve the high risk of base material oxidation at high-temperature.

## References

- [1] “Demystifying Pakistan’s Energy Crisis.” .
- [2] F. O. Soechting, “A Design Perspective on Thermal Barrier Coatings,” *J. Therm. Spray Technol.*, vol. 8, no. December, pp. 505–511, 1999.
- [3] C. Courtois, J. Desmaison, H. T, and S. E. E. S. Cedex, “Protection against oxidation of C / SiC composites : oxidation behaviour of CVD TiB<sub>2</sub> coated substrates,” *J. Phys. Iv*, vol. 3, 1993.
- [4] J. D. Osorio, A. Toro, and J. P. Hernandez-Ortiz, “Thermal barrier coatings for gas turbine applications: failure mechanisms and key microstructural features,” *Dyna*, vol. 79, no. 176, pp. 149–158, 2012.
- [5] A. Wank *et al.*, “Diffusion barrier coatings for graphite , C / C and C / SiC racks in vacuum heat treatment or High-Temperature brazing processes,” pp. 5–8, 2005.
- [6] B. Zou *et al.*, “Microstructure, oxidation protection and failure mechanism of Yb<sub>2</sub>SiO<sub>5</sub>/LaMgAl<sub>11</sub>O<sub>19</sub> coating deposited on C/SiC composites by atmospheric plasma spraying,” *Corros. Sci.*, vol. 62, pp. 192–200, 2012.
- [7] W. Q. Xiang Yang\* , Cao Feng, “ZrB<sub>2</sub>-SiC as a protective coating for C/SiC composites: Effect of High-Temperature oxidation on thermal shock property and protection mechanism.” *Journal of Asian Ceramic Societies*, pp. 159–163, 2016.
- [8] C. a Estrada, “New Technology Used in Gas Turbine Blade Materials .,” *Sci. Tech. Año XIII*, no. 36, pp. 297–301, 2007.
- [9] “FUNDAMENTALS OF GAS TURBINE ENGINES.”
- [10] G. Turbines and K. N. Lee, “Protective Coatings for Gas Turbines 4.4.2-1 Introduction,” pp. 419–437.
- [11] R. S. Bunker, “Innovative gas turbine cooling techniques.”
- [12] A. C. Karaoglanli, K. Ogawa, A. Türk, and I. Ozdemir, *Thermal Shock and Cycling*



- Behavior of Thermal Barrier Coatings (TBCs) Used in Gas Turbines*. Intech, 2014.
- [13] K. Singh, "Advanced Materials for Land Based Gas Turbines," *Trans. Indian Inst. Met.*, vol. 67, no. 5, pp. 601–615, Oct. 2014.
- [14] R. J. E. Glenny, J. E. Northwood, and a. B. Smith, "Materials for Gas Turbines," *Int. Mater. Rev.*, vol. 20, no. 1, pp. 1–28, 1975.
- [15] Y. Tamarin, *Protective Coatings for Turbine Blades*. ASM International, 2002.
- [16] F. O. Soechting, "A design perspective on thermal barrier coatings," Oct. 1995.
- [17] D. C. June and J. D. Whittenberger, "NASA TM X-3065 HIGH-TEMPERATURE MECHANICAL PROPERTIES OF A ZIRCONIUM-MODIFIED , NICKEL - 30 PERCENT COPPER ALLOY by John D . Whittenberger," no. June, 1974.
- [18] K. D. Ramkumar, N. Arivazhagan, S. Narayanan, and D. Mishra, "Hot Corrosion Behavior of Monel 400 and AISI 304 Dissimilar Weldments Exposed in the Molten Salt Environment Containing Na<sub>2</sub>SO<sub>4</sub> + 60 % V<sub>2</sub>O<sub>5</sub> at 600 °C . Experimental Procedure," *Mater. Res.*, vol. 17, no. 5, pp. 1273–1284, 2014.
- [19] I. of M. R. at the G. A. Center, "Institute of Materials Research." Institute of Materials Research at the German Aerospace Center.
- [20] X. Yang, L. Wei, W. Song, Z. Bi-feng, and C. Zhao-hui, "ZrB<sub>2</sub>/SiC as a protective coating for C/SiC composites: Effect of High-Temperature oxidation on mechanical properties and anti-ablation property," *Compos. Part B Eng.*, vol. 45, no. 1, pp. 1391–1396, Feb. 2013.
- [21] *Ceramic Fibers and Coatings*. Washington, D.C.: National Academies Press, 1998.
- [22] A. Z. Abidin *et al.*, "EVALUATION OF ALUMINA AS PROTECTIVE COATING FOR CARBON FIBERS IN MAGNESIUM-BASED COMPOSITES," 2015.
- [23] P. Prapamonthon, H. Xu, W. Yang, and J. Wang, "Numerical Study of the Effects of Thermal Barrier Coating and Turbulence Intensity on Cooling Performances of a Nozzle Guide Vane," *Energies*, vol. 10, no. 3, p. 362, 2017.

- [24] M. A. Vanderputten, T. A. Jacob, M. Sattar, N. Ali, and B. M. Fronk, “Two-phase flow regimes of condensing R-134a at low mass flux in rectangular microchannels,” *Int. J. Refrig.*, vol. 84, pp. 92–103, Dec. 2017.
- [25] M. A. Vanderputten, T. A. Jacob, M. Sattar, N. Ali, and B. M. Fronk, “Two-phase flow regimes of condensing R-134a at low mass flux in rectangular microchannels,” *Int. J. Refrig.*, vol. 84, pp. 92–103, Dec. 2017.
- [26] A. Cavallini, G. Censi, D. Del Col, L. Doretti, G. Longo, and L. Rossetto, “Condensation of Halogenated Refrigerants Inside Smooth Tubes,” *HVAC&R Res.*, vol. 8, no. 4, pp. 429–451, Oct. 2002.
- [27] E. Rahim, R. Revellin, J. Thome, and A. Bar-Cohen, “Characterization and prediction of two-phase flow regimes in miniature tubes,” *Int. J. Multiph. Flow*, vol. 37, no. 1, pp. 12–23, Jan. 2011.
- [28] J. W. Coleman and S. Garimella, “Two-phase flow regimes in round, square and rectangular tubes during condensation of refrigerant R134a,” *Int. J. Refrig.*, vol. 26, no. 1, pp. 117–128, Jan. 2003.
- [29] C.-Y. Yang and C.-C. Shieh, “Flow pattern of air–water and two-phase R-134a in small circular tubes,” *Int. J. Multiph. Flow*, vol. 27, no. 7, pp. 1163–1177, Jul. 2001.
- [30] C. L. Ong and J. R. Thome, “Macro-to-microchannel transition in two-phase flow: Part 1 – Two-phase flow patterns and film thickness measurements,” *Exp. Therm. Fluid Sci.*, vol. 35, no. 1, pp. 37–47, Jan. 2011.
- [31] J. R. Thome, “Boiling in microchannels: a review of experiment and theory,” *Int. J. Heat Fluid Flow*, vol. 25, no. 2, pp. 128–139, Apr. 2004.
- [32] C. B. Tibiriçá and G. Ribatski, “Flow boiling in micro-scale channels – Synthesized literature review,” *Int. J. Refrig.*, vol. 36, no. 2, pp. 301–324, Mar. 2013.
- [33] B. M. Fronk and K. R. Zada, “Evaluation of Heat and Mass Transfer Models for Sizing Low-Temperature Kalina Cycle Microchannel Condensers,” *J. Energy Resour. Technol.*, vol. 139, no. 2, p. 22002, Aug. 2016.

- [34] N. Asok Kumar and S. R. Kale, "Numerical simulation of steady state heat transfer in a ceramic-coated gas turbine blade," *Int. J. Heat Mass Transf.*, vol. 45, no. 24, pp. 4831–4845, 2002.
- [35] T. Harirchian and S. V. Garimella, "A comprehensive flow regime map for microchannel flow boiling with quantitative transition criteria," *Int. J. Heat Mass Transf.*, vol. 53, no. 13–14, pp. 2694–2702, 2010.
- [36] R. Suliman, L. Liebenberg, and J. P. Meyer, "Improved flow pattern map for accurate prediction of the heat transfer coefficients during condensation of R-134a in smooth horizontal tubes and within the low-mass flux range," *Int. J. Heat Mass Transf.*, vol. 52, no. 25–26, pp. 5701–5711, 2009.
- [37] J. El Hajal, J. R. Thome, and A. Cavallini, "Condensation in horizontal tubes, part 1: Two-phase flow pattern map," *Int. J. Heat Mass Transf.*, vol. 46, no. 18, pp. 3349–3363, 2003.
- [38] M. K. Akbar, D. A. Plummer, and S. M. Ghiaasiaan, "On gas-liquid two-phase flow regimes in microchannels," *Int. J. Multiph. Flow*, vol. 29, no. 5, pp. 855–865, 2003.
- [39] C. Y. Yang and C. C. Shieh, "Flow pattern of air-water and two-phase R-134a in small circular tubes," *Int. J. Multiph. Flow*, vol. 27, no. 7, pp. 1163–1177, 2001.
- [40] G. El Achkar, M. Miscevic, P. Lavieille, J. Lluc, and J. Hugon, "Flow patterns and heat transfer in a square cross-section micro condenser working at low mass flux," *Appl. Therm. Eng.*, vol. 59, no. 1–2, pp. 704–716, 2013.
- [41] J. A. Milkie, S. Garimella, and M. P. Macdonald, "Flow regimes and void fractions during condensation of hydrocarbons in horizontal smooth tubes," *Int. J. Heat Mass Transf.*, vol. 92, pp. 252–267, 2016.
- [42] G. Nema, S. Garimella, and B. M. Fronk, "Flow regime transitions during condensation in microchannels," *Int. J. Refrig.*, vol. 40, pp. 227–240, 2014.

# Chapter 2

## Why Environmental and thermal barrier coatings and Microchannel cooling system for gas turbine engine

### 2.1. Environmental and Thermal barrier coatings (ETBCs)

Environmental and Thermal barrier coatings (ETBCs) can help the C-Composite to resist against thermos-chemical environment along with providing mechanical strength to the turbine component. Recent advances in turbine engine operating temperature is possible by depositing ETBCs on high- temperature gas turbine components. Usually, ETBCs are thick coatings of refractory oxides with a thickness of about 100  $\mu\text{m}$  -2 mm. These coatings enable the base material at hot temperature section of turbine engine to work above than their melting point. Functionality of thermal barrier coatings (ETBCs) mainly depends on the thermal conductivity, coefficient of thermal expansion, and phase stability from room temperature to hot gas temperature. It has been observed that 50% decrease in thermal conductivity drop the temperature about 55°C for single crystal Ni-based Super alloy [19]. Mostly ETBCs structure comprised of bond coat and overlay coat/wash coat.

#### 2.1.1. Bond Coat

Material for bond coat is typically thermal resistant material that at High-Temperature give production of thermally grown oxide. Usually, metallic bond coat is preferred for TBCs as it improves the bonding between ceramic topcoat and substrate material.

In 1950s, first enamel coating as TBCs application was manufactured for military engine components. In 1960s the first flame sprayed NiAl bond coats with ceramic top coat was used as thermal barrier coating for aero engines. In mid-1970s, thermal barrier coatings on Ni-Super alloy were first successfully applied in a research turbine engine. Further advances in early 1980s possible the manufacture of TBCs on vane and blade surfaces that commercialized the technology[1][2].

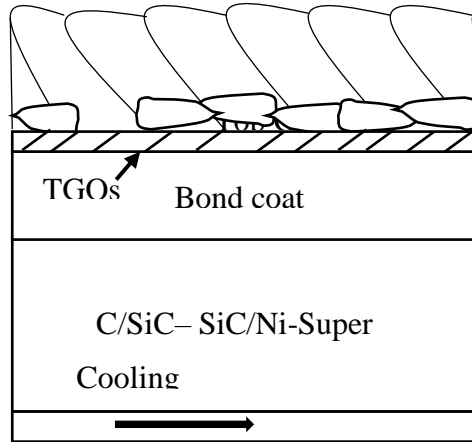


Figure 2.1: Cross sectional description of TBCs coatings for high-temperature application

Instead of High-Temperature, combustion environment is another challenge for hot section of turbine engine. At High-Temperature, Ni-based Super alloys lose their mechanical strength due to low creep resistance as compared to carbon composite. Carbon fiber reinforced silicon carbide composite due to low coefficient of thermal expansion and of being lightweight is material of interest for turbine engine components. They have good mechanical strength and creep resistance. The major challenge associated with C/SiC composite is their high-temperature oxidation due to high oxygen affinity of carbon and they prone to attack by water vapors that leads to formation of  $\text{Si}(\text{OH})_4$ . The production of this gaseous product can lead to excessive degradation and rapid recession of C/SiC composite. This chemical reaction can harm the arrangement of carbon fibers and also cause degradation of composite [2].

### 2.1.2. Top coat

Environmental and thermal barrier coatings (ETBCs) are a way to reduce the impact of heat on the base material of gas turbine engine[3][4][5]. Typical service temperature of a gas turbine engine is in between 800-1300°C for land-based and Jet engine [6]. Thermal protection system has the capability to reduce the base material temperature up-to 100-300°C with the coating thickness of about 100- 400 $\mu\text{m}$  [3][7] . ETBCs have good mechanical strength and thermal shock resistance as illustrated in **Error! Reference source not found.** The aim of this work is to investigate the thermal resistance of ceramics for the protection of C/SiC composites against high-temperature oxidation together emphasis on surface structure via image analysis.

In the family of ceramics, YSZ/ $\text{Al}_2\text{O}_3$ ,  $\text{ZrO}_2$ ,  $\text{ZrB}_2$ -SiC,  $\text{TiB}_2$ ,  $\text{Al}_2\text{O}_3$ -13% $\text{TiO}_2$ , Si-Zr,  $\text{Al}_2\text{O}_3$  are the reported materials used as a topcoat with the provision of bond coat for the protection of C/SiC composites [6], [8]–[15].

This challenge introduces a new concept in coating technology that is thermal and environmental barrier coatings. Thermal and environmental barrier coatings can reduce the risk of turbine blade /vane failure after implying state of the art material, optimum thickness of coating, and improve manufacture of coating structure. In this decade, researchers and manufacturers are in struggle to find out state of art material for TBCs. This study will emphasis on ceramic oxide as an effective material for C/SiC thermal and chemical protection.

### **2.1.3 Key features of protective coatings system**

1. Selection of coating material and coating technology.
2. Thermo-physical compatibility (thermal expansion) and Chemical compatibility (wetting angle, chemical stability, etc.)
3. The thickness of the protective coating at the surface of the turbine blade.
4. Diffusion barrier function against working environment.

## **2.2. Materials for ETBCs**

Materials for antioxidation coating must have good thermos-mechanical properties, especially of high melting point, phase stability, low evaporation rate, chemical inertness, thermal expansion match with base material, and should resistant to oxidative exposure[17]. TBCs material should have good surface adherence along with low sintering rate of the porous microstructure[18]. Preferably coating materials are zirconia partially stabilized with yttria (PYSZ),  $\alpha$ -alumina,  $\text{ZrC/SiC}$ , and  $\text{ZrB}_2/\text{SiC}$ , mullite,  $\text{La}_2\text{Zr}_2\text{O}_7$ , have been evaluated [19][20][21][11][18]. From early 80s, Due to low thermal conductivity, yttria-stabilized zirconia (YSZ) is the most used material for thermal insulation of turbine components.

Table 2.1: Thermal properties of materials for gas turbines:

Material	Thermal Conductivity W/m. K	Co-efficient of Thermal Expansion $10^{-6}$ ( $^{\circ}\text{C}^{-1}$ ) at 1000 $^{\circ}\text{C}$	Melting Temp ( $^{\circ}\text{C}$ )	Fracture Toughness $\text{Mpa}\cdot\text{m}^{1/2}$	Poisson's ratio	Young's Modulus Gpa
Base material						
C/C-SiC [22]	120	4.2	1600	2.4		75.2
Monel 400[23]	21.8	14	1300-1350			
TBCs Coating Material						
Alumina [24]	20	8.4	1750	4.5	0.27	393
ZrO <sub>2</sub> [25]	2.5-3	11	2700	6.5-8	.32	207
TiO <sub>2</sub> [26]	11.3	8.1	1850	3.2		
YSZ[27]	2.9	11	2700			
ZrB <sub>2</sub> -SiC [28]	37[29]	7.1		3.5	0.15	489
ZrB <sub>2</sub> [29]	60	5.9	3245	3.5	0.14	492

### 2.3. Corundum or Alumina as ETBCs material

Alpha Alumina is the thermally-mechanical phase of aluminum oxide with low coefficient of thermal expansion and zero diffusivity for oxygen. It is strongly water repellent but has high thermal conductivity. High thermal conductivity enhances the flow heat from hotter area to cooler area and then radiant back to atmosphere. Alpha alumina is hard and chemical inert compound as it can be a promising candidate for ETBC application. Optimum availability of porosity and horizontal cracks can overcome the thermal expansion mismatch of alpha alumina and C/SiC-Composite. As heat/thermal wave approaches the interface between alumina coating and composite surface, it will facilitate the growth of Al<sub>2</sub>O<sub>3</sub>-SiC Thermally grown oxides. These TGOs increase the thermal resistance insulation (TRI) at the interface and served as a bond coat for the substrate surface. These will strengthen the bonding between ETBCs coating

and substrate surfaces. This will improve the thermal shock life of C/SiC composite as horizontal cracks and nanopores will release the thermal stress concentration [30]. Thermal stresses originated due to TGOs and CTE mismatch. Slow growing oxide scale and CTE mismatch are governing parameters for thermal resistance at the interface. Thermal stresses resulted can be calculated by

$$\sigma_t = (\alpha_c - \alpha_s) \times \frac{(\Delta T \times E_c)}{1 - \nu_c} \quad 1$$

Where  $\alpha_c$  and  $\alpha_s$  are coefficient of thermal expansion for coating and substrate respectively.  $\Delta T$  is the temperature difference between room temperature and thermal shock temperature.  $E_c$  is the Young's modulus and  $\nu_c$  is poisson's ratio of the coating.

Phase stability is an important material property for High-Temperature application especially for hypersonic aircraft. Thermal stresses and thermal fatigue life are directly related with the phase change behavior at High-Temperature

Deposition techniques are also important to determine the coating behavior with material as well. Literature reported various deposition coating technologies i.e. slurry deposition via dip coating [31] [32], chemical vapor deposition, slurry painting[11], [21], sol-gel process [33].

## 2.4. Microchannel Cooling System

Microchannel heat exchangers are a promising technology to increase the system's operational efficiency of HVAC&R equipment as well as to reduce the carbon footprint of refrigeration and air conditioning unit on the global environment. The system efficiency mainly depends on design consideration for fully developed flow as well as on material aspect of flow section. In microchannel heat exchanger, effective condensation can be accomplished by enhancing effective surface area to volume ratio and, also by optimizing the saturated vapor and liquid ratio inside the channel flow section. The heat transfer in the microchannel is mainly depended on hydraulic diameter ( $D_H$ ), which is  $D_H < 1\text{mm}$  for effective condensation inside microchannel. The motivation of microchannel phase change research has been the necessity for high-heat flux removal especially from engine and electronic devices [4].



### 2.4.1. Understanding of flow patterns

Understanding of flow patterns inside the horizontal microchannel can be developed by analyzing the flow regime maps. Flow regime maps are generated by considering the fluid flows and channel parameters with thermophysical properties of condensation fluid. Researchers discussed the interrelation among mass fluxes, channel size, channel geometry, fluid properties and directing forces i.e. gravitational forces, viscous drag forces, inertial forces, buoyancy forces, and surface tension forces during the flow inside the microchannel.

Suo & Griffith [5] developed the first understanding of flow regime map inside the capillary sized flow channel during adiabatic heat transfer. Their findings stated that usually in small diameter tubes, flow transition will occur in two stages: first, slug flow to bubbly flow, and secondly bubbly- slug flow to annular flow at higher flow rates in zero gravity field. In this study, they considered the surface tension forces, viscous drag forces, and inertial forces as main governing forces of flow regime transition.

Taitel and Dukler [6] presented a theoretical flow regime map based on dimensionless flow parameters. They formulated five flow regime transition groups included as stratified-annular, stratified-intermittent, intermittent-dispersed bubble, stratified smooth-stratified wavy, and annular dispersed liquid-intermittent-dispersed bubble. Their parametric study considered five different dimensionless parameters. They stated that at low flow rates intermittent flow can only occur when the ratio between liquid level and channel size is 0.5. They suggested that intermittent flow can only be established in the horizontal channel if the liquid level inside the channel goes higher than the center of flow sphere. Primarily the wave stability controlled the transition of flow regime. For stabilized waves, the intermittent flow will occur while higher flow rates cause instability that will lead to annular flow regimes. Generalized flow regime map was established between Martinelli parameter  $X$  and  $K$  (dimensionless parameter), where  $K$  can be obtained by multiplying the modified Froude number with the square root of Reynolds number for liquid.

Breber et al. [7] developed the first condensation flow regime map. They correlated the ratio of shear forces to gravitational forces on the condensate film and the liquid volume fraction inside the microchannel for the flow regime map. They deduced that theoretical and experimental

studies have satisfied each other for the establishment of transition boundaries in flow regime map. Their study was related with vertical and horizontal condensation of refrigerants, R-11, R-12, R-113, n-pentane, and steam. They established a simplified flow regime map that satisfied the Taitel & Dukler's theoretical flow regime map for horizontal channel condensation.

Barnea et al. [8] studied the effect of surface tension forces for slug formation in small tube channels for the transition of annular to slug flow. They proposed an experimental modification to the Taitel and Dukler's theoretical-empirical model to account for a balance between surface tension and gravitational forces in the annular to slug transition. They recommended that at low liquid flow rates in small channels ( $D_H > 5\text{mm}$ ), the transition from annular to slug flow can be demonstrated by studying the effect of gravitational and shear/surface tension forces during two-phase flow inside the microchannel. Recent studies regarding two-phase flow in microchannels ( $D_h \ll 1\text{ mm}$ ) were focused on flow regime maps in terms of superficial liquid-vapor velocities for adiabatic air-water mixtures [9].

Serizawa et al. [10] investigated flow patterns during the two-phase flow of air-water mixtures flowing inside circular tubes with  $D_H$  25-100  $\mu\text{m}$ . Their flow visualization was done by using the NIKON SMZ-U type microscope together with a high-speed video camera for flow visualization and observed frequent flow patterns such as; dispersed bubbly, liquid ring, annular, wispy annular, and liquid-droplet.

## **2.5. Problem Statement**

For higher efficiencies, there should be an increase in turbine gas inlet temperature, while conventional material i.e. Ni- based superalloys can't withstand against creep and thermal oxidation exerted by combustion load e.g. elevated temperatures. For increasing the thermal tolerance of Ni superalloy above than their melting point, there is need of external protection system that can reduce the heat penetration to the substrate's surface. However, to meet the requirements for increased turbine temperatures e.g. 1500-1600°C, more advanced materials have been introduced into the turbine section of high performance, power generation units e.g. DS alloys, ceramics composites e.g. C/SiC, due to the complexity, of casting technologies and high cost of Ni-based superalloys. [34]. C/SiC composites being lightweight, combining with high specific strength and damage tolerance represented a candidate material for high-

temperature components of gas turbine engines. Nevertheless, major obstacles in the manufacturing of C/SiC are high reactivity and poor wettability of the carbon fibers along with the sensitivity of carbon fibers to oxidizing environment beyond 400°C[35]. At the same time, at higher operating temperatures (>1200°C) [36], the mechanical behavior of C/C-SiC composites is strongly affected because of the oxidation process of the fiber, inter-phase, and matrix, which led to thermal spallation[37]. To overcome these challenges. C/C-SiC composites must be provided by anti-oxidation protection together with innovative microchannel Cooling to withstand the extreme operating conditions.

## **2.6. Objectives of Study**

- Deposition of Alumina Coating at Monel 400 superalloy and C/C-SiC composites via slurry dip coating route
- Investigating the isothermal oxidation performance of Alumina coated substrates at 1000°C temperatures
- Evaluate the thermal shock resistance of alumina coated C/C-SiC after dynamic thermal shock testing
- Analyzing the microstructure and microchemistry of Alumina Coating via XRD, SEM & EDS analysis
- Performing the image analysis for surface measurements i.e. porosity, surface roughness, and surface profile

## Thesis Flow Chart

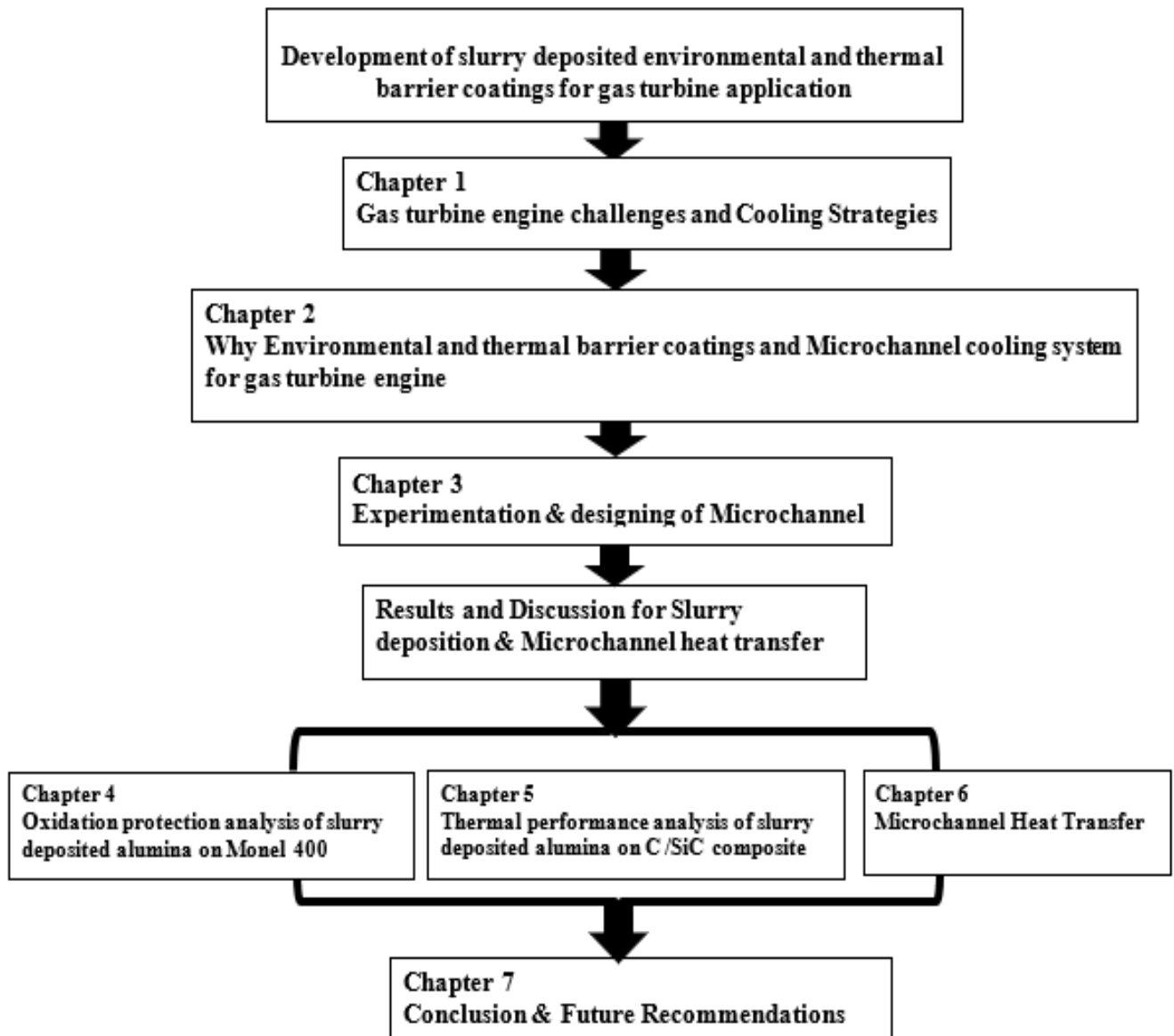


Figure 2.2: Thesis flow for the study

## Summary

As previously mentioned, a lot of work has done and reported for the oxidation protection of C/SiC with the provision of environmental and thermal barrier coatings. Most of the reported literature comprised of costly deposition techniques i.e. Atmospheric plasma spraying, combustion assisted powder flame spraying, etc. Meanwhile, they are focused on developing multilayered coating system. This is the present need of sustainability that “high efficiencies at the little cost of materials/resources”. The research presented here is an effort to add up in the current knowledge of thermal protection systems. Before this, the work was only limited to superalloy, but in this thesis, ETBCs research expands up-to-the materials of future, “composite”. In this study, Isothermal oxidation test and thermal shock cycling was done to evaluate the thermal performance of ceramics as ETBCs.

Understanding of flow patterns inside the horizontal microchannel can be developed by analyzing the flow regime maps. Flow regime maps are generated by considering the fluid flows and channel parameters with thermophysical properties of condensation fluid. Researchers discussed the interrelation among mass fluxes, channel size, channel geometry, fluid properties and directing forces i.e. gravitational forces, viscous drag forces, inertial forces, buoyancy forces, and surface tension forces during the flow inside the microchannel.

## References

- [1] R. Vaßen, M. O. Jarligo, T. Steinke, D. E. Mack, and D. Stöver, “Overview on advanced thermal barrier coatings,” *Surf. Coatings Technol.*, vol. 205, no. 4, pp. 938–942, 2010.
- [2] G. Turbines and K. N. Lee, “Protective Coatings for Gas Turbines 4.4.2-1 Introduction,” pp. 419–437.
- [3] J. D. Osorio, A. Toro, and J. P. Hernandez-Ortiz, “Thermal barrier coatings for gas turbine applications: failure mechanisms and key microstructural features,” *Dyna*, vol. 79, no. 176, pp. 149–158, 2012.
- [4] B. Zou *et al.*, “A new double layer oxidation resistant coating based on Er<sub>2</sub>SiO<sub>5</sub>/LaMgAl<sub>11</sub>O<sub>19</sub> deposited on C/SiC composites by atmospheric plasma spraying,” *Surf. Coatings Technol.*, vol. 219, pp. 101–108, Mar. 2013.
- [5] Z.-Q. Yan, X. Xiang, X. Peng, C. Feng, H.-B. Zhang, and B.-Y. Huang, “Oxidation behavior of oxidation protective coatings for C/C-SiC composites at 1 500 °C,” *Trans. Nonferrous Met. Soc. China*, vol. 19, pp. 61–64, 2009.
- [6] R. Trice, Y. Su, J. Mawdsley, and K. Faber, “Effect of heat treatment on phase stability, microstructure, and thermal conductivity of plasma-sprayed YSZ,” *J. Mater. Sci.*, vol. 37, pp. 2359–2365, 2002.
- [7] P. Prapamonthon, H. Xu, W. Yang, and J. Wang, “Numerical Study of the Effects of Thermal Barrier Coating and Turbulence Intensity on Cooling Performances of a Nozzle Guide Vane,” *Energies*, vol. 10, no. 3, p. 362, 2017.
- [8] X. J. Lu and P. Xiao, “Constrained sintering of YSZ/Al<sub>2</sub>O<sub>3</sub> composite coatings on metal substrates produced from electrophoretic deposition,” *J. Eur. Ceram. Soc.*, vol. 27, no. 7, pp. 2613–2621, 2007.
- [9] J. Zhang, Q. Fu, P. Zhang, J. Qu, R. Yuan, and H. Li, “Surface & Coatings Technology Rapid heat treatment to improve the thermal shock resistance of ZrO<sub>2</sub> coating for SiC coated carbon / carbon composites,” *Surf. Coat. Technol.*, vol. 285, pp. 24–30, 2016.
- [10] C. Courtois, J. Desmaison, H. T, and S. E. E. S. Cedex, “Protection against oxidation of C / SiC composites : oxidation behaviour of CVD TiB<sub>2</sub> coated substrates,” *J. Phys. Iv*, vol. 3, 1993.
- [11] W. Q. Xiang Yang\* , Cao Feng, “ZrB<sub>2</sub>-SiC as a protective coating for C/SiC

- composites: Effect of High-Temperature oxidation on thermal shock property and protection mechanism.” *Journal of Asian Ceramic Societies*, pp. 159–163, 2016.
- [12] L. Cheng, Y. Xu, L. Zhang, and R. Gao, “Oxidation Behaviour of C/SiC Composites with a Si-Zr Coating from Room Temperature to 1500 °C,” in *High-Temperature Ceramic Matrix Composites*, Weinheim, FRG: Wiley-VCH Verlag GmbH & Co. KGaA, 2006, pp. 268–273.
- [13] X. LU, D. YAN, Y. YANG, Y. DONG, J. HE, and J. ZHANG, “Phase evolution of plasma sprayed Al<sub>2</sub>O<sub>3</sub>–13%TiO<sub>2</sub> coatings derived from nanocrystalline powders,” *Trans. Nonferrous Met. Soc. China*, vol. 23, no. 10, pp. 2951–2956, 2013.
- [14] A. K. Krell, A. T. Sobczyk, A. Krupa, and A. Jaworek, “Thermal resistance of Al<sub>2</sub>O<sub>3</sub> coating produced by electrostatic spray deposition method,” *Mech. Mater.*, vol. 98, pp. 120–133, 2016.
- [15] Y. Xiang, W. Li, S. Wang, and Z.-H. Chen, “Preparation of UHTC based coatings for C–SiC composites by slurry and CVD,” *Mater. Technol.*, vol. 27, no. 3, pp. 257–260, Jul. 2012.
- [16] L. A. Tkachenko, A. Y. Shaulov, and A. A. Berlin, “High-temperature protective coatings for carbon fibers,” *Inorg. Mater.*, vol. 48, no. 3, pp. 213–221, Feb. 2012.
- [17] B. Zou *et al.*, “Microstructure, oxidation protection and failure mechanism of Yb<sub>2</sub>SiO<sub>5</sub>/LaMgAl<sub>11</sub>O<sub>19</sub> coating deposited on C/SiC composites by atmospheric plasma spraying,” *Corros. Sci.*, vol. 62, pp. 192–200, 2012.
- [18] X. Q. Cao, R. Vassen, and D. Stoeber, “Ceramic materials for thermal barrier coatings,” *J. Eur. Ceram. Soc.*, vol. 24, no. 1, pp. 1–10, 2004.
- [19] R. Braun *et al.*, “Environmental/thermal barrier coating systems deposited on Nb/Nb<sub>5</sub>Si<sub>3</sub> based alloy,” *Mater. High Temp.*, vol. 32, no. 1–2, pp. 50–56, Jan. 2015.
- [20] M. Carlin, “DESIGN, MANUFACTURE, AND HIGH-TEMPERATURE BEHAVIOUR OF  $\alpha$ -PHASE BONDCOAT FOR THERMAL BARRIER COATING Supervisor:,” 2007.
- [21] I. Krenkel, “Carbon fibre reinforced silicon carbide composites (C/SiC, C/C-SiC),” *Handb. Ceram. Compos.*, pp. 117–148, 2005.
- [22] USA specialmetals Corporation, “Physical Constants and Thermal Properties of Monel Alloy 400.”

- [23] “Material Properties Charts.”
- [24] chemicalland21, “ZIRCONIA (ZIRCONIUM DIOXIDE).” .
- [25] AZOmaterials, “Titanium Dioxide - Titania ( TiO<sub>2</sub>).” .
- [26] H. Zhao, F. Yu, T. D. Bennett, and H. N. G. Wadley, “Morphology and thermal conductivity of yttria-stabilized zirconia coatings,” *Acta Mater.*, vol. 54, pp. 5195–5207, 2006.
- [27] S. C. Zhang, G. E. Hilmas, and W. G. Fahrenholtz, “Mechanical properties of sintered ZrB<sub>2</sub>–SiC ceramics,” *J. Eur. Ceram. Soc.*, vol. 31, no. 5, pp. 893–901, 2011.
- [28] J. F. Justin and A. Jankowiak, “AL03-08 1 High-Temperature Materials Ultra High-Temperature Ceramics: Densification, Properties and Thermal Stability.”
- [29] L. Wang *et al.*, “Effect of interface on the thermal conductivity of thermal barrier coatings: A numerical simulation study,” *Int. J. Heat Mass Transf.*, vol. 79, pp. 954–967, 2014.
- [30] M. Aparicio and A. Durán, “Yttrium Silicate Coatings for Oxidation Protection of Carbon-Silicon Carbide Composites,” *J. Am. Ceram. Soc.*, vol. 83, no. 6, pp. 1351–1355, Dec. 2004.
- [31] S. K. Khaja-abdul, “SLURRY BASED COATINGS ON SILICON BASED CERAMICS,” Cleveland State University, Cleveland OHIO, 2006.
- [32] W. Yee, “Oxidation of Carbon-Carbon Composite,” Southern Illinois University Carbondale, 2016.
- [33] R. Ali, “Phase Change Phenomena During Fluid Flow in Microchannels.”
- [34] P. Griffith, “C \*\*,” 1963.
- [35] Y. Taitel and a E. Dukler, “A Model for Predicting Flow Regime Horizontal and Near - 0 - 0 I ransitions Horizontal Gas-liquid Flow,” *AIChE J.*, vol. 22, no. 1, pp. 47–55, 1976.
- [36] G. Breber, J. W. Palen, and J. Taborek, “Prediction of Horizontal Tubeside Condensation of Pure Components Using Flow Regime Criteria,” *J. Heat Transfer*, vol. 102, no. 3, p. 471, 1980.
- [37] D. Barnea, Y. Luninski, and Y. Taitel, “Flow Pattern in Horizontal and Vertical Two-Phase Flow in Small Diameter Pipes,” *Can. J. Chem. Eng.*, vol. 61, no. 5, pp. 617--620,



1983.

- [38] J. R. Thome, "Mini- and Microchannel Condensation," 2015, pp. 231–284.
- [39] A. Serizawa, Z. Feng, and Z. Kawara, "Two-phase flow in microchannels," *Exp. Therm. Fluid Sci.*, vol. 26, no. 6–7, pp. 703–714, 2002.
- [40] K. Singh, "Advanced Materials for Land Based Gas Turbines," *Trans. Indian Inst. Met.*, vol. 67, no. 5, pp. 601–615, Oct. 2014.
- [41] A. Z. Abidin *et al.*, "EVALUATION OF ALUMINA AS PROTECTIVE COATING FOR CARBON FIBERS IN MAGNESIUM-BASED COMPOSITES," 2015.
- [42] X. Yang, L. Wei, W. Song, Z. Bi-feng, and C. Zhao-hui, "ZrB<sub>2</sub>/SiC as a protective coating for C/SiC composites: Effect of High-Temperature oxidation on mechanical properties and anti-ablation property," *Compos. Part B Eng.*, vol. 45, no. 1, pp. 1391–1396, Feb. 2013.
- [43] X. Yang, C. Zhao-hui, and C. Feng, "High-temperature protective coatings for C/SiC composites," *J. Asian Ceram. Soc.*, vol. 2, no. 4, pp. 305–309, Dec. 2014.

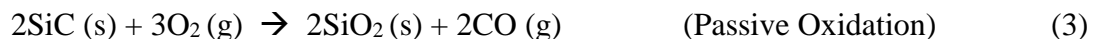
# Chapter 3

## Mechanism of Mass change in C/SiC Composite at high temperature sintering

C/SiC composite based on reinforcement of 2D carbon fibres and SiC matrix for improving the thermomechanical properties of carbon composites. As the carbon fibres are prone to oxidation at temperature above 400°C, SiC matrix is embedded to improve the structural stability against hot atmosphere. SiC matrix not only provide toughness to carbon composites but also ensure the oxidation protection via silica formation  $\geq 600^\circ\text{C}$  at the surface of composite.  $\text{SiO}_2$ , a refractory oxide with self healing capability provided the protection above than  $1050^\circ\text{C}$  [1]. Due to good mobility under gravity or surface tension forces, liquid  $\text{SiO}_2$  fills up the cracks those were developed during oxidation of composites. Oxidation products of C/SiC composite  $\text{CO}$ ,  $\text{CO}_2$ ,  $\text{SiO}_2$  and volatile  $\text{SiO}$  [2]–[4].

### 3.1. Mode of C/SiC Oxidation

C/SiC composites are prone to oxidation in terms of carbon fiber and SiC matrix. As temperature goes above  $400^\circ\text{C}$ , carbon fiber oxidized into  $\text{CO}_2$  and  $\text{CO}$ . These oxides evaporate and left the open spaces for further diffusion of oxidizing species that intensified the oxidation process. At temperature  $800^\circ\text{C}$ , SiC matrix oxidized at higher rate due passive oxidation [2]. At higher temperature, ionic oxygen diffused and react with the silica.  $\text{SiO}_2$  formed a protective layer to inhibit the catastrophic oxidation of composite. Following are the competent reactions those run side by side during oxidation of C/SiC composite.



Thermodynamically it is noted that SiC started to oxidize at 600°C [3]. Surplus diffusion of oxygen resulted in volatile SiO formation that resulted in weight loss C/SiC composite. SiO increased the number of reaction sites and twofold the catastrophic oxidation of C/SiC composite. At atmospheric pressure, passive oxidation dominates and resulted in the formation of SiO<sub>2</sub> layer that get deposited over the surface of composite leading to weight gain. The SiO<sub>2</sub> formed due to passive oxidation is amorphous in nature and needs high temperate exposure to crystallize it. SiO<sub>2</sub> after solidification seals up the cracks and pores, to restrict the diffusion of oxygen. Although the oxidation kinetics of SiO<sub>2</sub> at 600°C is low but the process speeds up as the temperature goes above 600°C[5].

After solidification and penetration of SiO<sub>2</sub>, following processes will continue,

- 1- Diffusion and removal of oxygen from the pores
- 2- Lowering of hot gas temperature due to effective removal of heat via voids or pores

Experiments showed that, at higher temperature ionic oxygen transportation dominated and followed parabolic oxidation rate.

SiO<sub>2</sub> deposited around the carbon fibers and SiC matrix, for the protection from catastrophic oxidation of C/SiC composite.

### **3.2. Antioxidation behavior with Thermal barrier Coatings**

The present study based on the Al<sub>2</sub>O<sub>3</sub> coating on C/SiC composite to protect it from catastrophic oxidation. Al<sub>2</sub>O<sub>3</sub> based coatings provide corrosion and oxidation resistance, as these coatings allow the diffusion of considerable heat and oxygen ion to the substrate surface that is sufficient for the formation of amorphous SiO<sub>2</sub>. High temperature sintering resulted in solidification of amorphous SiO<sub>2</sub>, that seals the crack and restrict the further penetration of heat beyond the SiO<sub>2</sub> layer. The activation energy of oxygen ion for amorphous SiO<sub>2</sub> reported as 298 kJ. mol<sup>-1</sup> at 800-1000°C [6].

The mass change during oxidation of C/SiC depends on the oxidation temperature. The critical temperature for C/SiC oxidation was reported 680°C with a activation energy of 28 Kcal/mol. At this time, the pores and cracks in developed coating are opened and allowed sufficient oxygen diffusion that started to degrade carbon fiber first. Due to oxidation, fibre bundle becomes loose and provided extensive nucleation point for oxygen molecule [1]. Oxidation rate

is directly related with the exposure time. The resistance to oxidation decreased with increasing the oxidation time. SiC matrix got oxidized into silica that suppressed the diffusion of oxygen after sealing up the cracks. It can be noted that oxygen was diffused by microcracks those originated during coating process. To decrease the crack density and rearrange the pores, initial heat treatment was done at 250°C under vacuum. SiO<sub>2</sub> due to good mobility sealed the cracks and solidified as the coating was cooled down after sintering. During cooling, coating shrank and prone to crack but the presence of silica overcome this risk.

### **3.3. Effect of sintering at 1073K**

The oxidation protection of Al<sub>2</sub>O<sub>3</sub> coated C/SiC depends on the sintering temperature. In this study, 1073K was decided as sintering temperature to promote the interfacial bonding and less porous interface. At 1073 K sintering, Formation of stable silica layer over the surface is favorable for oxidation protection if it gets solidify. The selection of sintering temperature depends on the volatility of silica.

If temperature becomes higher than 1373K then SiO<sub>2</sub> will become volatile [15]. If temperature got lower as 873 K, then active oxidation dominated, and the resulted oxidation products comprised of volatile oxides, i.e. SiO and CO formation [2]. In this study, coating after vacuum drying, sintered at 1073 K that favors passive oxidation for the formation of stabilized amorphous SiO<sub>2</sub> layer, solidified during cooling process after sintering. At 1073 K, SiO<sub>2</sub> formed and deposited over the carbon fibre and SiC matrix, provided the protection against catastrophic high temperature oxidation up-to 1996 K. The formation of SiO<sub>2</sub> reduces the risk of coating failure due to CTE mismatch between composite and alumina coating. Alumina has higher CTE than C/SiC that can cause delamination of coating. A CTE transition layer established depending on the bonding of SiO<sub>2</sub>

with C/SiC. The values of  $\alpha$  for SiO<sub>2</sub>-C-SiC and SiO<sub>2</sub>/SiC are  $5.4 \times 10^{-6}$  and  $8.5 \times 10^{-6}$  respectively [2].

At the start of oxidation, the mass change was in terms of weight loss due to active oxidation of SiC into SiO, with the passage of time passive oxidation started the formation of SiO<sub>2</sub> that suppressed further oxidation of SiC. The exposure time to oxidizing atmosphere also effects the coating densification and bonding strength. Binglin Zou et al, [12] reported Gibbs free energy -180 Kcal/mol. At 1000K for SiO<sub>2</sub> and Kinetic energy for the reaction of carbon with oxygen calculated as 28 Kcal/mol [1]. It is indicated that the reactions are thermodynamically feasible because of  $G_T < 0$  for whole reaction.

Table 3.1: Reported sintering temperature for Environmental and thermal barrier coatings

Substrate Material	Material	Deposition technique	System	Sintering temp. (°C)	Medium	Thermal shock Temp. (°C)
C/SiC [7]	SiC+TiB <sub>2</sub>	CVD	Single		vacuum	1100
SiC [8]	Al <sub>2</sub> O <sub>3</sub> -Mullite	Slurry-dip	Single & Duplex	1200	air	1200
C/SiC [9]	SiC/Si-Mo	CVD + Slurry Painting	Multilayer	1500	air	1400
SiC & Si <sub>3</sub> N <sub>4</sub> [10]	Mullite/Gd <sub>2</sub> SiO <sub>5</sub>	Slurry	Multilayer	1300C	air	
C/C [11]	SiC	Pack cementation	Single layer	1500	Argon	1500
C/C [12]	ZrB <sub>2</sub> -SiC-Si/Yb <sub>2</sub> SiO <sub>5</sub> /LaMgAl <sub>11</sub> O <sub>19</sub>	Plasma Spraying	Multilayer	2000	air	2000
C/C [13]	ZrO <sub>2</sub> -SiC	Atmospheric plasma Spraying	Multilayer	2000	air	2700
C/SiC[1]	Si-Zr-SiC	Liquid reaction & CVD	Multilayer	1500	Air & Argon	1300

X10CrAlSi18 Steel [14]	$\text{Al}_2\text{O}_3 - \text{TiO}_2$	Electrophoretic spray deposition	Multilayer	1000	air	1000
C/SiC [15]	$\text{Y}_2\text{SiO}_5\text{-SiC}$	Dip coating	Multilayer	1600	Vacuum	1600-400
Sapphire [16]	$\text{ZrO}_2$	EPD	Single layer	1100	air	

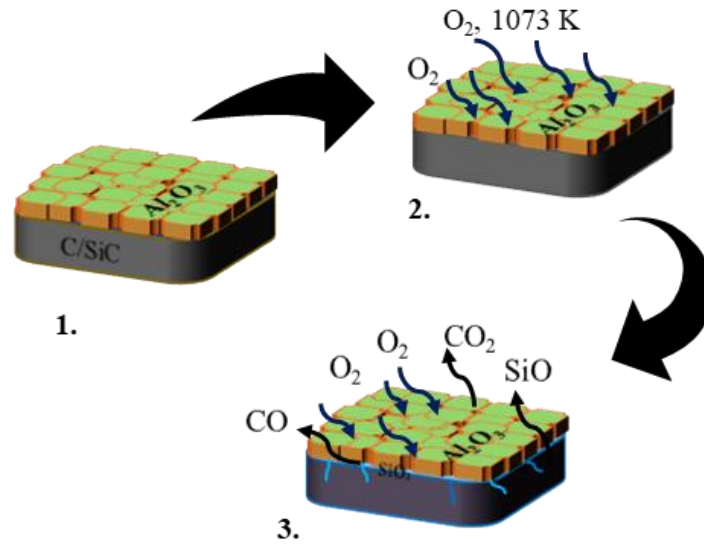


Figure 3.1: Schematic illustration of oxidation mechanism during high temperature sintering of alumina coated C/SiC composite.

The CTE of hexagonal  $\text{Al}_2\text{O}_3$  and C/SiC are about  $9.3 \times 10^{-6}$  [7] and  $3.5 \times 10^{-6}$  [33] respectively over a temperature range of 298 to 1273 K. The difference in CTE has serious impact on the coating adherence that leads to extensive thermal stresses at the interface during thermal cycling. Thus  $\text{Al}_2\text{O}_3$  coating faced shrinkage during drying process more than the C/SiC specimen [7]. Shrinkage caused tensile stresses and initiated the crack production. As deposited coating has loose aggregates of particles at the surface and retains high porosity that requires sintering at high temperature to increase the bond-strength of coating. To behave like a ceramic body, coating needs augmentation in microstructure. During sintering, oxidation of SiC resulted in the production of  $\text{SiO}_2$  (Fig. 3.1). However, after sintering, coating has the best match of CTE because of  $\text{SiO}_2$  formation at the interface. The presence of  $\text{SiO}_2$  on the surface has been confirmed by XRD (Fig. 2).  $\text{SiO}_2$  acts as an industrious transition for CTE mismatch that is

prerequisite for thermal resistant coatings. Formation of SiO and SiO<sub>2</sub> depends on the oxygen pressure, at higher pressure, a mass gain is observed with the formation of SiO<sub>2</sub> according to either equation 4 or 5 [34]

## **Summary**

This chapter discussed the formation of SiO<sub>2</sub> layer at the interface. SiO<sub>2</sub> layer provided oxidation protection to C/SiC composite. The diffusion of oxygen ion at high temperature led to the formation of amorphous SiO<sub>2</sub> that seals the pores and cracks. This study confirmed the formation of amorphous SiO<sub>2</sub> at 600°C.



## References

- [1] L. Cheng, Y. Xu, L. Zhang, and R. Gao, "Oxidation Behaviour of C/SiC Composites with a Si-Zr Coating from Room Temperature to 1500 °C," in *High Temperature Ceramic Matrix Composites*, FRG: Wiley-VCH Verlag GmbH & Co. KGaA, 2006, pp. 268–273.
- [2] J. Roy, S. Chandra, S. Das, and S. Maitra, "OXIDATION BEHAVIOUR OF SILICON CARBIDE - A REVIEW," *Rev. Adv. Mater. Sci.*, vol. 38, pp. 29–39, 2014.
- [3] C. Zhang *et al.*, "Thermal shock resistance of a 2D-C/SiC composite and its damage mechanisms," *Adv. Appl. Ceram.*, vol. 112, no. 8, pp. 499–504, Nov. 2013.
- [4] L. Cheng, Y. Xu, L. Zhang, and X. Yin, "Effect of carbon interlayer on oxidation behavior of C / SiC composites with a coating from room temperature to 1500 ° C," *High Temp.*, vol. 300, pp. 219–225, 2001.
- [5] I. Krenkel, "Carbon fibre reinforced silicon carbide composites (C/SiC, C/C-SiC)," *Handb. Ceram. Compos.*, pp. 117–148, 2005.
- [6] H. P. Oxidation, C. Vapor, and D. Silicon, "of Carbide," vol. 90, pp. 1386–1390, 1989.
- [7] C. Courtois, J. Desmaison, H. T, and S. E. E. S. Cedex, "Protection against oxidation of C / SiC composites : oxidation behaviour of CVD TiB2 coated substrates," *J. Phys. Iv*, vol. 3, 1993.
- [8] J. I. Federer, "Alumina base coatings for protection of SiC ceramics," *J. Mater. Eng.*, vol. 12, no. 2, pp. 141–149, Jun. 1990.
- [9] Z. Yan, F. Chen, X. Xiong, P. Xiao, and B. Huang, "Thermal Shock Resistance of SiC/Si—Mo Multilayer Oxidation Protective Coating for Carbon/Carbon Silicon Carbide Composites."
- [10] S. Ramasamy, S. N. Tewari, K. N. Lee, R. T. Bhatt, and D. S. Fox, "Slurry based multilayer environmental barrier coatings for silicon carbide and silicon nitride ceramics - I. Processing," *Surf. Coatings Technol.*, vol. 205, no. 2, pp. 258–265, 2010.
- [11] C. Huo *et al.*, "Improving the oxidation resistance under thermal shock condition of SiC-coated C/C composites with refined SiC grain size using ferrocene," *Surf. Coatings Technol.*, vol. 316, pp. 39–47, Apr. 2017.
- [12] B. Zou *et al.*, "Oxidation protection of carbon/carbon composites with a plasma-sprayed

ZrB<sub>2</sub>-SiC-

Si/Yb<sub>2</sub>SiO<sub>5</sub>/LaMgAl<sub>11</sub>O<sub>19</sub> coating during thermal cycling,” *J. Eur. Ceram. Soc.*, vol. 35, no. 7, pp. 2017–2025, 2015.

- [13] J. Zhang, Q. Fu, P. Zhang, J. Qu, R. Yuan, and H. Li, “Surface & Coatings Technology Rapid heat treatment to improve the thermal shock resistance of ZrO<sub>2</sub> coating for SiC coated carbon / carbon composites,” *Surf. Coat. Technol.*, vol. 285, pp. 24–30, 2016.
- [14] A. K. Krella, A. T. Sobczyk, A. Krupa, and A. Jaworek, “Thermal resistance of Al<sub>2</sub>O<sub>3</sub> coating produced by electrostatic spray deposition method,” *Mech. Mater.*, vol. 98, pp. 120–133, 2016.
- [15] M. Aparicio and A. Durán, “Yttrium silicate coatings for oxidation protection of carbon-silicon carbide composites,” *J. Am. Ceram. Soc.*, vol. 83, no. 6, pp. 1351–1355, Dec. 2000.
- [16] B. Baufeld, O. van der Biest, and H.-J. Raetzer-Scheibe, “Thermal and Mechanical Properties of Zirconia Coatings Produced By Electrophoretic Deposition,” *Adv. Ceram. Coatings Interfaces II*, vol. 28, no. 3, pp. 3–10, 2008.

# Chapter 4

## Development of slurry deposited ETBCs & Designing of Microchannel

In this chapter, slurry preparation and its deposition via dip coating route will be discussed for environmental and thermal barrier application.

### 4.1. Substrate preparation

The first and foremost step of this study was substrate preparation. The as provided coupon was of  $50 \times 25 \times 5$  mm in dimensions. for keeping experimentation convenient we sliced the substrates in appropriate size to keep the coating process as easy as possible.

#### 4.1.1. C/SiC Composite Slicing

The coupon of C/SiC was sliced into  $15 \times 8 \times 5$  mm with the help of diamond saw Model SYJ-150, MTI Corporation.

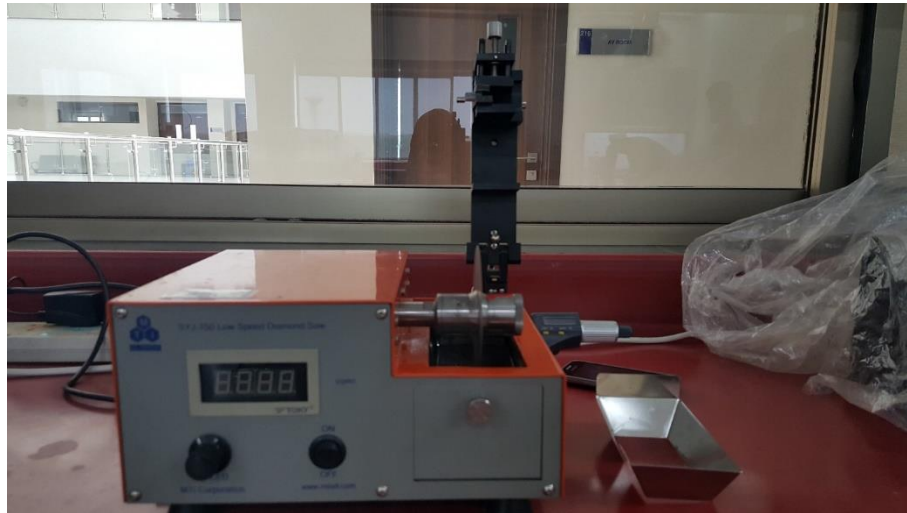


Figure 4.1: Low-speed diamond saw in Advanced Energy Materials and Systems lab

For cutting, coupon was wrapped in unstick paper then fixed in the dicing jaws. After that diamond blade was inserted into the shaft and adjusted. Fresh water was used as lubricant to remove the heat produced due to surface friction and to protect the blade for damage. After confirming everything adjusted, diamond saw was switched on and operation was started at an

adjustable speed of 135 rpm. The coupon was cut into desired dimensions and then send these for surface preparation.

### **Precautions**

Check the level of water in the boat, edge of blade should be dipped in water.

Coupon was placed slowly on blade after starting the machine

Machine should be stopped after removing coupon which was placed on the blade

### **4.1.2. Monel 400 Superalloy Sectioning**

Monel 400 Superalloy coupon was provided as in rod shape with dimensions of  $13 \times 10$  mm.

## **4.2. Surface preparation**

The most important step for slurry deposition is surface preparation. If the surface of coupon is prepared well then coating deposition efficiency will be high.

### **4.2.1. Monel 400 Superalloy Surface preparation**

Monel 400 superalloy coupon was sand blasted at 2Mpa air pressure with alumina sand. Then surface was cleaned by acetone and dried. Further cleaning was performed by using acetone bath and sonicated the coupons with acetone at 50°C for 30 min. in a sonicator.

### **4.2.2. C/SiC composite Surface preparation**

C/SiC composite investigated in this study were prepared by reaction melt infiltration method. Two-dimensional carbon fiber reinforced silicon carbide composite was used as a coating coupon in the study. Small rectangular C/SiC coupons with the dimension of 1.5 x 1x 2 mm were cut by using a low-speed diamond saw (Model SYJ-150, MTI Corporation) at the adjustable speed of 135 rpm. Distilled water was used as a lubricant during cutting of C/SiC coupon. Small coupons were grinded manually using 220 sand paper, followed by acetone bath, sonication, drying, rinsing with acetone and drying again to clean the coupon surfaces.

All the coupons were weighed using an electric balance with a sensitivity of 0.005g to measure the weight loss during isothermal oxidation test and thermal shock testing. The roughness of coupon surfaces was measured by using surface roughness tester (Model No. NDT 110). The roughness parameter Ra (arithmetic mean of the absolute values of the profile deviations) was found to be 0.24 $\mu$ m.

Table 4.1: Manual grinding of C/SiC composite for slurry deposition

<b>Base Material</b>	<b>Grinding</b>	<b>Lubricant</b>	<b>Round</b>	<b>Duration</b>
C/SiC Composite	220 Sand Paper	Fresh Water	3-5	15-30 mints for each round

### 4.3. Slurry Preparation

Alumina slurry constituents were alumina powder with purity of > 99 % purchased by China leadmat advanced materials, distilled water which was prepared in the lab and Polyethyleneimine (PEI) as a binder as well as dispersant. Alumina powder was grinded in mortar and pestle for refining the particle size and forming a graded particle size distribution. The grinding was done for 3-4 hrs. with multiple rounds of each 15 mints continuously. 0.14 wt. % of Polyethylene Imine was added as a binder to enhance the dissolution of alumina in distilled water. The PEI binder enhanced the rheological properties of slurry and facilitated the adhesion of alumina at the coupon surface. For slurry formation, the Al<sub>2</sub>O<sub>3</sub> powder was magnetically stirred for 16 hrs. in hot solution of PEI with distill water at 170 rpm of hot plate. The pH of the slurry was measured by using pH paper that was 7.

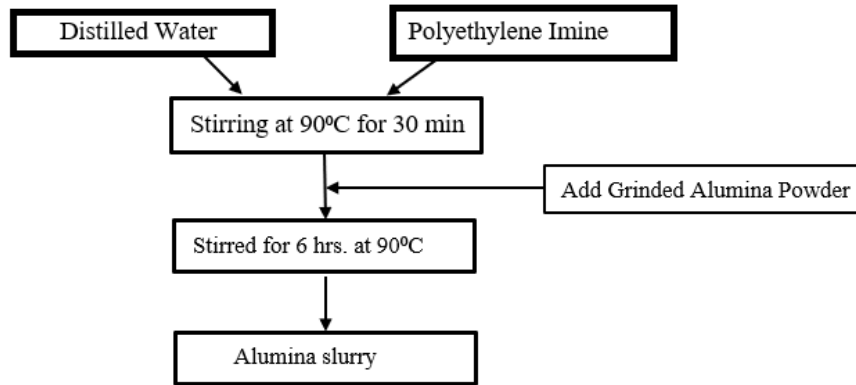


Figure 4.2: Schematic for Alumina slurry preparation

#### 4.3.1. Rheology Properties of Slurry

The slurry for coating should have properties as follow:

- 1- Slurry should be well mixed
- 2- High solid loading increases the adhesion at the surface and decreases the flocculation
- 3- PH of the slurry for ETBCs application in range of 6-11 [1]

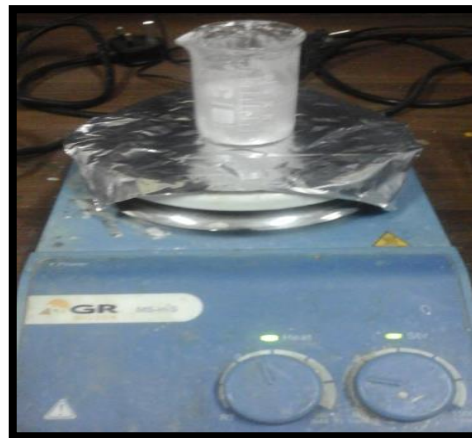


Figure 4.3: Camera image of alumina slurry: Magnetically stirred at 60 rpm for 6 hrs.

#### 4.4. Deposition of Alumina slurry

Alumina slurry was deposited on surface prepared coupons after sonication for extra cleaning. Dip coating process was employed to deposit the slurry on coupon's surface. Dip coater was programmable for adjusting the coat speed and residence time. In this study, slurry was

deposited at 30mm/min travel speed with a residence time of 30 sec in slurry between successive coats. 3 successive coats with a rest time of 5 min resulted in six side coated substrates. After this, the coated coupons were allowed for overnight drying at room temperature. After that weight of each coupon was measured with the help of digital microbalance with a sensitivity of 0.005g.

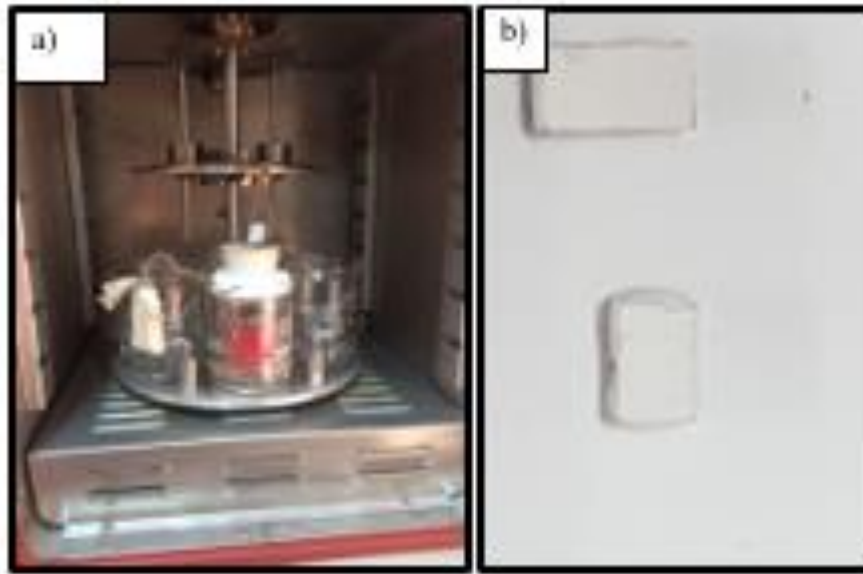


Figure 4.4: a) Alumina slurry deposition via dip coating by using dip coater at C/SiC composite coupon, b) camera images of dip-coated substrate after overnight drying at room temperature

#### **4.5. Heat Treatment/Curing/Sintering of coating**

After drying at room temperature, coated coupon was vacuum dried at 250°C at a vacuum pressure of 0.07Mpa for 2 hr. Heat treatment has its importance for the development of interface between coupon surface and coating. Literature reported heat treatment in two ways:

- 1- Prior deposition process
- 2- After deposition process

Adhesiveness and homogeneity of coating depends on this step. There are various heat treatment temperature reported such as 800°C [2], 1000°C, 1250°C [3].

The basic aims of heat treatment are to improve the surface structure, increase the densification of coating and built up the interface. We have decided sintering temperature of about 800°C to allow the growth of SiO<sub>2</sub> at the interface. During sintering, oxygen penetrated inside the coating and started to react with carbon fibers and SiC matrix and resulted in the production of SiO<sub>2</sub> which act as thermally grown oxides and further densified the interface as compared to surface.

The coated coupons were placed in box furnace and heated at the ramp rate of 10°C/min and cooled at room temperature under natural cooling.

#### **4.6. Sample Preparation for SEM Analysis**

For SEM analysis, gold-palladium coating was prepared to improve the image visualization. For cross-sectional analysis, coupons were embedded in epoxy resin then polished with standard polishing procedure.

#### **4.7. Isothermal Oxidation Testing**

Thermal performance of C/SiC composite coupon and sintered slurry deposited C/SiC coupon were evaluated by isothermal oxidation at 1000°C in the box furnace in an air atmosphere for 3 hrs. with a heating rate of 10°C/min in the box furnace under air atmosphere. After ISOT, coupons were furnace cooled by natural convection at room temperature inside the furnace. Uncoated and coated coupons were weighed after oxidation tests by an analytical balance with a sensitivity of 0.005g. Mass balance equation was used to determine the weight loss percentage given by

$$w = \left( \frac{m_1 - m_2}{m_1} \right) \times 100 \quad (5)$$

Where  $m_1$  and  $m_2$  are the weight in grams before and after oxidation test.

#### **4.8. Thermal Shock Testing**

Dynamic thermal shock (DTS) testing of coated C/SiC coupon was carried out to investigate the thermal performance of slurry deposited Al<sub>2</sub>O<sub>3</sub> in a tube furnace. The furnace was equipped with an Al<sub>2</sub>O<sub>3</sub> tube which is heated up by the heating filament and embedded in the insulating matrix. The sintered coupon was thermal shocked at 1000°C after inserting and extracting it in



the ambient atmosphere. The temperature of the coupon surface was measured by using an infrared thermometer. DTS testing was performed by keeping the coated coupon at 1000°C for 5 min. and immediately extract it at room temperature, where it was cooled down with manual cooling at 30-40°C temperature within 4 min duration. A total of 25 thermal cycles were done to investigate the thermal shock behavior of coated coupons. In the 26<sup>th</sup> thermal cycle, the coated coupon was rest there for 30 min. Overall thermal shock testing was continued for 250 min. duration excluding furnace heating & cooling. Weight was measured after every 5 cycles to estimate the weight change during DTS testing. 26<sup>th</sup> cycle weight was measured after cooling down the coupon at room temperature with natural cooling inside the furnace. Macrograph and SEM images were acquired for the surface and cross-sectional study of slurry deposited Al<sub>2</sub>O<sub>3</sub> coating. Thermal stresses induced at the interface during thermal shock testing were calculated to understand the stresses at the interface (**Error! Reference source not found.**). For cross-sectional analysis, the tested coupon was embedded in epoxy to acquire the cross-sectional view. Before cross-sectional analysis, the epoxy was manual grinded on sandpaper of grain sizes 220, 400, 600, 800, 1000 and then grinded at 1200 grain size sandpaper on Metkon Forcipol 2V grinding and polishing machine. After grinding, grinded coupon was surface polished at 6 and 3µm diamond paper with diamond suspension as a lubricant followed by a standard polishing process. The grain size of the diamond paper was selected based on coating thickness that was calculated about 259 µm on an average of three six side coated coupons after image analysis with Image J and confirmed by cross-sectional analysis after completion of DTS testing.

#### **4.9. Phase stability, microstructure and image analysis**

Phase structure was studied by D8 Advance Bruker X-ray diffractometer (XRD) with Cu K $\alpha$  radiation generated at 40 KV and 30 mA. The scanning rate was 9 step/sec with a step size of 0.02° over a range of 20° to 70°. Surface and cross-sectional study were conducted with the help of Vega3 TEScan scanning electron microscope (SEM).

##### **4.9.1. Image J analysis for porosity, surface roughness, and coating thickness**

Image analysis was performed for measuring the porosity, surface roughness Ra and coating thickness from the individual SEM images. Image J (version 1.51s, for Windows 10, 64-bit,

free software, National Institutes of Health, Bethesda, MD, USA) following the below-given methodology, being thresholded and binarized returning to give porosity for each image. SurfChar J plugin[4], [5] was used to calculate the average surface roughness height and roughness shape factors. Coating thickness was also measured from roughness calculations and reported in **Error! Reference source not found..** The methodology was adopted from these references [6]–[8].

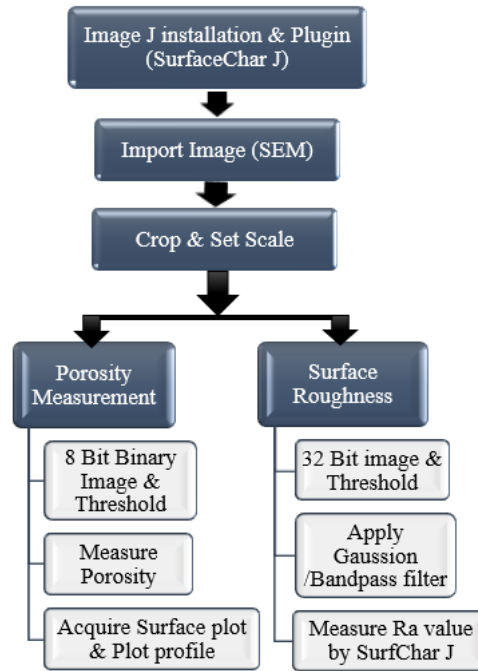


Figure 4.5: Flow diagram showing methodology for image analysis

$R_a$  is the roughness parameter relevant to height that describes the arithmetic average of the absolute values of the profile height deviations recorded along the specified length and measured from the mean line [7].  $R_{sk}$  &  $R_{ku}$  are the shape factor of roughness profile related with skewness and kurtosis, explained the sharpness and broadness of peaks and valleys on the surface. For image analysis, 50  $\mu\text{m}$  sized SEM images were considered to acquire the best estimation of parameters.

## 4.10. Experimental Approach

An experimental facility was developed to produce and measure low mass flux, two-phase flows of low surface tension fluids at varying thermodynamic quality with a maximum pressure of 2070 kPa (300 psia). Figure shows a schematic of the complete facility with important refrigerant thermodynamic state points labeled.

### 4.10.1. Test Section Design

The test section (shown in Figure 2) condensed superheated vapor to a specified thermodynamic quality and then allowed optical access to the two-phase flow. The fluid enters the test section as a superheated vapor and is distributed to the multiple parallel channels. Unlike many other multi-phase visualization studies [9]–[11], where flow enters the test section as a two-phase mixture, superheating the inlet fluid enables a more uniform distribution. The refrigerant is then condensed to the desired quality in the pre-condensing length of the flow channels by water flowing in counter flow from the bottom side (see Figure 2a).

The microchannel heat exchanger plate consisted of five, rectangular (average aspect ratio = 0.92) parallel microchannels in Aluminum 6061. The heat exchange plate was machined on a Fadal VMC15 vertical milling center and the as-machined dimensions of the channels were verified using a ZeScope<sup>TM</sup> optical profiler. The ZeScope<sup>TM</sup> measures surfaces using vertical scanning interference microscopy,

which enables it to resolve three-dimensional features as small as 2  $\mu\text{m}$ . The width and depth of each channel was measured using this technique, with results shown in Table 1. The average measured channel hydraulic diameter was 842.49  $\mu\text{m}$ , with a standard deviation of 1.1%. A hydraulic diameter of under 1.0 mm was desired to maintain a Confinement number below the microscale transition predicted by the literature [12].

An impact resistant polycarbonate was selected for the viewing plate material. With a reported thermal conductivity of 0.19  $\text{W m}^{-1} \text{K}^{-1}$ , the 9.5 mm thick polycarbonate sheet had orders of magnitude higher thermal resistance than the 1.0 mm thick aluminum heat exchange plate, mitigating the risk of substantial heat loss from the test section. For similar reasons, Delrin®

(Polyoxymethylene) was selected for the base plate material, which houses the cooling fluid channel and supports the heat exchange plate. A neoprene O-ring cord was used to seal the heat exchange plate against the base plate to contain the cooling fluid. Lastly, to incorporate NPT ports for the inlet and outlet of the working fluid, 12.7 mm (0.5 inch) thick plates were added at both ends of the test section to integrate the flow inlet and exit NPT fittings. A 0.5-inch diameter O-ring was used to seal the face of the NPT blocks to the viewing section. The blocks were machined from aluminum for ease of tapping the NPT ports and maintaining a face seal near the O-ring. The system was insulated with 5 mm thick aerogel material with a thermal conductivity of  $0.274 \text{ W m}^{-1} \text{ K}^{-1}$  to minimize heat loss wherever optical access to the flow was not required.

#### **4.10.2. Refrigerant and Water Loops**

At state point one (Figure 1), the temperature and pressure of the refrigerant are known and can be used to determine the fluid density entering the flowmeter. To achieve mass fluxes in the range of  $75$  to  $150 \text{ kg m}^{-2} \text{ s}^{-1}$  through the five channels of the test section, the required flow rate of liquid R-134a at the pump and flowmeter ranged from approximately  $13$  to  $25 \text{ mL}\cdot\text{min}^{-1}$ . A positive displacement gear pump was used to provide this flow rate. The pump head is designed such that no lubricating grease or oil contacts any internal flow components, which are driven via a magnetic drive. Because of the replaceable gearing in the system, wide ranges of low mass flow rates are achievable, even with a low viscosity refrigerant. The pump is driven via a magnetic coupling by a brushless 20 to 30 V variable speed motor that is controlled by a 0 to 5 V signal. Both the supply and signal voltages are provided by a variable voltage supply unit capable of 0.01 V variations. From the pump, the fluid enters the vaporizer, which consists of a 250 W in-line cartridge heater controlled by a Variac variable voltage controller. A K-type thermocouple was included in the heater tip to ensure the surface temperature was maintained below  $250^\circ\text{C}$  (maximum operating temperature was  $760^\circ\text{C}$ ). From the vaporizer, superheated refrigerant entered the test section where it was partially condensed and visualized, described in the following sections. After exiting test section at state 3 (in Figure 1), the two-phase mixture was then fully condensed in a counter flow tube-in-tube post-condenser before returning to the gear pump.

A nitrogen charged piston accumulator was used to maintain the desired saturation pressure. Heat was rejected from the test section to a closed loop of circulating deionized water. Because the thermocouples used to measure the water temperature have an uncertainty of  $\pm 0.5^\circ\text{C}$ , a large temperature difference is required on the water-side to keep uncertainty low in the energy balance used to calculate the condensation heat duty. To maintain high water-side temperature difference a combination of low water flow rate and low inlet temperature were required. To provide the desired flow rates, a set of NE-1010 New Era Pump Systems syringe pumps were used (flow rate  $\pm 1\%$  of setpoint). The two syringe pumps are able to communicate with each other and can operate in continuous flow mode with one pump filling as the other discharges. The two 60 mL syringes were connected to a water reservoir by a set of one-way valves, and then fed into the water-side pre-chiller. The circulating deionized water and the post-condenser were cooled by a NESLAB M75 circulating chiller.

#### **4.11. Condensation system**

Water and refrigerant temperatures were measured with T-type thermocouples inserted into the flow. The thermocouples were calibrated in a heated drywell and ice bath against a high accuracy Fluke platinum resistance thermistor. Refrigerant pressure was measured at the pump and test section inlet (state points one and 2) using Omega PX209-300A1 absolute pressure transducers. The transducers used have a measurable range of 0-2070 kPa (0-300 psia) and a reported uncertainty of  $\pm 2.59$  kPa. Because R-134a is a low viscosity, low surface-tension fluid it is challenging to pump and meter at low flow rates. To measure flow rates in the 13-25 mL  $\text{min}^{-1}$  range, a nutating flowmeter from DEA Engineering was used.

The flowmeter has a dual chamber flow path that allows liquid to pass through only by displacing the nutating metering element. The nutating flowmeter is capable of measuring low-viscosity flows from 1-250 mL  $\text{min}^{-1}$  and has a rated max operating pressure of 20.7 Mpa (3,000 psia) with a nominal uncertainty of  $\pm 1.0\%$  of reading. The water-side volumetric flow rate was directly measured from the New ERA syringe pump controller, with a reported uncertainty of  $\pm 1.0\%$  of reading.

A Phantom V310 high-speed camera was used to capture optical images of the flow. A 60mm Nikon AF Micro Nikon™ lens was used to capture a 1280 x 800pixel resolution image of the viewing section. Because frames were captured at 2400 fps with a 415.96  $\mu$ s exposure time, a large amount of system light was required. Two 120 W Energy Saver LED™ lights were used to illuminate the test section channels. The LED lights are capable of producing 13,000 lumens with minimal heat generation.

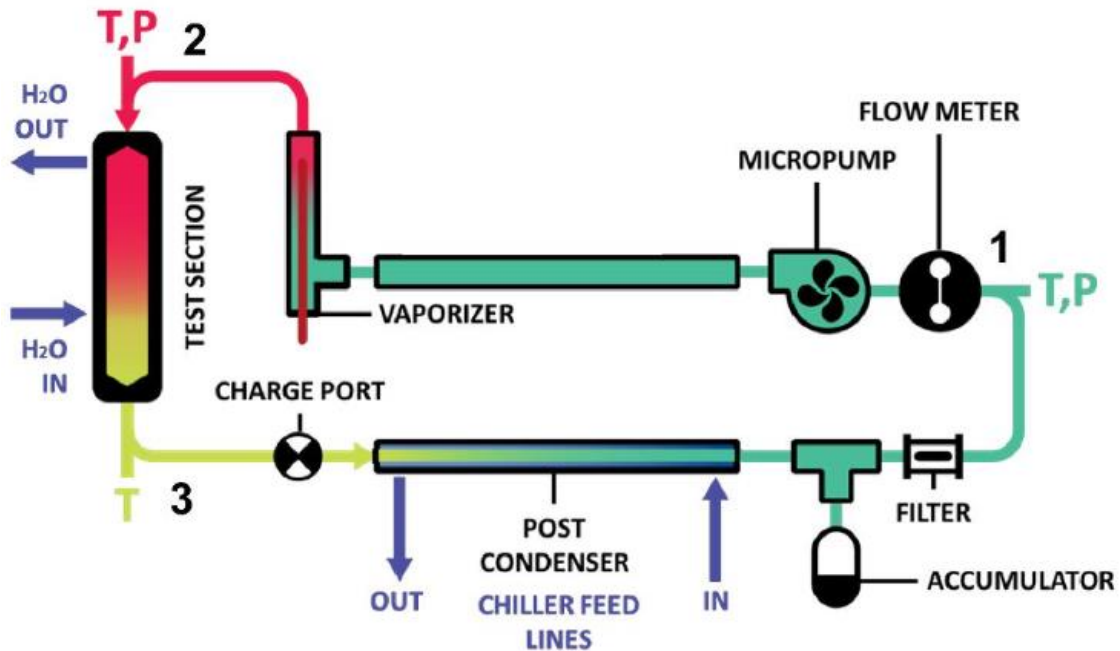


Figure 4.6: Schematic of test facility

## 4.12. Experimental Methods and Analysis

To capture each data point, the refrigerant and cooling water flow rates were adjusted until the desired state point was reached. After temperature fluctuations were within  $\pm 0.5^\circ\text{C}$  for a minimum of five minutes, the system was determined to be at steady state and data capture was started.

Temperature, pressure, and fluid flow rate measurements were collected using a LabVIEW[13] program developed to receive information from the DAQ system. Data was collected at a rate

of 1 Hz for a minimum of 4 minutes. The Phantom PCC software provided with the Phantom camera was used to collect the visualization footage. Images and video of each data point were exported from the .cine raw files into more manageable video and image files for comparison.

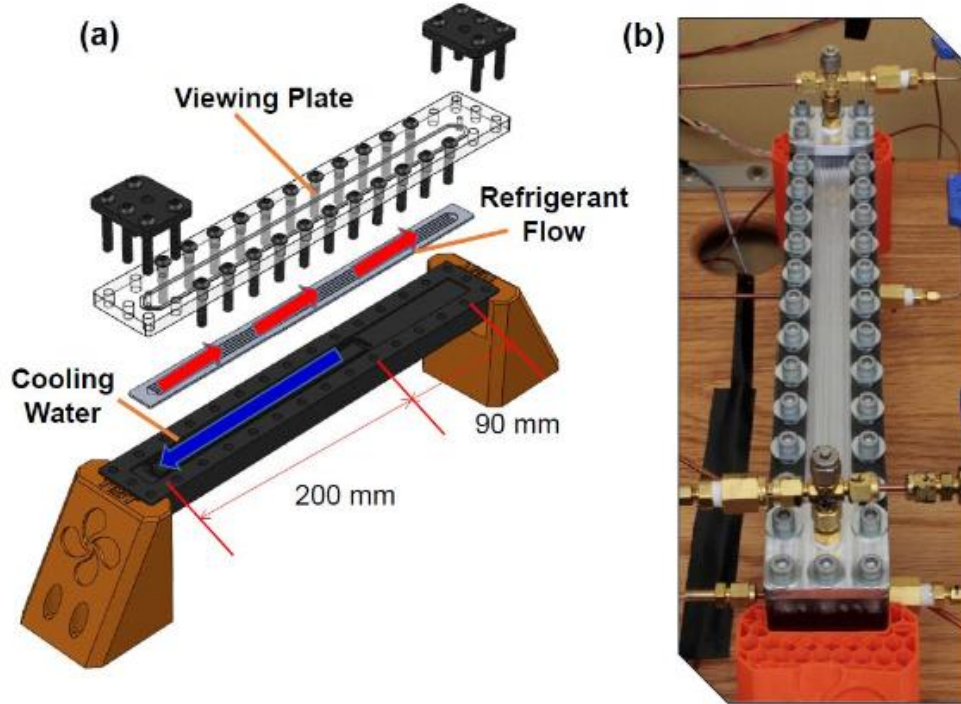


Figure 4.7: a) Schematic of test section, b) Photograph of uninsulated test section

Table 4.2: Test matrix for R134a condensation study

Two-Phase Study	Parameters	Symbol	Ranges
Operating parameters	Mass flux	$G$	75-150 $\text{Kg/m}^2\text{-s}$
	Saturation temperature	$T_{\text{sat}}$	40 °C, 55 °C
	Coolant volumetric flow rate	$\dot{V}$	9-25 ml/min
	Saturation pressure	$P_{\text{sat}}$	147.4 psi, 217.55 psi
Microchannel geometry dimensions	Cross section area	$A_c$	Rectangular
	Hydraulic diameter	$D_H$	0.84 mm
	Length of channel	$L$	200mm

#### 4.12.1. Heat transfer model

The data acquired from the experimental facility was processed by using following governing heat transfer equations. The heat transferred in the test section is calculated from an energy balance on the water flowing in the coolant section.

The heat absorbed by water from refrigerant as shown in Equation 3.

$$\dot{Q}_w = \dot{m}_w \times C_p \times (T_{out} - T_{in}) \quad 1$$

The heat transfer by refrigerant in term of enthalpies is given by Equation 4.

$$\dot{Q}_{ref} = \dot{m}_{ref} \times (h_{out} - h_{in}) \quad 2$$

$\Delta T_{in}$  and  $\Delta T_{out}$  in Equation 1 and 2 are expressed in term of the inlet and outlet temperatures and the ambient temperature.

$$\Delta T_{in} = T_{in} - T_{amb} \quad 3$$

$$\Delta T_{out} = T_{out} - T_{amb} \quad 4$$

$\Delta T_{LM}$  is a log mean temperature difference calculated from Equation 3 and 4.

$$\Delta T_{LM} = \frac{\Delta T_{in} - \Delta T_{out}}{\ln\left(\frac{\Delta T_{in}}{\Delta T_{out}}\right)} \quad 5$$

The vapor quality at the inlet of the test section of the refrigerant R134a in Equation 7. It is determined by using the enthalpies.  $H_{in}$ , is obtained from the enthalpy at the inlet of the pre-condenser, the water heat transfer rate and the refrigerant mass flow rate as shown in Equation 8. Similarly,  $x_{out}$  is the quality at outlet of microchannel determined by same way as quality at inlet of condenser except that enthalpy at the post-condenser found by heat loss [14].



$$x_{in} = \frac{h_{in}-h_l}{h_v-h_l} \quad 6$$

$$h_{in,test} = h_{in,pre} - \left| \frac{\dot{Q}_w}{\dot{m}_{ref}} \right| \quad 2$$

Where mass flux  $G$  is obtained by dividing mass flow rate of refrigerant to cross sectional area of channel as shown in Equation 6.

$$G = \frac{\dot{m}_{ref}}{A_c} \quad 8$$

#### 4.12.2. Two-Phase flow model

Martinelli parameter is a dimensionless number. Which is used to determine the volume fraction of liquid to vapors of flowing fluid in condensation two-phase flow of microchannels. It varies with the tube size and hydraulic diameter of channel. Whereas,  $J_g$  is also a dimensionless gas velocity, which describes ratio of velocity of gas to velocity of liquid in two-phase flow [15].

$$X = \left( \frac{\rho_v}{\rho_l} \right)^{0.5} \times \left( \frac{\mu_v}{\mu_l} \right)^{0.1} \times \left( \frac{1-x}{x} \right)^{0.9} \quad 9$$

$$J_g = \frac{G \times x}{\rho_g} \quad 10$$

## Summary

In this chapter, experimentation for slurry deposition is reported. The experiment is divided into two sections: Surface preparation, coating deposition followed by thermal testing that includes isothermal oxidation testing and thermal shock cycling test. In this, we have also discussed about the characterization techniques for studying the phase composition, surface morphology and, microstructure. For extending the investigation about surface morphology, image analysis was also performed to measure the surface roughness, porosity, and coating thickness.

R-134a was chosen as a working fluid due to its prevalence in the HVAC&R industry and the availability of prior work using this fluid. R-134a is in the process of being phased down due to its high global warming potential (GWP). However, the thermophysical properties are comparable to new low GWP replacements such as R-1234yf and R-513A, providing some confidence that the results of this study can be extended to new refrigerants.

The system efficiency mainly depends on design consideration for fully developed flow as well as on material aspect of flow section. In microchannel heat exchanger, effective condensation can be accomplished by enhancing effective surface area to volume ratio and, also by optimizing the saturated vapor and liquid ratio inside the channel flow section. The heat transfer in the microchannel is mainly depended on hydraulic diameter ( $D_H$ ), which is  $D_H < 1\text{mm}$  for effective condensation inside microchannel. The motivation of microchannel phase change research has been the necessity for high-heat flux removal especially from combustor section of gas turbine engine [16]–[19].

In this research paper, Refrigerant R134a is used inside horizontal rectangular microchannels at saturation temperature of 40°C, 55°C and saturation pressure of 147psi, 217psi over lower mass flux of 75-150 kg/m<sup>2</sup>-s to visualize the different flow regimes and also to compare experimental data points with the Barnea and Breber flow maps.

## References

- [1] V. Naglieri, D. Gutknecht, V. Garnier, P. Palmero, J. Chevalier, and L. Montanaro, "Optimized slurries for spray drying: Different approaches to obtain homogeneous and deformable alumina-zirconia granules," *Materials (Basel)*, vol. 6, no. 11, pp. 5382–5397, 2013.
- [2] S. Roy, S. R. Reddy, P. Sindhuja, D. Das, and V. V. B. Prasad, "AlPO<sub>4</sub>-C composite coating on Ni-based super alloy substrates for high emissivity applications: Experimentation on dip coating and spray coating," *Def. Sci. J.*, vol. 66, no. 4, pp. 425–433, 2016.
- [3] X. J. Lu and P. Xiao, "Constrained sintering of YSZ/Al<sub>2</sub>O<sub>3</sub> composite coatings on metal substrates produced from eletrophoretic deposition," *J. Eur. Ceram. Soc.*, vol. 27, no. 7, pp. 2613–2621, 2007.
- [4] W. Rasband and M. Health, "Microscopy and computer ized image analysis of wood pulp fibr es multi- scale str uctur es," no. level 1, 1997.
- [5] N. Hotaling, N. Hotaling, S. Code, and P. Analysis, "Contents 1," pp. 1–10, 2017.
- [6] J. Buckman, S. Bankole, S. Zihms, H. Lewis, G. Couples, and P. Corbett, "Quantifying Porosity through Automated Image Collection and Batch Image Processing: Case Study of Three Carbonates and an Aragonite Cemented Sandstone," *Geosciences*, vol. 7, no. 3, p. 70, 2017.
- [7] J. Ann and C. C. Berndt, "Surface Roughness of Plasma Sprayed Coatings : A Statistical Approach," *DVS*, vol. 302, pp. 599–604, 2014.
- [8] S. Bhoje, "Thermal cycling test setup design and testing of TBCs for diesel engine application," 2017.
- [9] V. G. Niño, P. S. Hrnjak, and T. A. Newell, "Two-Phase Flow Visualization of R134A in a Multiport Microchannel Tube," *Heat Transf. Eng.*, vol. 24, no. 1, pp. 41–52, Jan. 2003.
- [10] A. Kawahara, P. M.-Y. Chung, and M. Kawaji, "Investigation of two-phase flow

- pattern, void fraction and pressure drop in a microchannel,” *Int. J. Multiph. Flow*, vol. 28, no. 9, pp. 1411–1435, Sep. 2002.
- [11] J. W. Coleman and S. Garimella, “Characterization of two-phase flow patterns in small diameter round and rectangular tubes,” *Int. J. Heat Mass Transf.*, vol. 42, no. 15, pp. 2869–2881, Aug. 1999.
- [12] P. A. Kew and K. Cornwell, “Correlations for the prediction of boiling heat transfer in small-diameter channels,” *Appl. Therm. Eng.*, vol. 17, no. 8–10, pp. 705–715, Aug. 1997.
- [13] “LabVIEW - National Instruments.” [Online]. Available: <http://www.ni.com/en-lb/shop/labview.html>. [Accessed: 30-Dec-2017].
- [14] R. Suliman, L. Liebenberg, and J. P. Meyer, “Improved flow pattern map for accurate prediction of the heat transfer coefficients during condensation of R-134a in smooth horizontal tubes and within the low-mass flux range,” *Int. J. Heat Mass Transf.*, vol. 52, no. 25–26, pp. 5701–5711, 2009.
- [15] J. A. Milkie, S. Garimella, and M. P. Macdonald, “Flow regimes and void fractions during condensation of hydrocarbons in horizontal smooth tubes,” *Int. J. Heat Mass Transf.*, vol. 92, pp. 252–267, 2016.
- [16] P. Prapamonthon, H. Xu, W. Yang, and J. Wang, “Numerical Study of the Effects of Thermal Barrier Coating and Turbulence Intensity on Cooling Performances of a Nozzle Guide Vane,” *Energies*, vol. 10, no. 3, p. 362, 2017.
- [17] A. Cavallini, G. Censi, D. Del Col, L. Doretti, G. Longo, and L. Rossetto, “Condensation of Halogenated Refrigerants Inside Smooth Tubes,” *HVAC&R Res.*, vol. 8, no. 4, pp. 429–451, Oct. 2002.
- [18] “Turbine blade with micro channel cooling system,” 2009.
- [19] I. of M. R. at the G. A. Center, “Institute of Materials Research.” Institute of Materials Research at the German Aerospace Center.

# Chapter 5

## Oxidation kinetics and microstructure analysis of slurry deposited alumina on Monel 400 Superalloy

### 5.1. Isothermal oxidation testing

Weight gain curve for uncoated and coated Monel 400 alloy was shown in Figure 5.1. A progressive weight gain curve was obtained for the oxidation of uncoated Monel 400 alloy from 250-1000°C. Weight gain curve at 600°C indicated the same trend for uncoated and coated substrates. Afterwards, for coated substrate, weight gain was not observed beyond 800°C, indicating that Al<sub>2</sub>O<sub>3</sub> retarded the oxidation process (Figure 5.1). It infers from the plot that weight gain curve followed parabolic law for coated substrates (Figure 5.1).

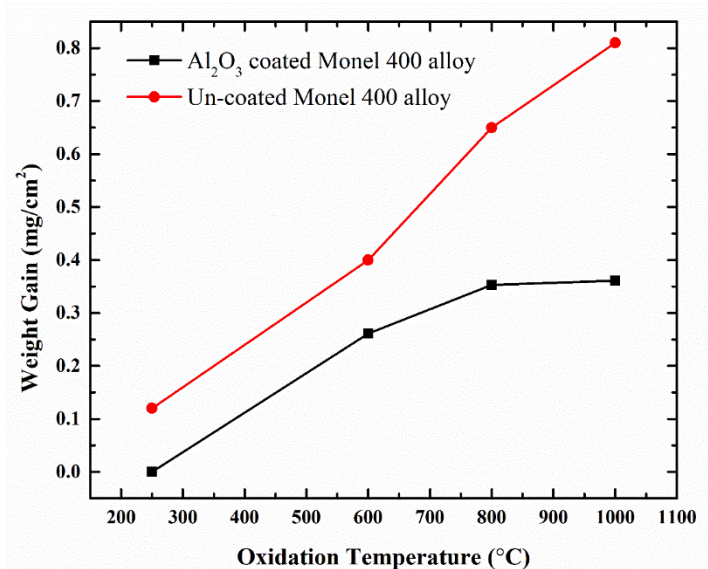


Figure 5.1; Weight gain curve for uncoated and Al<sub>2</sub>O<sub>3</sub> coated Monel 400 alloy substrate with a surface area of 5.625 cm<sup>2</sup>. Duration of each cycle was 3 h.

Table 5.1 shows the oxidation kinetics at service temperatures 600°C, 800°C, 1000°C respectively. It indicates that during sintering 600°C oxidation rate was high. While during ISOT, surface oxidation occurred but at lower rate and became negligible at 1000°C. From this, it infers that thermodynamically stable oxide scale and spinel i.e. NiO, Al<sub>2</sub>O<sub>3</sub>, CuAlO<sub>2</sub>, Fe<sub>3</sub>O<sub>4</sub>, CuFe<sub>2</sub>O<sub>4</sub>, protected the deteriorated oxidation of inner metal. The oxidation kinetics for coated

substrates was slowed down because of low diffusivity of hot gases to the coating surface (Table 5.1).

Table 5.1. Oxidation rate of slurry deposited Al<sub>2</sub>O<sub>3</sub> coated Monel 400 superalloy

Oxidation temperature (°C)	Oxidation rate ( $\Delta m/A$ ) <sup>2</sup> /t [mg <sup>2</sup> /cm <sup>4</sup> ·s <sup>-1</sup> ]
600	0.24 e <sup>-10</sup>
800	0.115 e <sup>-10</sup>
1000	0.116 e <sup>-10</sup>

## 5.2. XRD analysis

Figure 5.2 shows the XRD analysis for the uncoated and coated Monel 400 alloy before and after oxidation.  $\alpha$ - Al<sub>2</sub>O<sub>3</sub> (104) used in this study exhibited hexagonal structure and the Monel 400 alloy single crystal (111) exhibited a cubical structure. For uncoated oxidized substrates, low-intensity peaks with minute concentration of Cu<sub>2</sub>O and FeO were observed. Although stable oxide scale NiO and CuO was not formed at the surface (Figure 5.2c). For the coated substrates, XRD pattern indicates the formation of oxide scale NiO, CuO along with the protective spinel oxides CuAlO<sub>2</sub>, Fe<sub>3</sub>O<sub>4</sub>, CuFe<sub>2</sub>O<sub>4</sub> and NiMn<sub>2</sub>O<sub>4</sub>. The miller indexes are (200), (002), (012), (311), (311) and (311) with the corresponding 2 $\theta$  degree values of, 43.38, 35.382, 37.853, 35.41, 35.438 and 35.40 respectively (Figure 5.2d). However, Cu<sub>2</sub>O formation belonged to initial oxidation of Cu, was not observed in upper oxide scale for coated substrate.

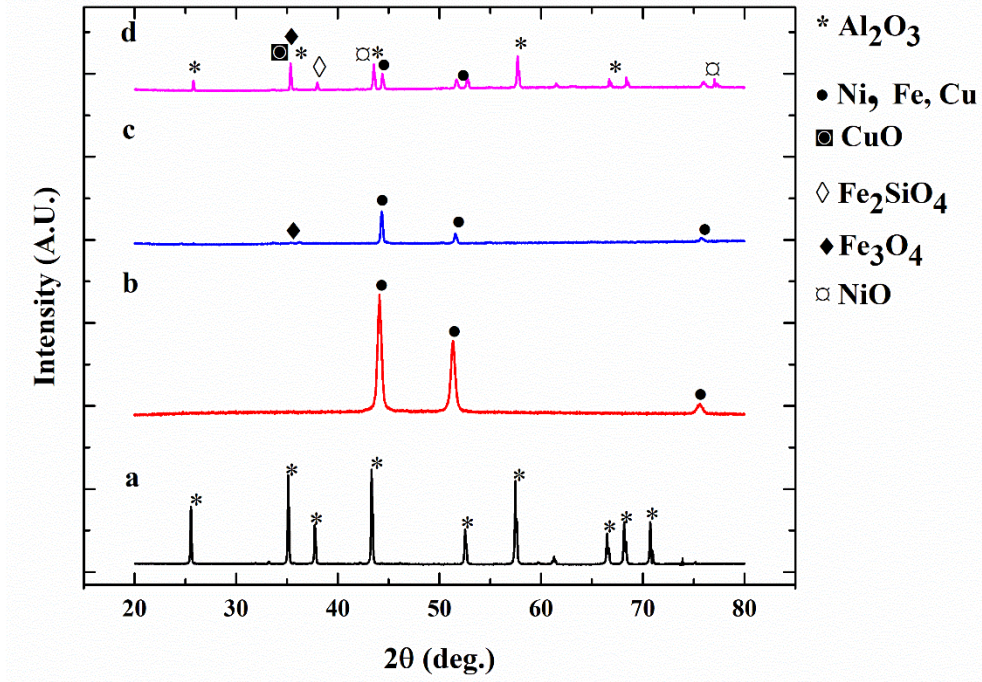


Figure 5.2. XRD analysis of a)  $\text{Al}_2\text{O}_3$  Powder, b) Monel 400 Superalloy, c) Uncoated oxidized at  $1000^\circ\text{C}$ , d) Torn off surface after ISOT of  $\text{Al}_2\text{O}_3$  coated Monel 400 superalloy at  $1000^\circ\text{C}$

### 5.3. SEM analysis

Figure 5.3, shows the SEM micrograph of oxidized  $\text{Al}_2\text{O}_3$  coated Monel 400 superalloy. In the figure 5.3(a), a densified coating structure was observed with few pinholes and longitudinal cracks with a short length. It indicates the good bonding of  $\text{Al}_2\text{O}_3$  coating with Monel 400 superalloy. Pin-holes and surface crack facilitated the conduction of heat flux and enhanced the thermal conductivity at high temperature.

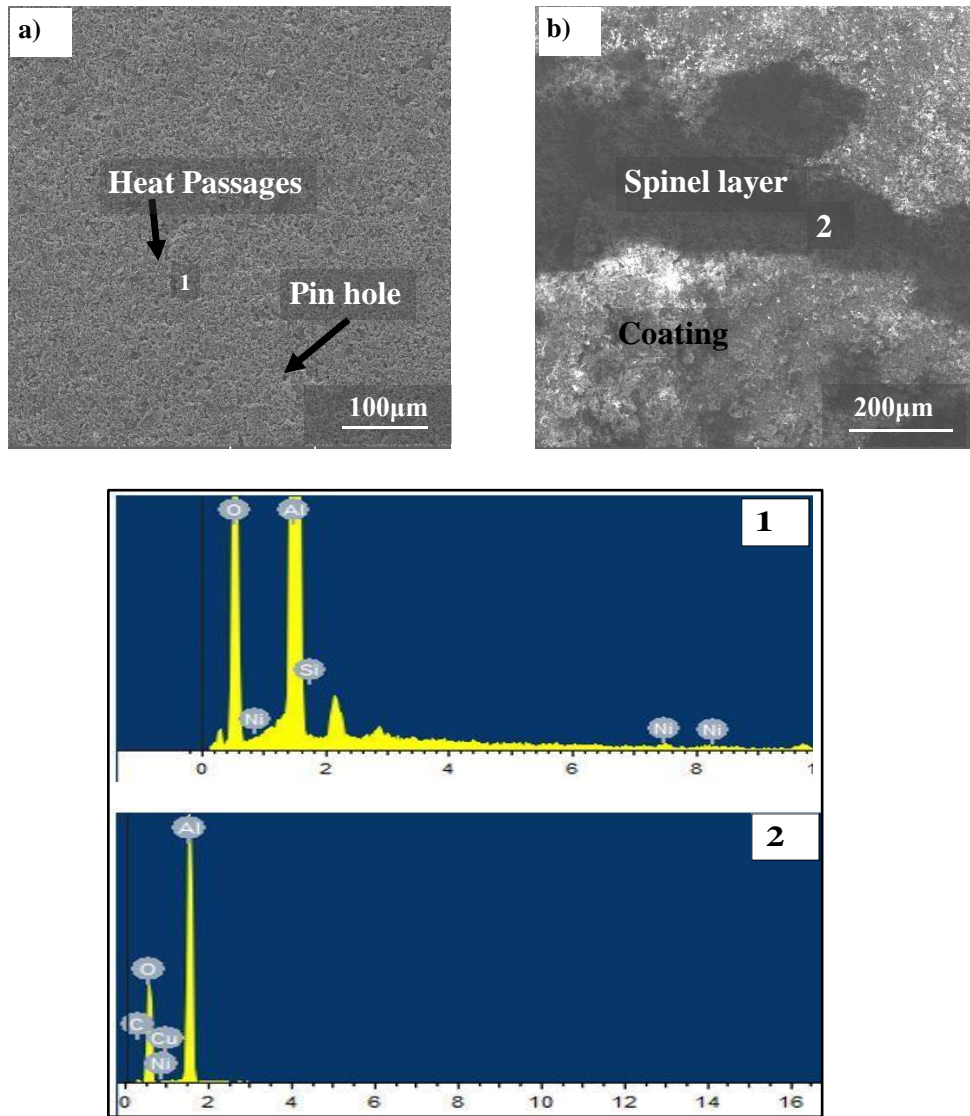


Figure 5.3. SEM and EDS analysis of  $\text{Al}_2\text{O}_3$  coated Monel 400 a) the coating morphology after ISOT at 800°C b) after isothermal oxidation test at 1000°C, c) point analysis of coating, d) EDS analysis of surface crack at 1000°C

Table 5.2, shows the EDS analysis of oxidized coated substrate at temperatures 800°C and 1000°C (Figure 5.3a-b) to get an understanding of oxidation mechanism at the internal surface layer. Point analysis of coating confirmed that  $\text{Al}_2\text{O}_3$  and NiO were present at the coating surface, but EDS analysis does not show the presence of CuO (Table 5.2). EDS at crack region



indicates the higher concentration of Al and Ni that indicates the stability of oxides at the surface (Osorio, Toro and Hernandez-Ortiz, 2012).

Table 5.2. EDS analysis of Al<sub>2</sub>O<sub>3</sub> deposited Monel 400 after isothermal oxidation test at 800°C and 1000°C a) the coating morphology after ISOT at 800°C b) At the torn off surface of coating at 1000°C

Element	EDS (a)		EDS 2 (b)	
	Weight%	Atomic%	Weight%	Atomic%
O K	55.65	68.04	59.84	67.02
Al K	43.80	31.75	31.91	21.19
Si K	0.08	0.06	--	--
Ni K	0.47	0.16	7.81	11.65
C K	--	--	0.02	0.01
Cu K	--	--	0.41	0.12
Total	100.00		100.00	

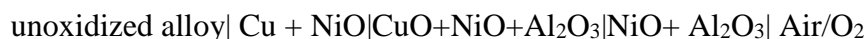
## 5.4. Discussion

The coated Monel 400 substrates show a lower oxidation rate as compared to uncoated substrates. This indicated that thick oxide scale was composed of NiO (Zhang et al., 2017) (Karl Hauffe, 1965). The weight gain reduction for coated substrates was ½ fraction of uncoated substrates. The XRD analysis of the oxidized surface of coated substrates revealed the existence of thermodynamically stable oxide scale and spinel oxides of CuAlO<sub>2</sub>, Fe<sub>3</sub>O<sub>4</sub>, CuFe<sub>2</sub>O<sub>4</sub> and NiMn<sub>2</sub>O<sub>4</sub>. For uncoated substrates, Cu<sub>2</sub>O formation was observed and predominates the oxidation of bare substrates. At 600°C, oxidation kinetics involves the formation of Cu<sub>2</sub>O and NiO (Karl Hauffe, 1965). However, in this study, at 600°C to 1000°C, NiO predominated the oxidation process for coated substrates.

Coating durability depends on the thermal and mechanical response of coating to i.e. excessive oxide growth, volumetric expansion and diffusion of oxygen. During sintering process, volumetric expansion evolved residual tensile stresses and discouraged the bonding between

coating and substrate. Although sintering process involved the pores' re-distribution, healing up the cracks and shifting of the grain boundaries. The excessive growth of oxide scale started to compel coating from the substrate surface and proceed towards delamination of coating (Osorio, Toro and Hernandez-Ortiz, 2012).  $\text{Al}_2\text{O}_3$  has low thermal conductivity and a very good match of coefficient of thermal expansion with the Monel 400 superalloy. At  $1000^\circ\text{C}$ , the formation of gaseous oxide weakened the interface and participated in the cracking of coating (Pettit and Meier, 1984). Volatile oxides e.g.  $\text{CuO}$ , started to evaporate at  $1000^\circ\text{C}$  and caused propagation of cracks at the coating surface (Table 5.2). The growth of oxide scale with spinel formation collectively affect the coating sustainability. During cooling, thermal expansion mismatch between coating and substrate caused residual compressive stresses that caused undulation at the surface. These all factors participate in the oxidation kinetics at high temperature. Oxidation kinetics depends on the surface microstructure and thermal conductivity of coating.

Although coating prevented the surface of Monel 400 alloy from being ruptured and cracked but coating itself was cracked. Crack region shows a higher amount of oxygen, Ni but a little percentage of Cu which indicates the evaporation of  $\text{CuO}$  above  $800^\circ\text{C}$ . Based on above discussion, Figure 5.5, illustrated the oxidation mechanism at the surface of coated Monel 400. It indicates that oxide scale bonded with the  $\text{Al}_2\text{O}_3$  and got stabilized. Thermodynamically stable spinel oxides i.e.  $\text{NiO}.\text{Al}_2\text{O}_3$  and  $\text{CuO}.\text{Al}_2\text{O}_3$  reduced the thermal stresses (Zhang et al., 2017). Sintering at  $600^\circ\text{C}$  aims to promote thermodynamically  $\text{NiO}$  formation that safeguard the inner metal up-to  $1300^\circ\text{C}$  after this it becomes volatile.  $\text{NiO}$  formation predominated the oxidation mechanism from  $500^\circ\text{C}$ - $800^\circ\text{C}$  with Gibbs free energy  $\Delta G_b^0$  of  $150 \text{ kJ/g}$  atom oxygen (Pettit and Meier, 1984). It is inferred from the analysis that  $\text{NiO}$  oxide scale protected the alloy from further oxidation (Figure 6). The oxidation at specific temperature termed as selective oxidation (Seraffon et al., 2011). Based on XRD and SEM/EDS analysis, the protective zone has following composition:



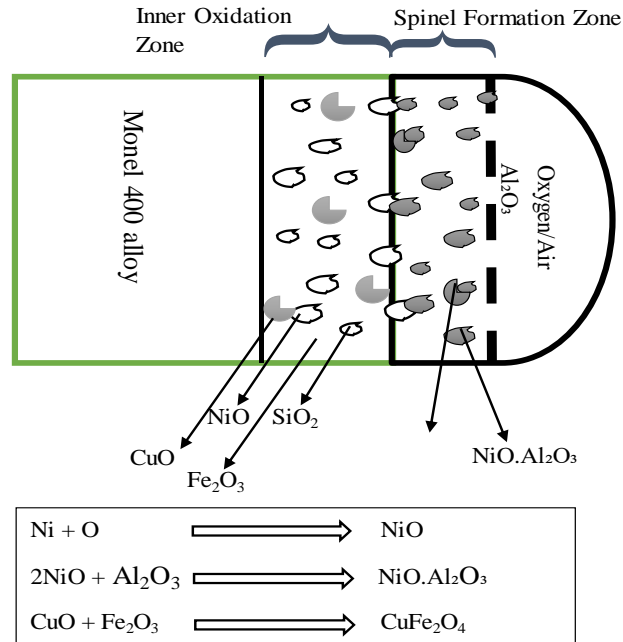


Figure 5.4. Schematic representation of inner oxidation mechanism and formation of spinel as an additional protective layer above the Monel 400 superalloy surface below the Al<sub>2</sub>O<sub>3</sub> coating

Figure 5.5 shows the crack free, adhering oxide layer at the surface of Monel 400 alloy. The image was taken from the cracked part of coating. As indicated that spinel oxides covered the surface and hindered the diffusion of oxygen beyond the oxide layer that was confirmed by weight gain curve. Parabolic rate law indicates the formation of oxide scale mainly consisted of NiO. Al<sub>2</sub>O<sub>3</sub> coating provided a sufficient protection to Monel 400 alloy.

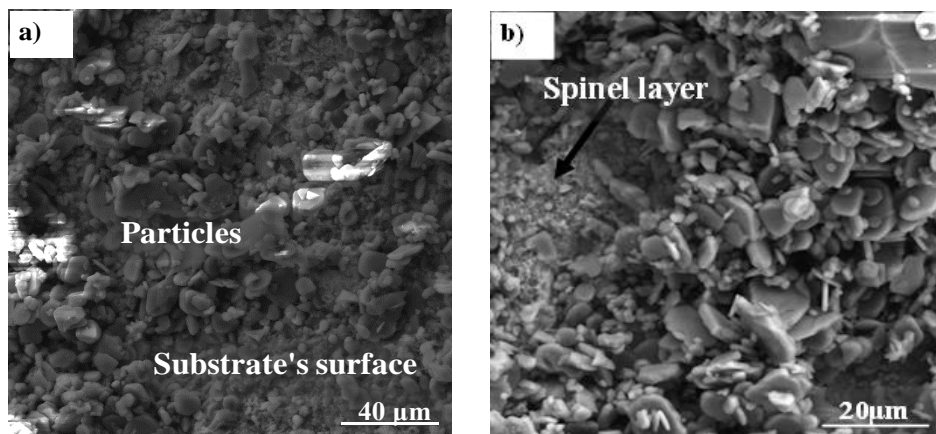


Figure 5.5. Monel 400 surface after removing a certain part of coating a) Spinel oxides, b) microstructure of spinel region

## 5.5. Thermal conductivity, porosity and pore distribution

Figure 5.6 (a-b) shows the surface microstructure of  $\text{Al}_2\text{O}_3$  coating before and after sintering respectively. Figure 5.6(a) shows that surface microstructure consisted of an uniform distribution of pores and microcrack. Before sintering, about 17 % surface porosity was measured via Image J software. Figure 5.6(b) shows a nano/microporous surface microstructure that increased the durability of coating. Thermal conductivity of coating depends on the pore fraction and morphology i.e. pore size and their shape. Higher porosity (nano/micropores) reduces the thermal conductivity while a lower porosity (macropores) increases the thermal conductivity of coating. Porous microstructure vanishes the thermal stresses generated at the interface. Air (thermal conductivity= 0.024 W/m·K (Cengel, 2002)) because of gravitational or surface tension forces, entrapped inside the pores and reduced the heat conduction through the coating. It is noted that surface tension effect predominates in nano/micropores while gravitational impact dominates in macropores and segmentation cracks. Although the study of heat transfer across nano/microporous coating still needs attention. For a good thermal barrier, certain fraction of pores is prerequisite. Figure 5.6(a) shows a large amount of microcracks those were filled with spinel oxides, i.e. NiO, CuO after sintering (Figure 5.6b). Sintering process reshape the surface microstructure of coating with a decrease in porosity and surface roughness from 17 % to 12% and  $7\mu\text{m}$  to  $2.5\mu\text{m}$  respectively. The average pore shape was measured to be  $1.37\mu\text{m} \pm 0.9$  via Image J software (Figure 5.6).

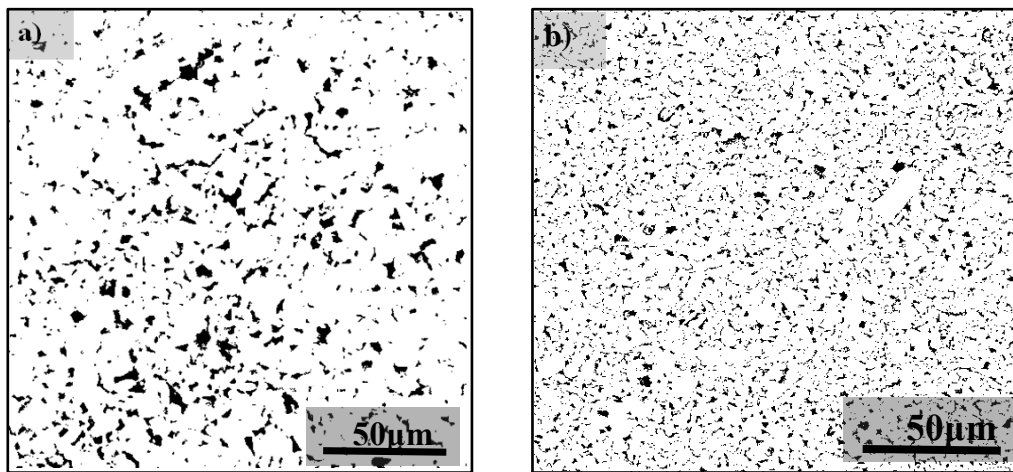


Figure 5.6. Pore size shrinkage and distribution, a) before sintering, b) after sintering

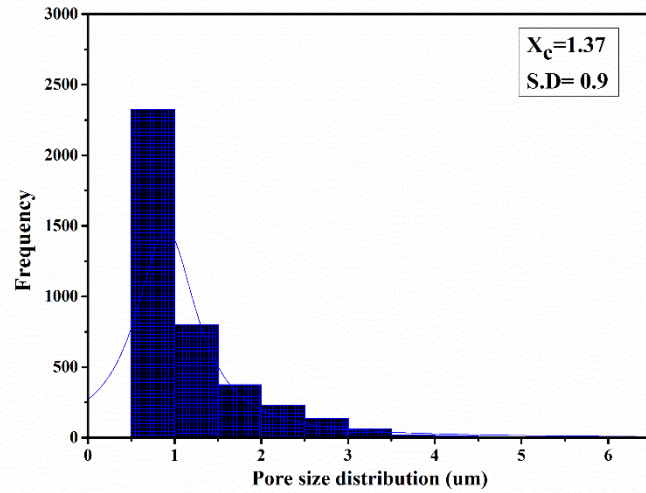


Figure 5.7. Pore size distribution after air-sintering at 600°C

Figure 5.8 indicates the inverse relation of thermal conductivity and porosity for four different porosity fractions. The porosity was determined to be 12-17% over the course of study. It is found that porosity was the dominant factor for controlling the thermal conductivity of coating. Instead of pores' characteristics, thermal conductivity also depends on the crack length, crack diameter and crack orientation (Jang and Matsubara, 2005; Zhao et al., 2006). Heat flux is propagated through phonon (thermal energy carriers) at high temperatures via convection and radiative heat transfer. Phonons are scattered through pore spaces and conduction across nano/micropores provides high thermal insulation.

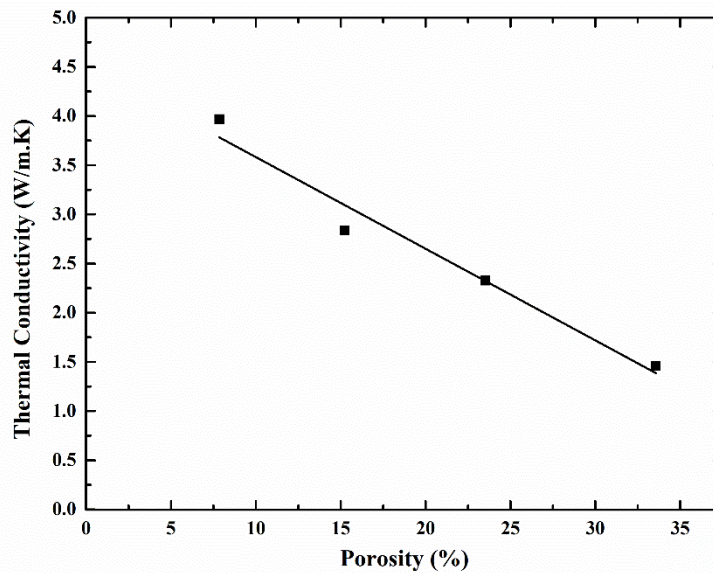


Figure 5.8. Effect of porosity on the thermal conductivity of Al<sub>2</sub>O<sub>3</sub> coating at 1000°C

This is consistent from the results that porosity provides a considerable impetus to reduce the thermal conductivity for Al<sub>2</sub>O<sub>3</sub> coatings (Shimizu et al., 2013; Askari, Taheri and Hejazi, 2015; A K Krella et al., 2016). Literature reported that pore fraction up to 40% have considerable effect on the thermal conductivity. Pore fraction greater than 40% will have direct relation with the thermal conductivity because at high temperature radiative heat transfer will be more effective (Shimizu et al., 2013). Thermal conductivity of 12 % porosity Al<sub>2</sub>O<sub>3</sub> coatings was measured via Serial parallel law reported in (Russell, 1935; Shimizu et al., 2013)

Slurry based coatings have flatten microstructure with roughness parameter in few microns. Such kind of coatings can address the challenge of CMAS (calcium, aluminium, magnesium and silica) deposition in the columnar structure of EB-CVD, EB-PVD, etc coatings (Zhao et al., 2006). Flatten coating structure increases the heat outflow along with encounter the CMAS attack on the coating durability.

## Summary

A single layer  $\text{Al}_2\text{O}_3$  based ETBC system was deposited on Monel 400 Superalloy via slurry dip coating process instead of the complex multi-layered system. The results showed that selective oxidation resulted in the transformation of single layer coating system into composite coating system. XRD analysis confirms the formation thermodynamically stable protective spinel oxides i.e.  $\text{NiO} \cdot \text{Al}_2\text{O}_3$  and  $\text{CuO} \cdot \text{Al}_2\text{O}_3$ ,  $\text{CuAlO}_2$ ,  $\text{Fe}_3\text{O}_4$ ,  $\text{CuFe}_2\text{O}_4$  and  $\text{NiMn}_2\text{O}_4$ . Based on oxidation kinetics, inner and outer zones were recognized as protective layer during sintering process. Coated substrates showed less weight gain as compared to uncoated substrates. Nano/microporous coating tended to decrease the thermal conductivity which could be controlled by particle size and sintering process.

Hence study concluded that nano/micropores coating prepared by slurry deposition are become cost effective for attaining the lower thermal conductivity at high temperature. Authors recommend the research of slurry-based coatings in terms of dip coating speed, heat transfer via nano/microporous surface. Because these coatings exhibit high porosity and low roughness profile.

## References

- [1] J. D. Osorio, A. Toro, and J. P. Hernandez-Ortiz, "Thermal barrier coatings for gas turbine applications: failure mechanisms and key microstructural features," *Dyna*, vol. 79, no. 176, pp. 149–158, 2012.
- [2] F. O. Soechting, "A Design Perspective on Thermal Barrier Coatings," *Journal of Thermal Spray Technology*, vol. 8, no. December, pp. 505–511, 1999.
- [3] R. Eriksson, "High-temperature degradation of plasma sprayed thermal barrier coating systems," Linkoping University, 2011.
- [4] K. N. Lee, "Protective coatings for gas turbines," *The gas turbine handbook*, pp. 419–437, 2006.
- [5] M. K. Chyu and S. C. Siw, "Recent Advances of Internal Cooling Techniques for Gas Turbine Airfoils," *Journal of Thermal Science and Engineering Applications*, vol. 5, no. 2, p. 21008, 2013.
- [6] J. D. Whittenberger, "HIGH-TEMPERATURE MECHANICAL PROPERTIES OF A ZIRCONIUM-MODIFIED, PRECIPITATION-STRENGTHENED NICKEL -30 PERCENT COPPER ALLOY," 1974.
- [7] K. D. Ramkumar, N. Arivazhagan, S. Narayanan, and D. Mishra, "Hot Corrosion Behavior of Monel 400 and AISI 304 Dissimilar Weldments Exposed in the Molten Salt Environment Containing  $\text{Na}_2\text{SO}_4 + 60\% \text{V}_2\text{O}_5$  at  $600^\circ\text{C}$  . Experimental Procedure," *Materials Research*, vol. 17, no. 5, pp. 1273–1284, 2014.
- [8] G. Gdowski, "Long-Term Corrosion/Oxidation Studies Under Controlled Humidity Conditions," 1997.
- [9] B. K. Jang and H. Matsubara, "Influence of rotation speed on microstructure and thermal conductivity of nano-porous zirconia layers fabricated by EB-PVD," *Scripta Materialia*, vol. 52, no. 7, pp. 553–558, Apr. 2005.
- [10] C. U. Hardwicke and Y. C. Lau, "Advances in thermal spray coatings for gas turbines and energy generation: A review," *Journal of Thermal Spray Technology*, vol. 22, no. 5, pp. 564–576, 2013.
- [11] K. Ito, H. Kuriki, H. Araki, S. Kuroda, and M. Enoki, "Detection of segmentation cracks in top coat of thermal barrier coatings during plasma spraying by non-contact



- acoustic emission method.,” *Science and technology of advanced materials*, vol. 15, no. 3, p. 35007, Jun. 2014.
- [12] P. W. Schilke, “Advanced Gas Turbine Materials and Coatings,” *GE Energy*, 2004.
- [13] M. Oksa, “Nickel and iron based HVOF thermal spray coatings for high temperature corrosion protection in biomass fired power plant boilers,” *JULKAISIJA - UTGIVARE*, 2015.
- [14] L. Wang *et al.*, “Effect of interface on the thermal conductivity of thermal barrier coatings: A numerical simulation study,” *International Journal of Heat and Mass Transfer*, vol. 79, pp. 954–967, 2014.
- [15] B. Baufeld, O. van der Biest, and H.-J. Raetzer-Scheibe, “Thermal and Mechanical Properties of Zirconia Coatings Produced By Electrophoretic Deposition,” *Advanced Ceramic Coatings and Interfaces II*, vol. 28, no. 3, pp. 3–10, 2008.
- [16] Z. S. Khan *et al.*, “Thermal cycling behavior and hot corrosion performance of the plasma sprayed Er<sub>2</sub>Si<sub>2</sub>O<sub>7</sub> coatings deposited on Cf/SiC composites,” *Journal of Asian Ceramic Societies*, vol. 3, no. 1, pp. 123–129, 2014.
- [17] S. Roy, S. R. Reddy, P. Sindhuja, D. Das, and V. V. B. Prasad, “AlPO<sub>4</sub>-C composite coating on Ni-based super alloy substrates for high emissivity applications: Experimentation on dip coating and spray coating,” *Defence Science Journal*, vol. 66, no. 4, pp. 425–433, 2016.
- [18] H. Zhang, Y. Liu, X. Chen, H. Zhang, and Y. Li, “Microstructural homogenization and high-temperature cyclic oxidation behavior of a Ni-based superalloy with high-Cr content,” *Journal of Alloys and Compounds*, vol. 727, pp. 410–418, 2017.
- [19] V. Sankar, “Thermal Barrier Coatings Material Selection , Method of Preparation and Applications - Review,” *International Journal of Mechanical Engineering and Robotics Research*, vol. 3, no. 2, pp. 510–517, 2014.
- [20] I. A. Mahmood, W. W. Jameel, & Lubna, and A. Khaleel, “Improved oxidation resistance for thermal barrier ceramic coating protect,” *International Journal of Research in Engineering & Technology*, vol. 1, no. 5, pp. 2321–8843, 2013.
- [21] A. K. Krella, A. T. Sobczyk, A. Krupa, and A. Jaworek, “Thermal resistance of Al<sub>2</sub>O<sub>3</sub> coating produced by electrostatic spray deposition method,” *Mechanics of Materials*,

- vol. 98, pp. 120–133, 2016.
- [22] X. J. Lu and P. Xiao, “Constrained sintering of YSZ/Al<sub>2</sub>O<sub>3</sub> composite coatings on metal substrates produced from eletrophoretic deposition,” *Journal of the European Ceramic Society*, vol. 27, no. 7, pp. 2613–2621, 2007.
- [23] S. K. Khaja-abdul, “SLURRY BASED COATINGS ON SILICON BASED CERAMICS,” Cleveland State University, Cleveland OHIO, 2006.
- [24] S. M. Corporation, “Physical and thermal properties of Monel 400 alloy.” Special Metals Corporation, 2005.
- [25] Karl Hauffe, *Oxidation of Metals*, German Edi. Springer US, 1965.
- [26] F. S. Pettit and G. H. Meier, “Oxidation and Hot Corrosion of Superalloys,” *Superalloys 1984 (Fifth International Symposium)*, pp. 651–6877, 1984.
- [27] f. s. pettit and g. h. meier, “oxidation and hot corrosion of superalloys.”
- [28] M. Seraffon, N. J. Simms, J. R. Nicholls, J. Sumner, and J. Nunn, “Performance of thermal barrier coatings in industrial gas turbine conditions,” *Materials at High Temperatures*, vol. 28, no. 4, pp. 309–314, 2011.
- [29] Y. Cengel, “Heat Transfer: A Pratical Approach,” *McGraw - Hill*, p. 932, 2002.
- [30] H. Zhao, F. Yu, T. D. Bennett, and H. N. G. Wadley, “Morphology and thermal conductivity of yttria-stabilized zirconia coatings,” 2006.
- [31] T. Shimizu, K. Matsuura, H. Furue, and K. Matsuzak, “Thermal conductivity of high porosity alumina refractory bricks made by a slurry gelation and foaming method,” *Journal of the European Ceramic Society*, vol. 33, no. 15–16, pp. 3429–3435, Dec. 2013.
- [32] R. Askari, S. Taheri, and S. H. Hejazi, “Thermal conductivity of granular porous media: A pore scale modeling approach,” *AIP Advances*, vol. 5, no. 9, p. 97106, Sep. 2015.
- [33] A. K. Krella, A. T. Sobczyk, A. Krupa, and A. Jaworek, “Thermal resistance of Al<sub>2</sub>O<sub>3</sub> coating produced by electrostatic spray deposition method,” *Mechanics of Materials*, vol. 98, pp. 120–133, 2016.
- [34] H. W. Russell, “PRINCIPLES OF HEAT FLOW IN POROUS INSULATORS,” *Journal of the American Ceramic Society*, vol. 18, no. 1–12, pp. 1–5, Dec. 193

# Chapter 6

## Thermal shock testing and microstructure analysis of slurry deposited alumina on C/SiC composite

### 6.1. Characteristics of as-deposited Al<sub>2</sub>O<sub>3</sub> coating

Figure 6.1. is the camera and SEM images of uncoated C/SiC composite as well as of as-deposited Al<sub>2</sub>O<sub>3</sub> coating on the surface of C/SiC composite with a deposition efficiency of 58% calculated by dividing the material deposited to the material consumed during the deposition process.

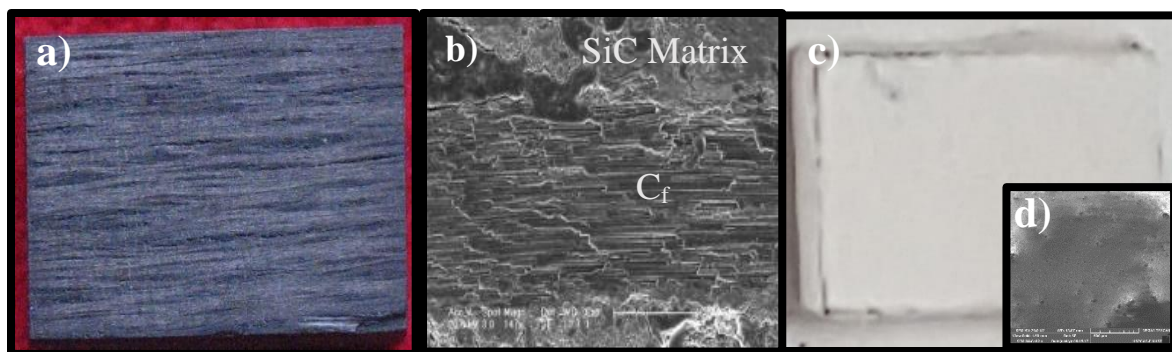


Figure 6.1: a) Camera image of C/SiC composite coupon before slurry deposition; (b) SEM image of uncoated C/SiC composite coupon; (c) camera image of coated coupon; (d) inset is of as-deposited Al<sub>2</sub>O<sub>3</sub> coating vacuum dried at 250°C;

It has been observed that graded coating structure with size distribution from 1-5  $\mu\text{m}$  resulting in smooth coating surface. PEI has improved the rheology of slurry and developed a well interlocking between coating and substrate surface. Although certain extrusions are found that because of the graded coating structure distributed all around the coating surface. Small sized and large sized particles are arranged coherently for developing a dense thermal shield with a porosity of about 15 %.

## **6.2. Characterization study of Al<sub>2</sub>O<sub>3</sub> Coating**

According to literature, a thermal barrier coating should have good surface adherence with optimum porosity. A good thermal barrier coating system should have 3-20% porosity that facilitates the thermal conduction and helps to overcome the CTE mismatch between substrate and coating material . It should be thermally and chemically inert with phase stability when exposed to High-Temperature. Al<sub>2</sub>O<sub>3</sub> with a high melting point, high thermal conductivity, the moderate coefficient of thermal expansion, and with phase stability is an ideal candidate for protection of C/SiC composite against high-temperature oxidation. Al<sub>2</sub>O<sub>3</sub> also with poor oxygen diffusivity and zero water absorptivity has strong environmental and thermal barrier applicability. Due to low oxygen permeability, Al<sub>2</sub>O<sub>3</sub> resists the growth of thermally grown oxides (TGOs) to increase the thermal cycle lifetime by reducing the production of thermal stresses that weaken the mechanical strength of coating structure. One of the shortcomings of Al<sub>2</sub>O<sub>3</sub> is its brittleness and low fracture toughness at High-Temperature [1]. Graded coating structure was designed to overcome this failure risk. Particle size and shape were improved by manual grinding the powders. SiC matrix not only provide toughness to carbon composites but also ensure the provision of silica within coating layer due to the good mobility of silicon towards the surface at high-temperature oxidation. SiO<sub>2</sub> formed at 600°C has the tendency to fill up the cracks present on the surface those were developed due to high-temperature oxidation [2–4].

### **6.2.1. Sintering at 800°C for the densification of coating**

As deposited Al<sub>2</sub>O<sub>3</sub> coated C/SiC composite was dried in vacuum oven at 250°C and 0.07 MPa for a duration of 2 hrs. to remove the entrapped moisture and PEI. The first goal of the heat treatment is to remove the binder from the coating surface that resulted in porous coating structure. The voids are the sites for oxygen diffusion during high-temperature sintering of Al<sub>2</sub>O<sub>3</sub> coated C/SiC composite. Graded coating structure filled up the voids, cavities and microcracks originated after removal of binder.

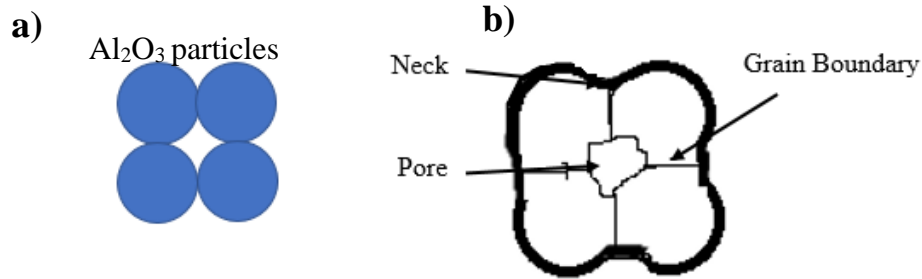


Figure 6.2: a)  $\text{Al}_2\text{O}_3$  particles before sintering, b) After sintering at  $800^\circ\text{C}$ , grain boundary shift

It also restricts the penetration of excessive oxygen to the surface that will cause the oxidation of carbon fiber but permit a reasonable amount of oxygen that is necessitated for bonding of  $\text{Al}_2\text{O}_3$  coating with the coupon surface. It will control the growth of thermally grown oxides (TGOs) at the interlayer which further reduces the failure risk due to suppression of interfacial residual stresses at the interjunction when exposed to the high-temperature environment [1]. Figure 6.2, illustrated the effect of sintering on the grain boundary shift of  $\text{Al}_2\text{O}_3$  at  $800^\circ\text{C}$ . It is observed that after sintering at  $800^\circ\text{C}$ , graded coating structure becomes densified because high-temperature ceramics get rid of grain boundaries and shifted towards the low energy state during sintering. The shift from high energy to low energy state decreases the porosity while increases the density of coating structure due to hot pressing effect [5][6].

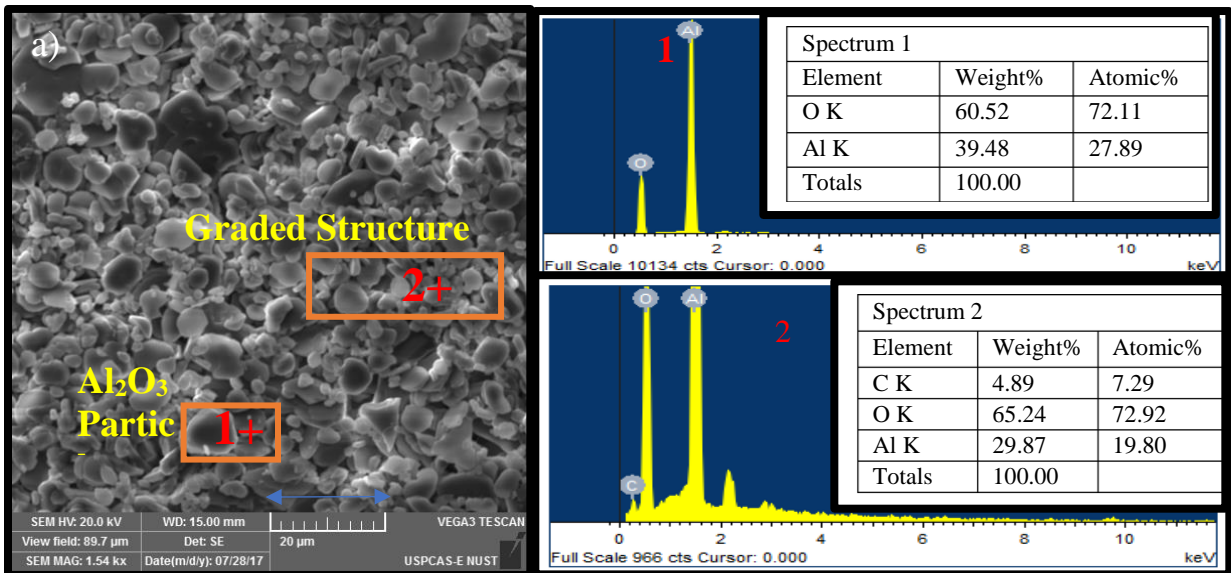


Figure 6.3: SEM micrograph and image analysis description of  $\text{Al}_2\text{O}_3$  coated coupon; a) After sintering at  $800^\circ\text{C}$  for 3 hrs. in static air (1-2) EDS analysis after sintering;

### 6.3. XRD analysis of powder and Sintered coating

#### 6.3.1. Effect of sintering on the microstructure of coating

Fig. 6.4. shows the mass change rates of multiple  $\text{Al}_2\text{O}_3$  coated C/SiC composite specimens after air-sintering at 1073 K. After sintering, an average mass change rate of  $0.033 \text{ mg/s.cm}^2$  and corresponding surface porosity of 12% (average of 3-specimens) was observed. It can be seen from Fig. 6.2(a) that the as-deposited coating was composed of hexagonal  $\text{Al}_2\text{O}_3$  with high-intensity peaks according to ICSD # 78-2427. Fig. 6.2(b) shows the appearance of  $\text{SiO}_2$  produced by passive oxidation of SiC during sintering process according to equation 4 and 5.  $\text{SiO}_2$  surrounded the alumina particles and sealed up the cracks and voids.

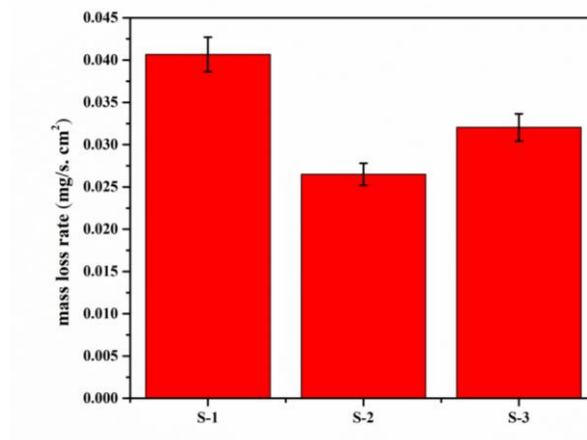


Figure 6.4: Mass change rate after air-sintering of Alumina-coated C/SiC composite at 1073 K for 3 h

Fig. 6.5 (b) indicates that  $\text{Al}_2\text{SiO}_5$  was formed at  $2\theta$  of  $35.66^\circ$  and  $60.04^\circ$ , confirmed by ICSD patterns 73-1763 and 74-2217 with phase structure of orthorhombic and triclinic. It is indicated that liquid  $\text{SiO}_2$  surrounded the  $\text{Al}_2\text{O}_3$  particles and gripped tightly after cooling. The presence of  $\text{SiO}_2$  at the surface indicates that the cracks were filled up with  $\text{SiO}_2$  that strengthened the interfacial bonding and enhanced the ductility of the coating.

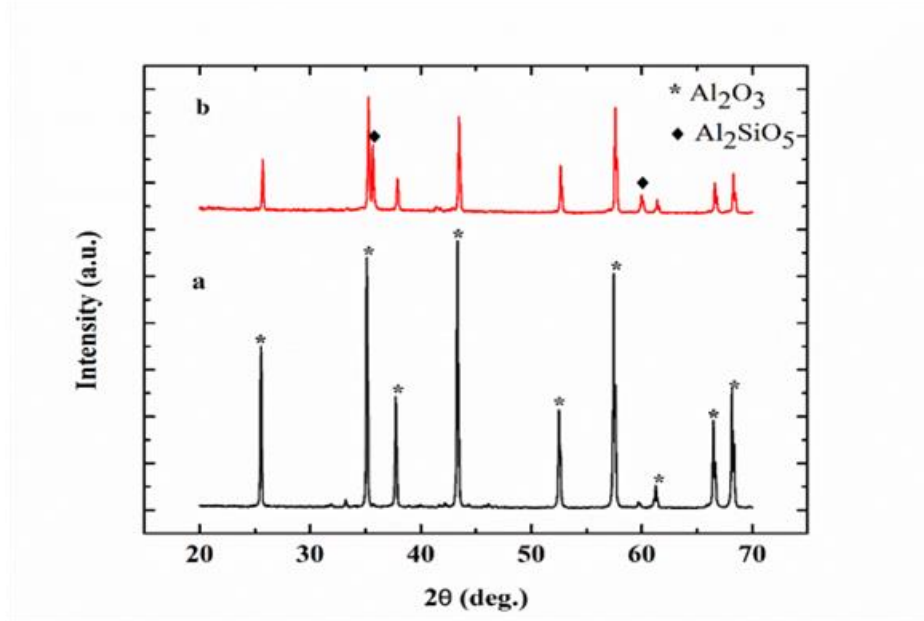


Figure 6.5: XRD spectra of Al<sub>2</sub>O<sub>3</sub> coating (a) before and (b) after sintering at 1073 K

#### 6.4. SEM analysis of Alumina coating

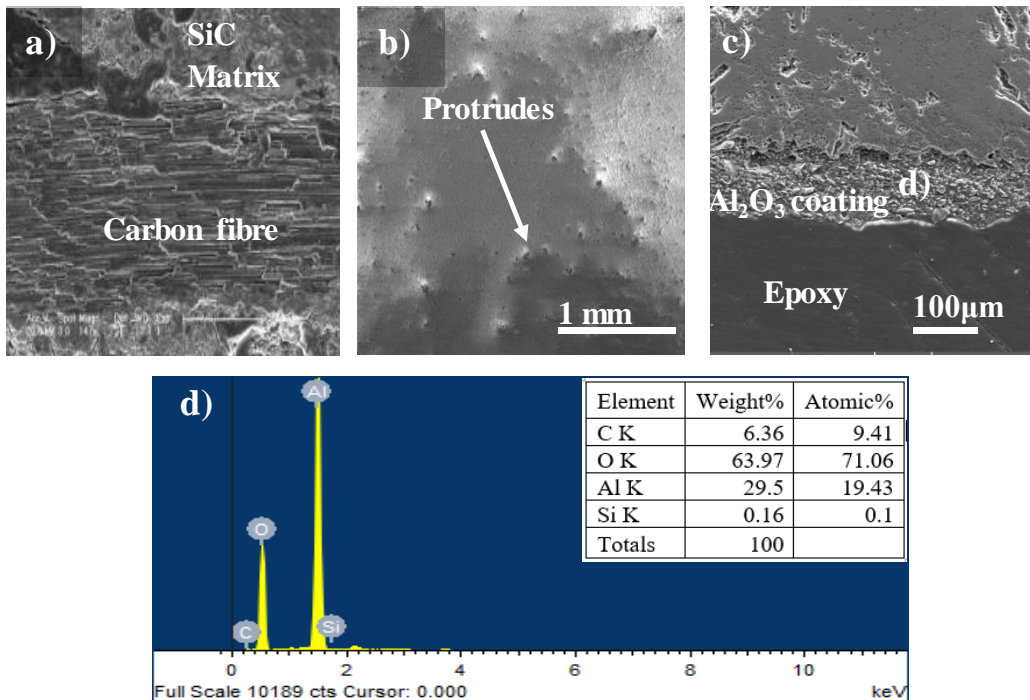


Figure 6.6: SEM image of (a) C/SiC; (b) As-deposited coating; (c) cross-section of sintered coating sintered coating, and (d) EDS spectra of alumina coating after sintering

Fig. 6.6(a) is the SEM image of C/SiC composite that indicated the embedment of SiC matrix between the fibers. Fig. 4b shows the smooth surface of the as-deposited coating with some protrusions on it. The development of protrusions is attributed to agglomeration of particles at the surface. Slurry coating process resulted in smooth coatings with appropriate coating thickness (100–400  $\mu\text{m}$ ). Slurry coat and coating thickness depends on the particle loading of slurry; high particle loading results in thick coating, but it can affect the adherence of coating. In this study, successive 3–5 dip-coats of slurry resulted in coating thickness of about 250–400  $\mu\text{m}$ . Fig. 6.6(c) shows the cross-section of coating that is homogenous, crack free and densified in nature. Coating thickness was measured via ImageJ analysis software.

Fig. 6.7 (a–c) and Fig. 6.7 (d–f) show the microstructure of coating before and after sintering process, respectively. Fig. 6.7 (b) shows the binary image of the as-deposited coating, which shows the distribution of smaller and larger pores all over the surface with an average pore size of 2.04  $\mu\text{m}$ . High solid loading of slurry-based coating resulted in dense microstructure with a thick layer.

Upon sintering, the surface cracks were sealed by  $\text{SiO}_2$  thereby improving the coating microstructure. It can be seen from fig. 6.4(e) that after sintering, reduction in pore size was observed with an average pore size of 0.839  $\mu\text{m}$ . It demonstrates the effect of sintering on the grain boundary shift of  $\text{Al}_2\text{O}_3$  at 1073 K. During high-temperature sintering, ceramics went through grain boundary shift from high energy to the low energy state and decreased the porosity while increased the density of coating structure [25], [36]. Porosity and density of coating are inversely related with each other. Shrinkage of grain boundaries hindered the diffusion of oxygen to the composite surface and invigorated the interlocking of coating and specimen. Fig. 6.4(e) shows that the density of sintered coating was increased with 48 % reduction in porosity measured via ImageJ software. The reduction in porosity after sintering suggests that  $\text{SiO}_2$  was solidified and it also sealed up the cracks which were appeared during the shrinkage of coating.

Fig. 6.7 (c) depicts that as-deposited coating exhibited a surface profile with negative skewness. This indicates a surface with broad peaks and sharp valleys. Broad peaks and sharp valleys allowed heat waves to reside at maxima that triggered the grain boundary shift,  $\text{SiO}_2$  formation,



and interface development with enough heat absorption. After sintering, the surface roughness (Ra) increased from 4.55  $\mu\text{m}$  to 7.03  $\mu\text{m}$  (measured via SurfCharJ plugin of ImageJ). Surface profile indicated sharp peaks and broad valley profile that reflects surface structure as a good thermal barrier. The developed dense microstructure of  $\text{Al}_2\text{O}_3$  ceramic layer enhanced the thermal shock resistance of the coating.

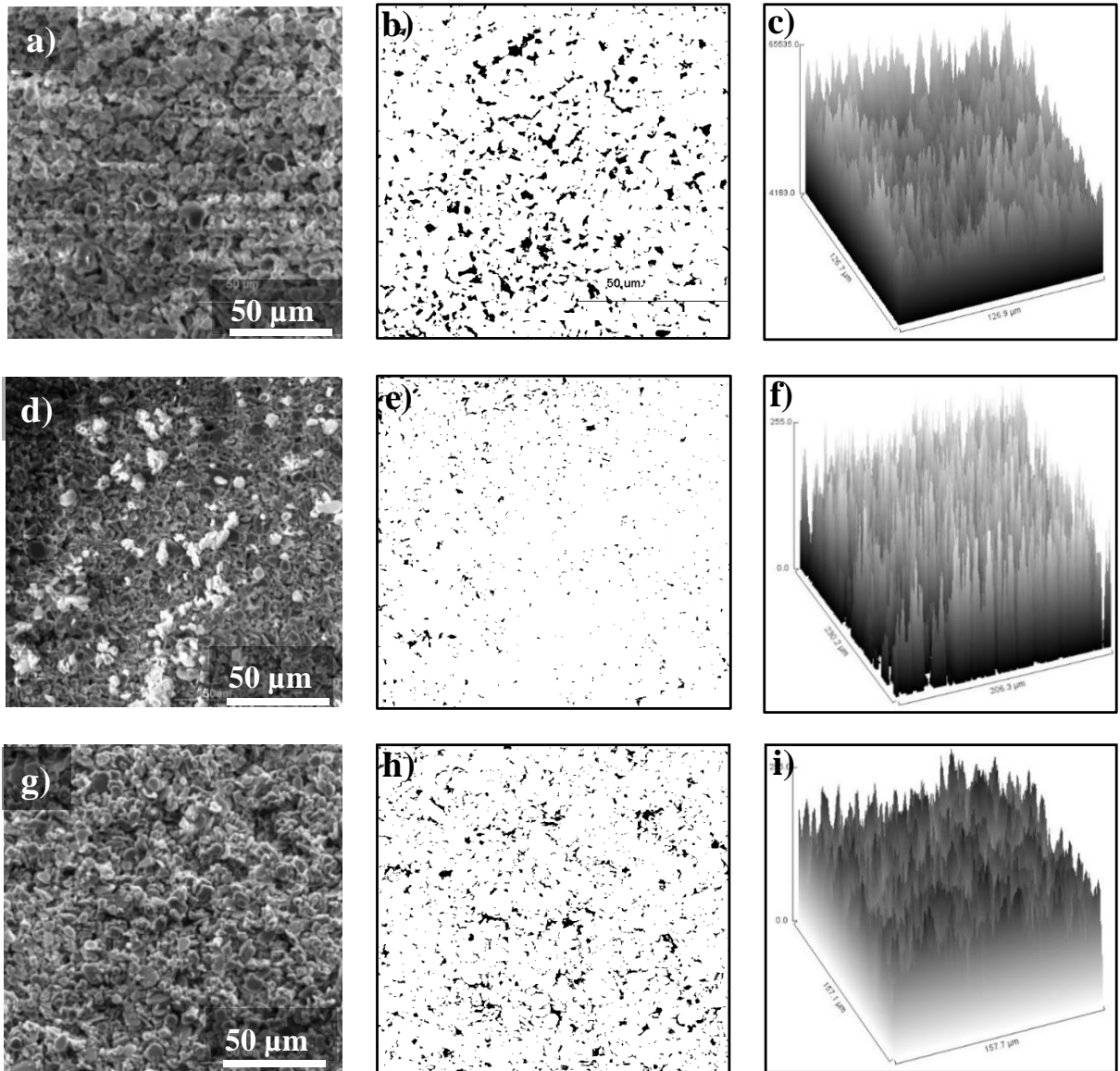


Figure 6.7: SEM image, binary image, and surface plot of the: (a-c) as-deposited coating; (d-f) coating after sintering at 1073 K; and (g-i) coating after ISOT testing of 3h, respectively.

Direct sintering of the coating at 1073 K after vacuum drying resulted in less mass loss as compared to stepwise sintering approach. It was noted that heating at 873 K resulted in rapid

degradation of carbon fibres and the corresponding weight loss was 29%. On the contrary, sintering at 1073 K resulted in lesser mass loss (i.e., 10.98%) which is attributed to the interface development. Isothermal oxidation test (ISOT) was conducted at 1273 K as a test for interfacial stability. No mass change was observed during the ISOT and the coating maintained its integrity with only a little change in coating thickness probably due to further densification of interface. Coating thickness varied from 259 to 258.3  $\mu\text{m}$  measured via ImageJ software. Exposure to oxidizing environment at constant temperature for several hours results in compressive stresses and microcracks. Fig. 6.4(h) shows that the dissipation of stresses results in surface microcracks. Although microcrack formation raised the surface porosity to 17%, destructive crack propagation was not observed. The  $\text{Al}_2\text{O}_3$  coating proved itself as a good barrier for application at 1273 K.

### **6.5. Thermal shock resistance of $\text{Al}_2\text{O}_3$ coating**

Fig. 6.5(a) is the camera image of as-deposited  $\text{Al}_2\text{O}_3$  coated C/SiC composite. Fig. 6.5(b) shows camera image of thermal shock tested specimens after 26 thermal cycles. Fig. 6.5(b) indicates that the surface roughness was increased after 5–26 thermal cycles. Heat-wave-impact not only altered the surface roughness but also increased the surface porosity.

Fig. 6.5(c). shows an obvious interlock interface after 26 thermal shock cycles which is beneficial to overcome thermal stresses originated because of mismatch of CTE between coating and C/SiC specimen. Compared with the morphology of before thermal shock testing cross section, some changes are observed. As at the interface, microcracks and pores were appeared near the interface and within the coating. Although no mass loss was observed which proves that the sintering at 1073 K integrated the interface with necessary microstructure. Surface porosity before and after DTS testing was measured 2.45% and 8% (measured via ImageJ software package) respectively.

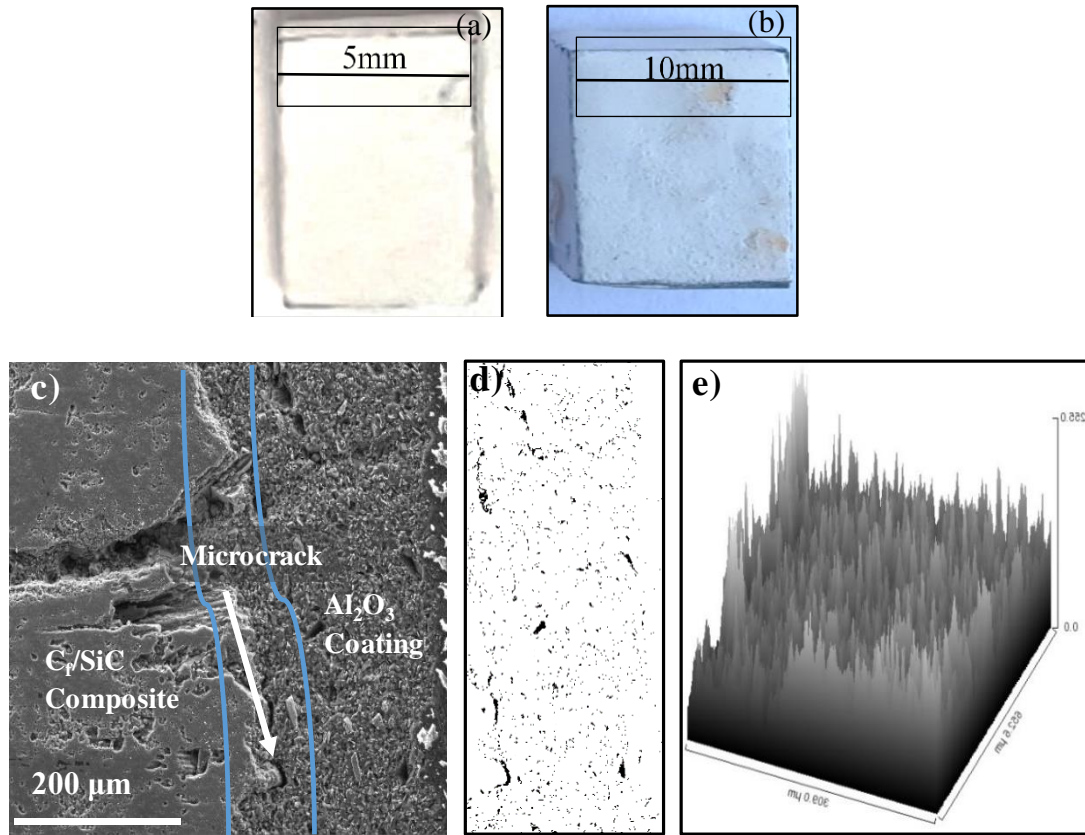


Fig 6.5. Camera image of coating & cross-sectional analysis: (a) as-deposited; (b) after 26 thermal shock cycles; (c) SEM of cross section after 26 thermal cycles; (d) binary image of interface; and (e) surface plot of interface, respectively.

It was noted that at high temperature, CTE mismatch resulted in tensile stresses throughout the coating structure i.e. at interface and surface. This effect became significant as the number of thermal cycles increased and promoted the production of cracks within the coating [7], [10], [16], [37], [38]. At 1273 K coefficient of thermal expansion (CTE) for  $\text{Al}_2\text{O}_3$  will become  $10.1 \times 10^{-6}/\text{K}$ , that reduces the thermal stresses due to volume expansion. The thermal conductivity of  $\text{Al}_2\text{O}_3$  decreases (from 20 W/ m·K at room temperature) as the temperature goes up (to 5 W/m·K at 1273 K); this leads to tensile stresses in the coating and originates the cracks [39]. Crack propagation and crack network control can only be possible with effective interface formation during sintering process.

Fig. 6.7 (a) shows the morphology developed after 5 thermal chock cycles. Fig. 6.7 (b) shows that the coating remained smooth with the development of a few micropores and microcracks. It should be in consideration that thermal cycling needs coating with moderate CTE so that it will neither peel off nor rupture. We addressed all these challenges during the development of  $\text{Al}_2\text{O}_3$  coating. Slurry based coatings are dense in nature because of high solid loading of suspension. Fig. 6.7 (c) shows the microstructure analysis via ImageJ of thermal shock tested specimen, it shows a porous surface with uniform distribution of pores and small microcracks.

Horizontal microcracks developed due to thermal stresses. Certain growth of microcracks is prerequisite to dissipate the thermal stresses evolved during thermal cycling. Crack formation over the surface facilitated to overcome the CTE mismatch. SurfChar J analysis showed a surface with positive skewness and kurtosis greater than 3, these features enhanced the heat rejection capability of the coating surface. Positive skewness indicates sharp peaks with broad valleys. Positive skewed surface increased the rate of heat rejection during thermal shock cycling.

During thermal cycling, coating maintained its integrity without any weight change. Although some depressions and ditches were observed on the surface, those were produced because of heat wave impact. The surface roughness was increased after thermal shock testing of specimens (i.e.  $R_a = 16 \mu\text{m}$ ).

It has been noted that grain size and thermal stresses are interrelated with each other; coating structured with the size range of  $1\text{--}5 \mu\text{m}$  have good ductility and high fracture toughness [14]. The coating retained its integrity without any observable crack formation (Fig. 6.7b). Densified microstructure with 15–20% porosity showed high resistance to crack growth and propagation. Meanwhile, the presence of pore spaces increases the compliance and counteracts the CTE mismatch. Wang et al. [18] developed a nanostructured YSZ coating having 9% porosity which peeled off only after 11 thermal cycles. Although, the coating thickness and thermal shock procedure also affect the thermal shock resistance. Our findings are in compliance with the coatings developed via expensive deposition techniques such as EB-CVD, APS, and PVD.

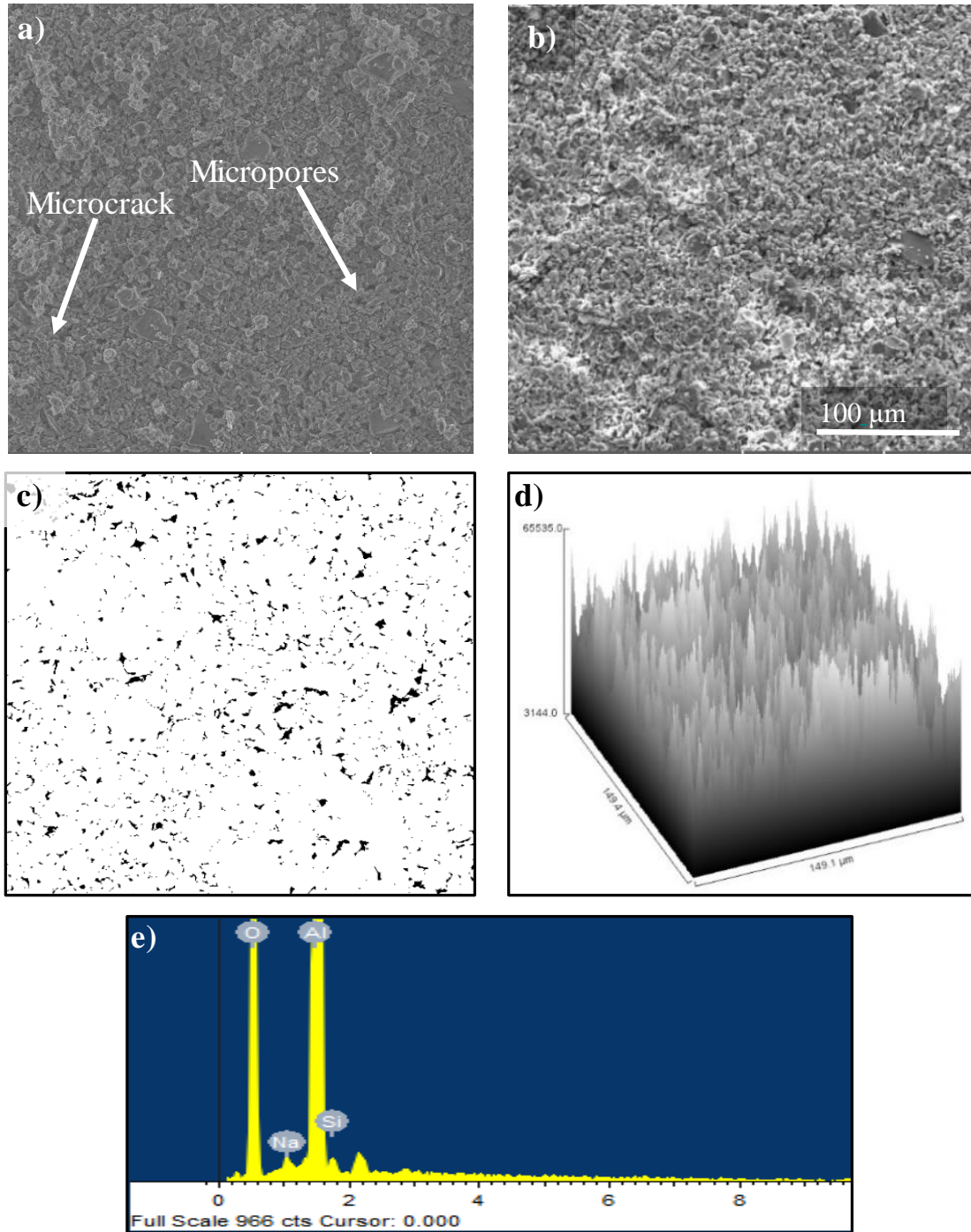


Figure 6.8: Microstructure analysis of thermal shock tested  $\text{Al}_2\text{O}_3$  coated C/SiC specimen via SEM and ImageJ analysis: (a) SEM after 5 thermal cycles; (b) SEM image; (c) binary image ( $50\ \mu\text{m}$ ); (d) surface plot; (e) EDS analysis; after 26 thermal shock cycles respectively.

## Summary

In this chapter we have discussed about the effort for the development of environmental and thermal barrier coatings (ETBCs) for the oxidation protection of C/SiC composites. Al<sub>2</sub>O<sub>3</sub> coating was deposited as ETBC on the surface of C/SiC composite after employing an easy and cost-effective slurry-dip coating route. The basic aim of this study is to investigate the thermal performance of a simple thermal protection system based on single material against the oxidative degradation of hot section components of gas turbine engine instead of a complex multilayered coating system. Our findings confirmed that a single coating system with 10-15% porosity can serve as an effective thermal barrier. We have performed isothermal oxidation testing and dynamic thermal shock testing to evaluate the thermal stability of coating against compressive and tensile stresses respectively. We have done with image analysis for calculating the porosity and surface roughness for developed and tested coating. Our findings are much better than the thermal protection system developed via costly route e.g. thermal spray technology. As per technology adaptation, maximum efficiency with minimum consumption of resources is still the matter of interest. Our work is in line to address the challenges regarding green energy production through gas turbine engine.

## References

- [1] I.A. Mahmood, W.W. Jameel, & Lubna, A. Khaleel, Improved oxidation resistance for thermal barrier ceramic coating protect, *Int. J. Res. Eng. Technol.* 1 (2013) 2321–8843. <http://oaji.net/articles/2014/489-1393410207.pdf> (accessed August 2, 2017).
- [2] J. Roy, S. Chandra, S. Das, S. Maitra, OXIDATION BEHAVIOUR OF SILICON CARBIDE - A REVIEW, *Rev. Adv. Mater. Sci.* 38 (2014) 29–39. [http://www-proxy.ipme.ru/e-journals/RAMS/no\\_13814/04\\_13814\\_roy.pdf](http://www-proxy.ipme.ru/e-journals/RAMS/no_13814/04_13814_roy.pdf) (accessed November 15, 2017).
- [3] C. Zhang, H. Wang, Y. Liu, S. Qiao, M. Li, D. Han, J. Zhang, Y. Guo, Thermal shock resistance of a 2D-C/SiC composite and its damage mechanisms, *Adv. Appl. Ceram.* 112 (2013) 499–504. doi:10.1179/1743676113Y.0000000120.
- [4] L. Cheng, Y. Xu, L. Zhang, X. Yin, Effect of carbon interlayer on oxidation behavior of C / SiC composites with a coating from room temperature to 1500 ° C, *High Temp.* 300 (2001) 219–225.
- [5] X.J. Lu, P. Xiao, Constrained sintering of YSZ/Al<sub>2</sub>O<sub>3</sub> composite coatings on metal substrates produced from eletrophoretic deposition, *J. Eur. Ceram. Soc.* 27 (2007) 2613–2621. doi:10.1016/j.jeurceramsoc.2006.09.016.
- [6] S.K. Khaja-abdul, SLURRY BASED COATINGS ON SILICON BASED CERAMICS, Cleveland State University, Cleveland OHIO, 2006.
- [7] Y. Xiang, W. Li, S. Wang, Z.-H. Chen, Preparation of UHTC based coatings for C–SiC composites by slurry and CVD, *Mater. Technol.* 27 (2012) 257–260. doi:10.1179/106678512X13333821993928.
- [8] I. Krenkel, Carbon fibre reinforced silicon carbide composites (C/SiC, C/C-SiC), *Handb. Ceram. Compos.* (2005) 117–148. [http://link.springer.com/chapter/10.1007/0-387-23986-3\\_6](http://link.springer.com/chapter/10.1007/0-387-23986-3_6).



- [9] J.F. Justin, A. Jankowiak, AL03-08 1 High-Temperature Materials Ultra High-Temperature Ceramics: Densification, Properties and Thermal Stability, (n.d.). <http://www.aerospacelab-journal.org/sites/www.aerospacelab-journal.org/files/AL3-08.pdf> (accessed June 30, 2017).
- [10] S. Honda, S. Hashimoto, H. Awaji, Thermal shock testing of ceramics, (n.d.). [http://www.atyc.org/2006aycect/abstract/p09c\\_honda.pdf](http://www.atyc.org/2006aycect/abstract/p09c_honda.pdf) (accessed August 14, 2017).
- [11] A.K. Krella, A.T. Sobczyk, A. Krupa, A. Jaworek, Thermal resistance of Al<sub>2</sub>O<sub>3</sub> coating produced by electrostatic spray deposition method, *Mech. Mater.* 98 (2016) 120–133. doi:10.1016/j.mechmat.2016.05.002.
- [12] J. Zhang, Q. Fu, P. Zhang, J. Qu, R. Yuan, H. Li, *Surface & Coatings Technology* Rapid heat treatment to improve the thermal shock resistance of ZrO<sub>2</sub> coating for SiC coated carbon / carbon composites, *Surf. Coat. Technol.* 285 (2016) 24–30. doi:10.1016/j.surfcoat.2015.11.027.
- [13] J. Ann, C.C. Berndt, *Surface Roughness of Plasma Sprayed Coatings: A Statistical Approach*, *DVS.* 302 (2014) 599–604.
- [14] F. Blas, F. Ansart, P. Lours, J. Bonino, S. Duluard, V. Vidal, L. Pin, G. Pujol, L. Bonin, Processing thermal barrier coatings via sol-gel route: Crack network control and durability, *Surf. Coat. Technol.* (2017). doi:10.1016/j.surfcoat.2017.11.008.
- [15] B. Baufeld, O. van der Biest, H.-J. Raetzer-Scheibe, Thermal and Mechanical Properties of Zirconia Coatings Produced By Electrophoretic Deposition, *Adv. Ceram. Coatings Interfaces* 28 (2008) 3–10.



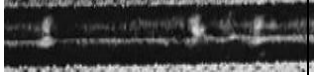
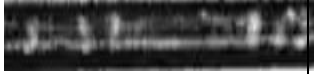

# Chapter 7

## Microchannel Heat Transfer

### 7.1. Flow Regimes at Saturation Temperature 40°C

The development of flow regimes during the condensation of R134a was also studied at saturation temperature 40°C. The experimental results at the saturation temperature of 40°C are presented in Table 7.1.

Table 7.1: Experimental results for flow visualization at 40°C saturation temperature

Mass Flux G (Kg/m <sup>2</sup> s)	T-Sat (°C)	Quality x	Coolant flow rate (ml/min)	Martini Parameter Xtt	Superficial Vapor Velocity Jg*	High Speed Camera flow visualization
75	40	0.42	14	1.506	0.307	
100	40	0.53	14	0.80	0.6199	
150	40	0.70	14	0.299	1.515	

#### 7.1.1. Barnea Two-Phase Flow Regime

The results acquired are compared with the flow regime map proposed by Barnea et al. Barnea et al concluded that at low flow rates in small channels, there will be a transition from annular to slug flow. Surface tension forces were the governing forces for transition of annular flow to slug flow in small diameter tubes at low flow rates of liquid and gas. Their study was focused on air-water mixture flowing inside small tubes of hydraulic diameters 4 to 12 mm. Flow visualization indicated that the flow was in the transition region. The results of the present study were compared with the flow regime map of Barnea et al between mass flux and quality. A good comparison study was seen by our data points onto the flow map of Barnea et al. at the saturation temperature of 40°C against mass fluxes of 75kg/m<sup>2</sup>s, 100kg/m<sup>2</sup>s, 150kg/m<sup>2</sup>s. All data points showed good satisfaction with the flow map of Barnea et al. Intermittent flow

regimes were observed at low mass flux of  $75\text{kg/m}^2\text{s}$ , slug flow regime at  $100\text{kg/m}^2\text{s}$  and at mass flux of  $150\text{kg/m}^2\text{s}$ , there was a transition behavior seen from annular to intermittent as shown in Figure 3.

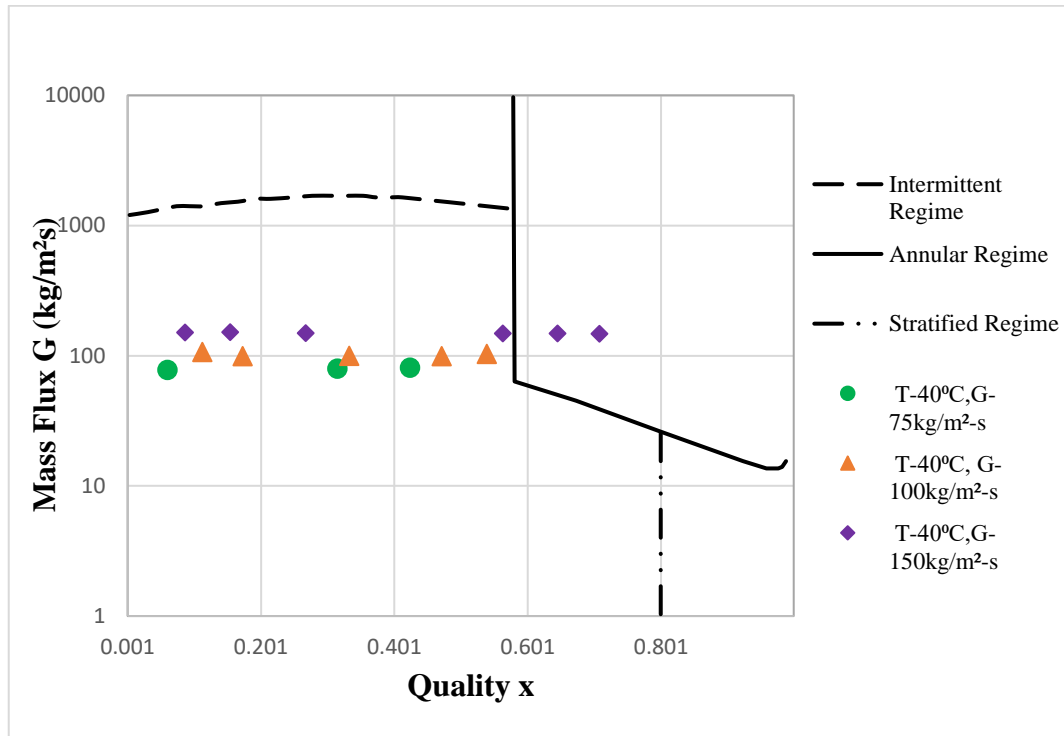


Figure 7.1: Comparison to Barnea et al. flow map for R134a at  $40^\circ\text{C}$  in 0.84mm channel

### 7.1.2. Breber Two-Phase Flow Regime

A flow map given by Breber et al. for condensation of refrigerant inside microchannels using widely data of dimensionless gas velocity against Martinelli Parameter and the data points were plotted on the flow map of Breber et al. and compared with results at different mass fluxes and found that at lower mass fluxes of  $75\text{kg/m}^2\text{s}$  and  $100\text{kg/m}^2\text{s}$ , the flow regime lies within the intermittent region but with the increase of mass flux values at given temperatures of  $40^\circ\text{C}$ , the transition behavior seen from annular or mist annular to intermittent (slug, plug) flow region such as in case of  $150\text{kg/m}^2\text{s}$  [13]. The transition from annular and mist annular to intermittent or wavy flow delayed due to the increased reduce pressure at lower qualities and these transitions exist at higher qualities depends upon the given diameter of channel. With the

increase in vapor density, the liquid-vapor density ratio reduces by increasing pressure. The maximum portion of quality ranges lies within those regions where gravitation forces are more significant than vapor tension force. By comparing the experimental data with the Breber et al. flow map shows better agreement.

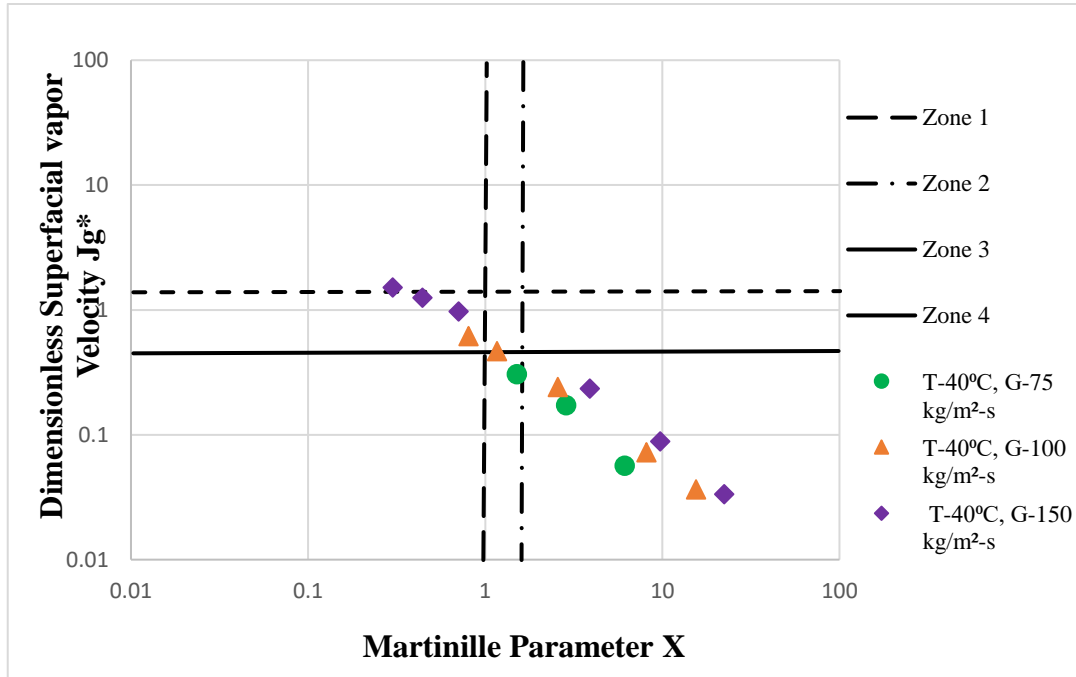


Figure 7.2: Comparison to Breber et al. flow map for R134a at 40°C in 0.84mm channel

## 7.2. Flow Regimes at Saturation Temperature 55°C

The experiments were conducted at low mass fluxes of refrigerant and low volumetric flow rate of coolant at the saturation temperature of 55°C. The experimental results at the saturation temperature of 55°C are presented in Table 3. It can be seen from Table 7.2 that the transformation of superheated vapor into liquid was reduced as the mass flux was increasing



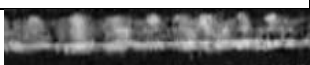
while keeping the coolant flow rate at 10 ml/min. At low mass flux, mixed vapor streams were observed.

### 7.2.1. Barnea Two-Phase Flow Regime

Figure 7.4 clearly depicted that the increasing coolant flow rate at a mass flux of 150 Kg/m<sup>2</sup>s resulted in the transition of flow from annular to intermittent flow region. While at low mass fluxes, the flow observed and calculated is within the intermittent region. As the coolant flow rate increased, it decreased the quality of vapors and indicated that flow transition from annular to intermittent flow at higher mass fluxes. At low velocities of fluid, laminar flow dominated because turbulence was generated against the high velocity of fluids during flow.

It should be noticed that in the present study microchannels are of hydraulic diameter  $D_H$  0.84mm, while Barnea studied the flow regimes in the channel with hydraulic diameter  $D_H$  4-12mm. With the reduction of channel size, the surface tension forces are dominating at the gravitational forces. It can say that flow regimes are not only affected by channel size. Mass fluxes and coolant flow rate are also vital entities in the development of flow regimes. The development of flow regimes at low mass fluxes will also be under the gravity effects.

Table 7.2: Experimental results for flow visualization at 55°C saturation temperature

Mass Flux G (Kg/m <sup>2</sup> s)	Coolant flow rate (ml/min)	T-Sat (°C)	Qua lity x	Martinelli Parameter X	Superficial Vapor Velocity Jg*	High Speed Camera flow visualization
75	10	55	0.27	4.5	0.09	
100	10	55	0.5	1.22	0.38	
150	10	55	0.64	0.55	0.64	

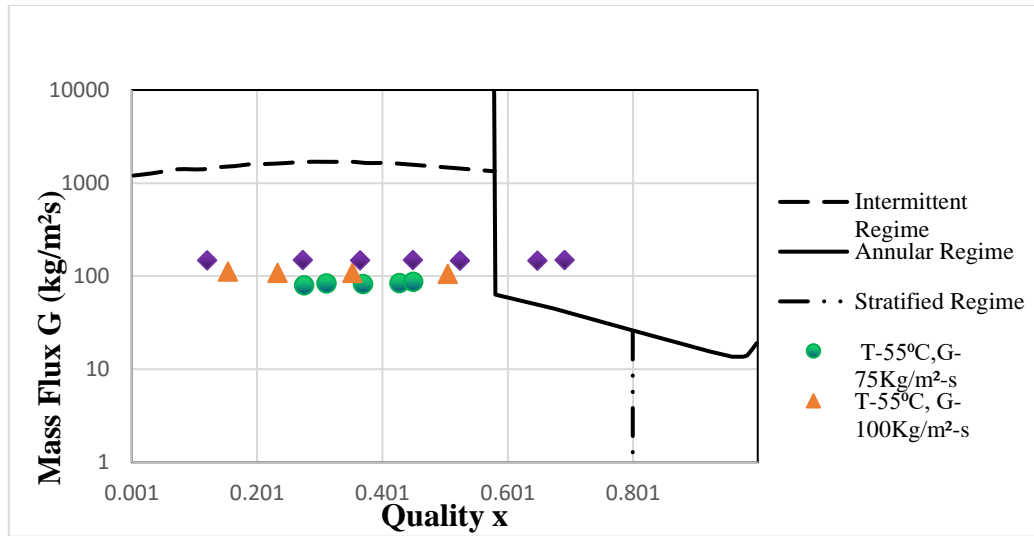


Figure 7.3: Comparison to Barnea et al. flow map for R134a at 55°C

### 7.2.2. Breber Two-Phase Flow Regime

Breber et al, 1980 proposed the first experimentally proved condensation flow regime map that was fully satisfied with the theoretically derived flow regime map of Taital and Dukler for condensation heat transfer. They stated from their study that dimensionless flow regime parameters, i.e. Superficial vapor velocity and Martinelli parameter, are good for describing adiabatic two-phase flow. So, the present study was compared with the Breber et al. flow regime map. It was resolute that at a low mass flux of about 75 Kg/m<sup>2</sup>-s the two-phase flow was in the transition region from annular to intermittent. As the flow rate increased, flow regimes shifted to the transition zone between annular to the intermittent region. At higher mass flux of about 150 Kg/m<sup>2</sup>s, it was also observed that there was a transition in flow regimes from annular flow to intermittent flow. It means that when increasing the coolant flow rate, the dominance of shear forces over gravitational forces will result in the development of annular regimes. The illustrations are given in Figure 5.

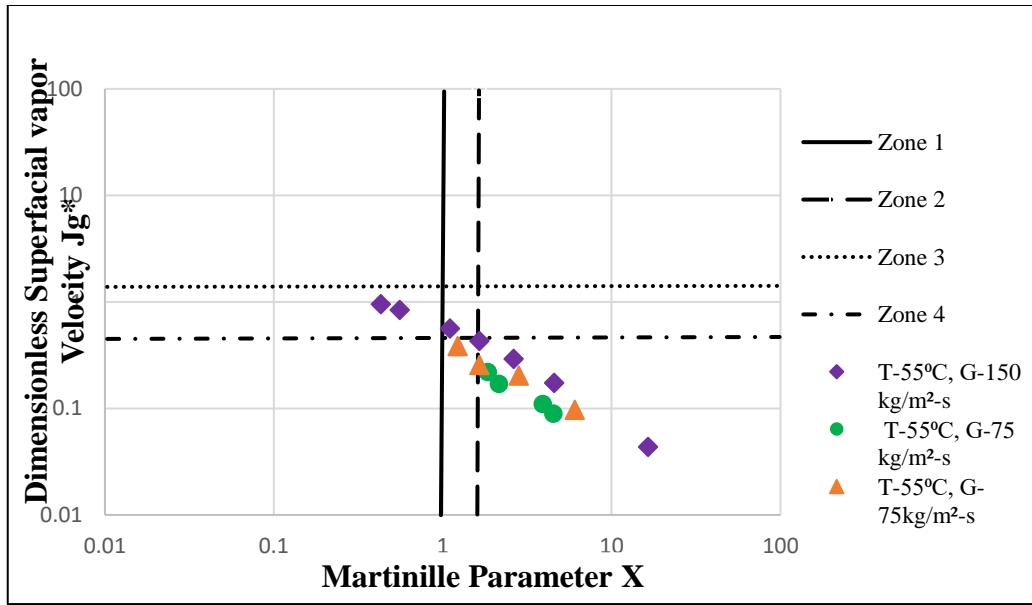


Figure 7.4: Comparison to Breber et al. flow map for R134a at 55°C in 0.84mm channel

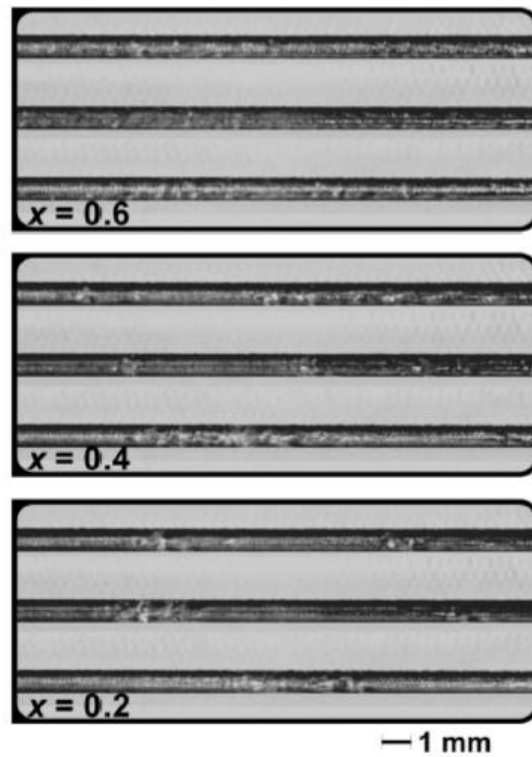


Figure 7.5: Comparison of visualization data  $G=100 \text{ Kg/m}^{-2} \text{ s}^{-1}$ ,  $T_{\text{sat}} = 40^\circ\text{C}$ , comparison of three different qualities

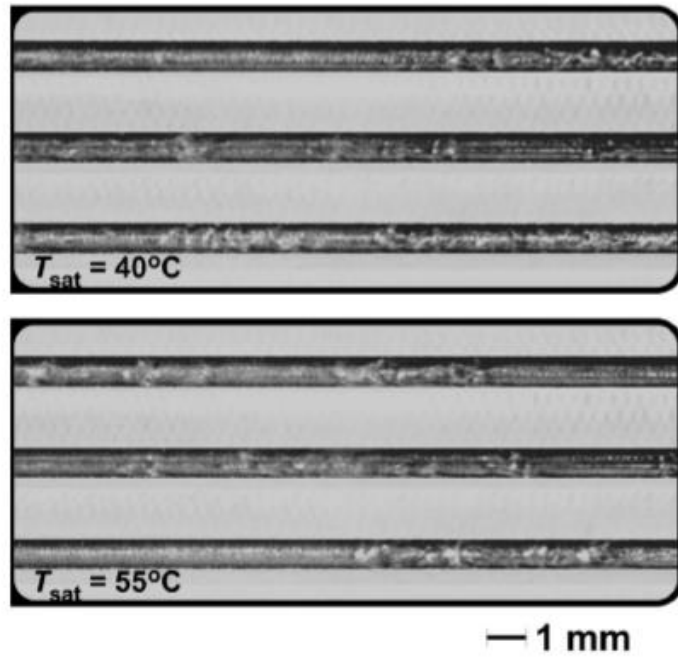


Figure 7.6: Comparison of visualization data  $G=100 \text{ Kg/m}^{-2} \text{ s}^{-1}$ ,  $x=0.2$  at two saturation temperatures, comparison of three different qualities

## Summary

In the present study, a test bed was developed capable of high-speed visualization and measurement of two-phase fluid refrigerant flow through microchannels at low mass fluxes. The test bed was used to collect data ( $75 < G < 150 \text{ kg m}^{-2} \text{ s}^{-1}$ ,  $0.05 < x < 0.75$ ,  $D_h = 0.84 \text{ mm}$ ) at two different saturation temperatures ( $T_{\text{sat}} = 40, 55^\circ\text{C}$ ) to assess the predicative capability of a variety of flow maps when applied to fluid flow in microchannels at such low mass fluxes. While the visualization was done under locally adiabatic conditions, the flow was condensed from a superheated state in a continuous microchannel rather than boiled or introduced as two-phase mixture, providing a better representation of what would happen in an actual condenser. The flow regimes observed for the range of conditions was primarily annular or wavy/annular flow. Transition to intermittent or wavy flow was not observed. Flow results were compared to flow maps presented by a variety of authors for macro and mini/microchannels, with none of the maps predicting the data well. Of the maps considered, the Taitel and Dukler [12] map surprisingly performed the best, correctly predicting 98% of the data to be annular and the rest intermittent. The Nema et al. [17] map was a distant second, predicting 46% as annular, with the remainder intermittent. Even though developed from data for small channels, the Nema et al. [17] map did not include data for channels below 1 mm or such low mass fluxes. Also of interest is that none of the maps agreed particularly well with one another. Potential reasons for discrepancy between the data and predictions include the use of non-circular tubes (stronger surface tension effects), operation at conditions outside the range, particularly the low mass flow for which most maps were developed for, as well as the potential for non-equilibrium effects at low mass flux and low thermodynamic quality.



## References

- [1] J. El Hajal, J. . Thome, and A. Cavallini, “Condensation in horizontal tubes, part 1: two-phase flow pattern map,” *Int. J. Heat Mass Transf.*, vol. 46, no. 18, pp. 3349–3363, Aug. 2003.

# Chapter 8

## 8.1. Conclusion

After thermal analysis of Monel 400 superalloy following implication were concluded:

- A simple ETBC system via Alumina has successfully deposited on Monel 400 Superalloy via slurry dip coating route instead of the complex multilayered system.
- Weight gain reduction was observed for the coated coupon as compared to uncoated coupon after oxidation at 1000°C.
- XRD analysis confirmed the protective spinel formation  $\text{Al}_2\text{SiO}_5$ ,  $\text{Ni}_2\text{SiO}_4$ ,  $\text{CuAl}_2\text{O}_4$  at the interface
- SEM analysis shows homogenous, crack-free, less porous microstructure for developed coating.
- Study concluded that slurry deposition as a favorable technique for employing alumina as protective shield material for high-temperature applications

The present study was also conducted to investigate the thermal performance of slurry deposited  $\text{Al}_2\text{O}_3$  on C/SiC composite for high-temperature applications. At least six  $\text{Al}_2\text{O}_3$  coated C/SiC coupons were prepared in this study. Every experiment was conducted 3 times to get maximum accurate results. The thermal resistance of the coating was studied via ISOT and DTS testing. Image analysis was done to understand the surface structure that best suit as an ETBCs. It has been concluded that particle size, roughness, and porosity are interrelated with each other. The developed coating exhibits the asymmetrical and peaked profile as indicated from the surface plot and plot profiles. The skewness and kurtosis results are above than zero and three respectively in most cases. Positive values indicated that surface was structured with sharp peaks and broad valleys.

Following implications were deduced from the study:

- Well adhered, 10-15% porous, smooth thermal resistant  $\text{Al}_2\text{O}_3$  shield was developed on C/SiC composite via slurry-dip coating process

- The well-boned interface was developed after sintering at 800°C under an air atmosphere with an 10 % porosity and 260 μm coating thickness.
- Al<sub>2</sub>O<sub>3</sub> has been proved as an excellent material for the protection against high-temperature oxidation for jet engine and land-based gas turbines. It has good thermal resistance against thermal shocks and allowed only weight loss of about 0.68 wt. % after 26 thermal cycles.
- Coating surface with 0.5-3 μm R<sub>a</sub> surface roughness with positive skewness and greater than 3 kurtosis will act as a good ETBC as compared to highly porous with 2-10 μm surface roughness thermal sprayed coatings and EPD coatings.

In the present study of microchannel heat transfer, that was conducted to measure the heat transfer via microchannels at low mass fluxed. The objective of the study was to develop flow regime map related to microchannel two-phase condensation. In this study, a test bed was developed capable of high-speed visualization and measurement of two-phase fluid refrigerant flow through microchannels at low mass fluxes. The test bed was used to collect data ( $75 < G < 150 \text{ kg m}^{-2}\text{s}^{-1}$ ,  $0.05 < X < 0.75$ ,  $D_h = 0.84 \text{ mm}$ ) at two different saturation temperatures ( $T_{\text{sat}} = 40, 55^\circ\text{C}$ ) to assess the predicative capability of a variety of flow maps when applied to fluid flow in microchannels at such low mass fluxes. While the visualization was done under locally adiabatic conditions, the flow was condensed from a superheated state in a continuous microchannel rather than boiled or introduced as two-phase mixture, providing a better representation of what would happen in an actual condenser. The flow regimes observed for the range of conditions was primarily annular or wavy/annular flow.

Transition to intermittent or wavy flow was not observed. Flow results were compared to flow maps presented by a variety of authors for macro and mini/microchannels, with none of the maps predicting the data well. Of the maps considered, the Taitel and Dukler [12] map surprisingly performed the best, correctly predicting 98% of the data to be annular and the rest intermittent. The Nema et al. [17] map was a distant second, predicting 46% as annular, with the remainder intermittent. Even though developed from data for small channels, the Nema et al. [17] map did not include data for channels below 1 mm or such

low mass fluxes. Also of interest is that none of the maps agreed particularly well with one another.

Potential reasons for discrepancy between the data and predictions include the use of non-circular tubes (stronger surface tension effects), operation at conditions outside the range, particularly the low mass flow for which most maps were developed for, as well as the potential for non-equilibrium effects at low mass flux and low thermodynamic quality. The results suggest that further work to understand flow transitions at low mass flux in small, non-circular channels are required. Understanding these transitions is critical to developing mechanistic heat transfer and pressure drop models for design of microchannel based condensers.

## **8.2. Future Recommendations**

- Present study was conducted to investigate the thermal performance of single coating system for this, alumina was chosen candidate because of its high melting point & good thermomechanical stability.
- Other ceramics material can be tested with alumina to improve the thermal performance at High-Temperatures such as 1500-1700°C.
- Heat transfer study should be conducted to find out the thermal gradient with proposed coating system.
- Finite elemental analysis should be performed to study the combined effect of ETBCs and microchannel cooling system

- Thermal fatigue life analysis should be performed to evaluate the coating sustainability in real environment
  
- A testing station for thermal cycling that reflects a real environment should be established to get more confident results.

## Annexure I

### **Oxidation protection study for Monel 400 Superalloy via slurry deposition of Al<sub>2</sub>O<sub>3</sub> coating for gas turbine engine application**

Authors: Maria Sattar<sup>1</sup>, Mariah Batool<sup>1</sup>, Zuhair S. Khan<sup>1\*</sup>

<sup>1</sup>U.S. Pakistan Center for advanced studies in Energy (USPCAS-E), National University of Sciences and Technology (NUST), Islamabad, 44000, Pakistan

\*[zskhan@ces.nust.edu.pk](mailto:zskhan@ces.nust.edu.pk) Tel: +9251-90855276

#### **Abstract**

In this study, an oxidation protective shield of Al<sub>2</sub>O<sub>3</sub> was prepared on Monel 400 alloy via a slurry-dip coating process instead of a more expensive thermal spray process. On exposure to 600°C, 800°C and 1000°C, slow-growing spinel formation was observed at the surface. Analytical techniques such as XRD, SEM and EDS analysis were employed for microstructure and microchemistry data before and after isothermal testing. Sintering resulted in uniform distribution of nano sized as well as micro sized pores. The coating retained its integrity upon exposure to service temperature; however, after testing at 1000°C, some cracks were observed in the coating. Reduction in weight gain was observed for coated substrate. The pore fraction and morphology of pores have considerable effect on oxidation kinetics of Al<sub>2</sub>O<sub>3</sub> coated Monel 400 alloy. The Al<sub>2</sub>O<sub>3</sub> coating shows good oxidation resistance.

Keywords: Ceramic coating; dip coating; high-temperature oxidation; oxidation kinetics; Monel 400 alloy; oxidation rate; porosity; slurry deposition; spinel oxides; thermal conductivity; surface roughness; selective oxidation

#### **Introduction**

Developments in energy generation technologies are stepping up to reduce fuel consumption and mitigate environmental impacts. Natural resources such as coal, natural gas and oil are at the forefront of energy production via thermal technology. The gas turbine engine is the mainstay of thermal power plants for continuous electricity generation [1]. Low efficiencies, high fuel consumption, and polluting emissions are major challenges that need to be addressed for a sustainable gas turbine engine operation. Higher efficiency needs to rise the inlet gas temperature higher than the melting point of base material, e.g., Ni superalloy. The increase in inlet gas temperature threatens the durability of base material (Soechting, 1999, Eriksson, 2011). The base material of gas turbines operating at temperature  $\geq 1000^{\circ}\text{C}$  needs to be oxidation and corrosion resistant [4]. In the consequence of increase in inlet conditions, emphasis in gas turbine materials development has shifted to the advances of cooling techniques. Environmental and thermal barrier coatings (ETBCs) and air-cooling techniques are employed together to overcome the catastrophic oxidation of the base material [5].

Monel 400 superalloy, a class of Ni-base superalloys, is a conventional material with an operating range of  $600\text{--}900^{\circ}\text{C}$  for gas turbine engines and widely used for steam generators, boiler components, nuclear reactors and fossil fuels thermal power plants [6], [7]. Monel 400 alloy exhibits  $0.04\ \mu\text{m}$  penetration depth for the diffusion of deleterious oxides. This feature enlightens the anticorrosion capability of Monel 400 alloy above than  $1000^{\circ}\text{C}$  [8]. However, poor oxidation resistance and low mechanical strength do not support it in high temperature environment, however, recent studies identified it as a catalyst for  $\text{NO}_x$  reduction [6]. In this regard, environmental and thermal barrier coating is needed which can protect it from the harmful impacts of high-temperature oxidation when exposed to air. Hence, the provision of ETBCs can allow the working temperature to rise above the melting point of Monel 400 superalloy [1].

Regarding thermal barrier coatings, thermal conductivity becomes a challenge. Thermal conductivity of coating material has significant impact on the protective spinel growth at the surface for durable interface. It stimulates the sintering process and establishes an adhered interface [4]. Although, thermal conductivity of coating depends on the surface parameters i.e. porosity, pore size distribution and surface roughness [9].

Thermal barrier coatings are ceramic coatings, which are exhibited low coefficient of thermal expansion, low thermal conductivities, chemical inertness and phase stability at high temperature. A ceramic coating with a thickness of 120–400  $\mu\text{m}$  can reduce the substrate temperature by 100–300  $^{\circ}\text{C}$  [1]. Within the ceramic family,  $\text{TiO}_2$ ,  $\text{ZrO}_2$ ,  $\text{CeO}_2$ ,  $\text{NiCrAl}$ ,  $\text{NiAl}$  and  $\text{Al}/\text{Al}_2\text{O}_3$  are promising candidates for the application of thermal barrier coatings to Ni-base superalloys (Whittenberger, 1974; Schilke, 2004; Baufeld, van der Biest and Raetzer-Scheibe, 2008; Hardwicke and Lau, 2013; Mahmood et al., 2013; Ito et al., 2014; Wang et al., 2014; Oksa, 2015; Roy et al., 2016; Zhang et al., 2017). Among these all,  $\text{Al}_2\text{O}_3$  offers high thermal conductivity and melting temperature, high hardness and good mechanical stability at high temperatures [20], [21]. The higher thermal conductivity at room temperature is a distinguish feature that termed  $\text{Al}_2\text{O}_3$  as a proven ETBC material for high temperature oxidative environment i.e. 1000 $^{\circ}\text{C}$ . Though, pure  $\text{Al}_2\text{O}_3$  coating exhibits porous microstructure and low fracture toughness that imposes major concerns with coating deposition technology. Various costly deposition techniques such as thermal spraying, chemical vapor deposition (CVD), electron beam physical vapour deposition (EB-PVD) and electrophoretic deposition (EPD) have been employed in industries for developing a durable coating for turbine components, such as, blades and vanes [22]. Compared to other deposition techniques, slurry-dip coating is preferable due to low equipment cost, process simplicity, controlled microstructure, high deposition efficiency and high drying rate [23]. Although, slurry-dip coating process has been demonstrated for various process parameters but obtained layer morphology has not been reported.

To address abovementioned challenges, the aim of this study to investigate the oxidation kinetics related to morphology of  $\text{Al}_2\text{O}_3$  coating, deposited by slurry dip coating process on Monel 400 alloy. This method allows to achieve thick coating with nano/micropores even at low surface roughness. Sintering at 600 $^{\circ}\text{C}$  reflects selective oxidation approach for establishing a nano/microporous coating surface. This study addresses how porosity and thermal conductivity of slurry deposited  $\text{Al}_2\text{O}_3$  base ETBC effect the oxidation kinetic of Monel 400 alloy. Such investigations regarding slurry deposition method have never been reported.



## 2. Material and methods

### 2.1 Substrate and coating material

The substrate material used in this study was Monel 400 alloy. Its chemical composition is given in Table 1, and physical and thermal properties are listed in Table 2 (S. Corporation, 2005). The substrate was cylindrically shaped with dimensions of 1(length) cm  $\times$  1.3(diameter) cm. The slurry comprised of Al<sub>2</sub>O<sub>3</sub> powder, polyethyleneimine (PEI) and distilled water. The average Al<sub>2</sub>O<sub>3</sub> particle size was measured to be  $\sim$ 2.54  $\mu$ m as shown in Figure 1. The Monel 400 alloy substrate surface was prepared prior to deposition of coating. Surface was sand blasted, acetone washed, dried and sonicated to remove impurities from the substrate surface. Surface roughness parameter Ra was measured as 0.42  $\mu$ m with the help of a surface roughness tester (Model No. NDT 110, Hong Kong).

**Table 3. Chemical composition of Monel 400 alloy**

Element	%
Ni	63
Mn	$\leq 2$
Fe	$\leq 2.5$
Cu	28–34
Si	0.5
C	0.3
S	0.025

**Table 4. Physical and mechanical properties of Monel 400 alloy at room temperature**

Property	Value
Density (g/cm <sup>3</sup> )	8.8
Tensile strength (N/mm <sup>2</sup> )	579–827
Thermal conductivity at 20°C-1000°C (W/m· °C)	22–48.8

Specific heat at 20°C-1000°C (J/Kg °C)	427–470
Co-efficient of linear expansion between 20°C–1000°C ( $10^{-6}/^{\circ}\text{C}$ )	14–18.1
Max. operating temperature ( $^{\circ}\text{C}$ )	1300–1350

---

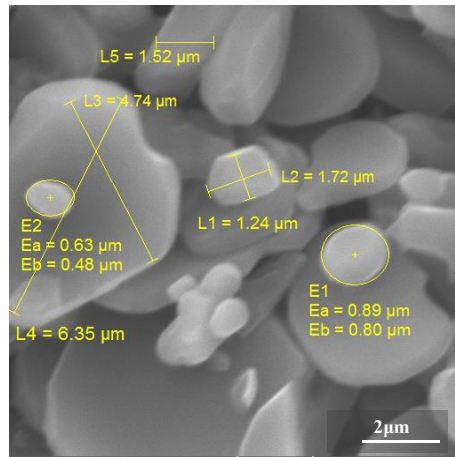


Figure 7. SEM image of  $\text{Al}_2\text{O}_3$  particles

## 2.2 Deposition of coating

$\text{Al}_2\text{O}_3$  slurry was prepared after manual grinding of  $\text{Al}_2\text{O}_3$  powder using a mortar and pestle. This powder was added into 80°C PEI solution and magnetically stirred for 6 hours. The  $\text{Al}_2\text{O}_3$  coating was deposited at the surface with a dip coating process. The dip coater was programmed manually, and the speed of dipping was set to 25 mm/min. A smooth and well-adhered coating was prepared after three consecutive dip coats. The coated substrate was dried at 25°C for 12 h. Afterwards, the coated substrates were vacuum dried at 250°C for 2 h; to increase the mechanical interlock of coating with the substrate. Subsequently, the coating was sintered at 600°C for its consolidation.

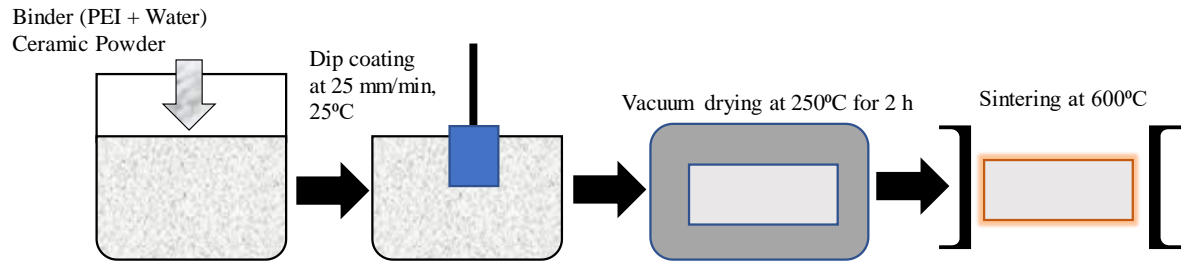


Figure 8. Slurry deposition-based method for preparing Al<sub>2</sub>O<sub>3</sub> coated Monel 400 specimen

### 2.3 Characterization techniques

Microstructure and microchemistry of the coated sample before and after oxidation was analyzed by X-ray diffraction, XRD (D8, Advance Bruker X-ray diffractometer) with Cu K $\alpha$  radiation generated at 40 KV and 30 mA. The scanning rate was 2.57 step/sec with a step size of 0.02° over a range of 20° to 80°. Phase identification was carried out by XRD phase identification software MDI Jade 6.5. The coating morphology and elemental composition were characterized with the help of scanning electron microscopy/energy-dispersive X-ray spectroscopy, SEM/EDS (Vega3 TEScan scanning electron microscope equipped with Oxford EDS). ImageJ software was used to calculate the porosity and surface roughness of the coating over the course of the study.

### 2.4 Isothermal oxidation testing

Air-sintering of coating was done at 600°C for 3 h in a box furnace. Coating durability and performance in the real environment was evaluated after subjecting the Al<sub>2</sub>O<sub>3</sub> coated Monel 400 superalloy to temperatures of 800°C and 1000°C for an exposure time of 6 h in a box furnace, respectively. Weight change was measured using an analytical balance with a sensitivity of 0.1 mg. XRD and SEM/EDS analyses were performed to analyse the surface chemistry and microstructure of oxidized substrates.

## 3. Results and discussion

### 3.1 Isothermal oxidation testing

Weight gain curve for uncoated and coated Monel 400 alloy was shown in Figure 3. A progressive weight gain curve was obtained for the oxidation of uncoated Monel 400 alloy from

250-1000°C. Weight gain curve at 600°C indicated the same trend for uncoated and coated substrates. Afterwards, for coated substrate, weight gain was not observed beyond 800°C, indicating that Al<sub>2</sub>O<sub>3</sub> retarded the oxidation process (Figure 3). It infers from the plot that weight gain curve followed parabolic law for coated substrates (Figure 3).

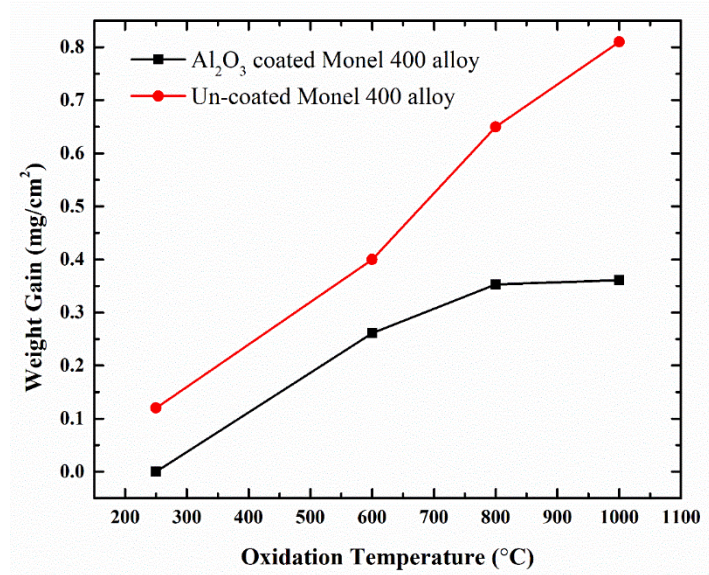


Figure 9. Weight gain curve for uncoated and Al<sub>2</sub>O<sub>3</sub> coated Monel 400 alloy substrate with a surface area of 5.625 cm<sup>2</sup>. Duration of each cycle was 6 h.

Table 3 shows the oxidation kinetics at service temperatures 600°C, 800°C, 1000°C respectively. It indicates that during sintering 600°C oxidation rate was high. While during ISOT, surface oxidation occurred but at lower rate and became negligible at 1000°C. From this, it infers that thermodynamically stable oxide scale and spinel i.e. NiO, Al<sub>2</sub>O<sub>3</sub>, CuAlO<sub>2</sub>, Fe<sub>3</sub>O<sub>4</sub>, CuFe<sub>2</sub>O<sub>4</sub>, protected the deteriorated oxidation of inner metal. The oxidation kinetics for coated substrates was slowed down because of low diffusivity of hot gases to the coating surface (Table 3).

Table 5. Oxidation rate of slurry deposited Al<sub>2</sub>O<sub>3</sub> coated Monel 400 superalloy

Oxidation temperature (°C)	Oxidation rate $(\Delta m/A)^2/t$ [mg <sup>2</sup> /cm <sup>4</sup> ·s <sup>-1</sup> ]
600	0.24 e <sup>-10</sup>
800	0.115 e <sup>-10</sup>
1000	0.116 e <sup>-10</sup>

### 3.2 XRD analysis

Figure 4 shows the XRD analysis for the uncoated and coated Monel 400 alloy before and after oxidation.  $\alpha$ -  $\text{Al}_2\text{O}_3$  (104) used in this study exhibited hexagonal structure and the Monel 400 alloy single crystal (111) exhibited a cubical structure. For uncoated oxidized substrates, low-intensity peaks with minute concentration of  $\text{Cu}_2\text{O}$  and  $\text{FeO}$  were observed. Although stable oxide scale  $\text{NiO}$  and  $\text{CuO}$  was not formed at the surface (Figure 4c). For the coated substrates, XRD pattern indicates the formation of oxide scale  $\text{NiO}$ ,  $\text{CuO}$  along with the protective spinel oxides  $\text{CuAlO}_2$ ,  $\text{Fe}_3\text{O}_4$ ,  $\text{CuFe}_2\text{O}_4$  and  $\text{NiMn}_2\text{O}_4$ . The miller indexes are (200), (002), (012), (311), (311) and (311) with the corresponding  $2\theta$  degree values of, 43.38, 35.382, 37.853, 35.41, 35.438 and 35.40 respectively (Figure 4d). However,  $\text{Cu}_2\text{O}$  formation belonged to initial oxidation of  $\text{Cu}$ , was not observed in upper oxide scale for coated substrate.

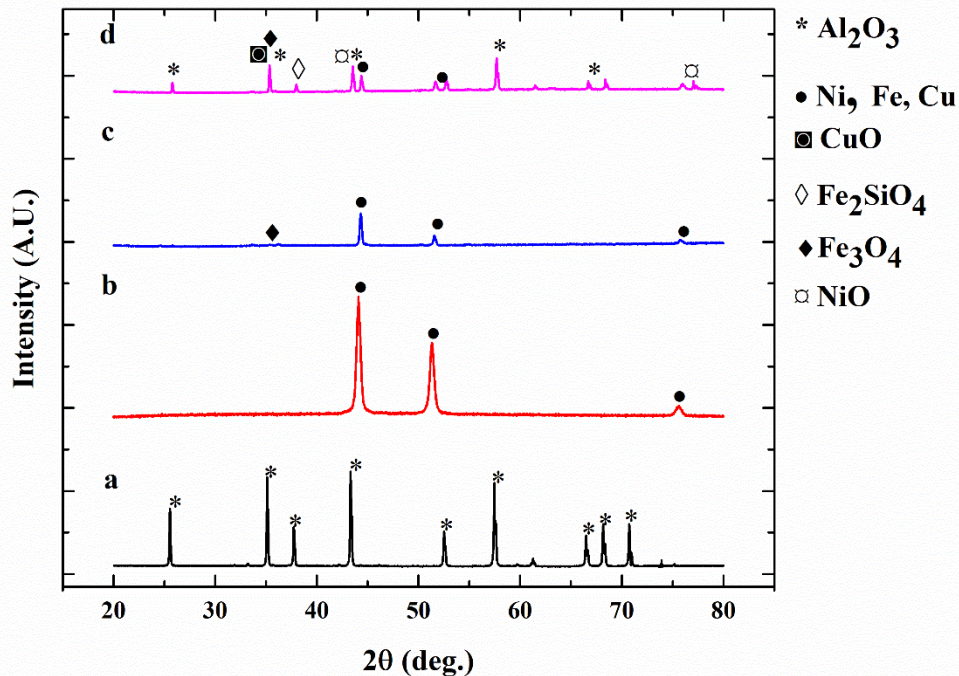


Figure 10. XRD analysis of a)  $\text{Al}_2\text{O}_3$  Powder, b) Monel 400 Superalloy, c) Uncoated oxidized at  $1000^\circ\text{C}$ , d) Torn off surface after ISOT of  $\text{Al}_2\text{O}_3$  coated Monel 400 superalloy at  $1000^\circ\text{C}$

### 3.3 SEM analysis

Figure 6, shows the SEM micrograph of oxidized  $\text{Al}_2\text{O}_3$  coated Monel 400 superalloy. In the figure 6(a), a densified coating structure was observed with few pinholes and longitudinal

cracks with a short length. It indicates the good bonding of  $\text{Al}_2\text{O}_3$  coating with Monel 400 superalloy. Pin-holes and surface crack facilitated the conduction of heat flux and enhanced the thermal conductivity at high temperature.

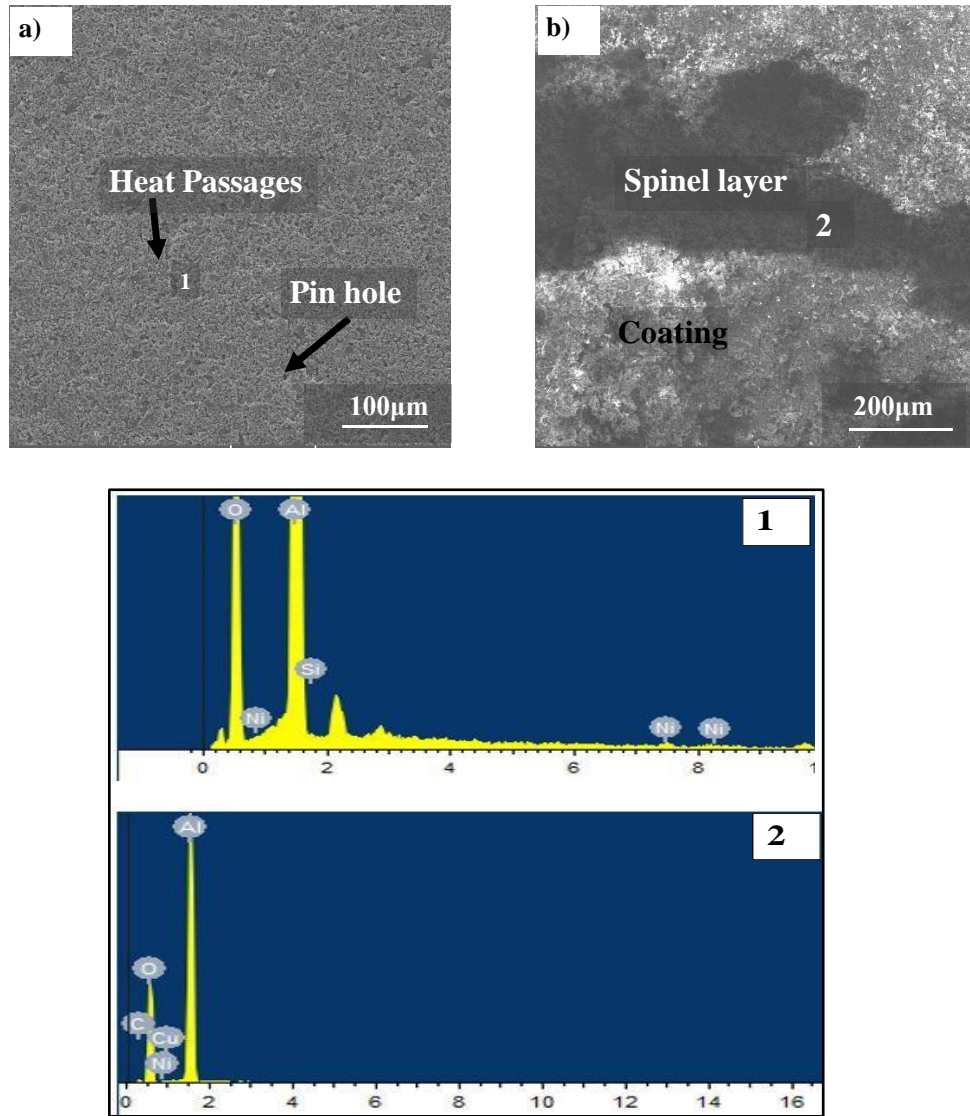


Figure 11. SEM and EDS analysis of  $\text{Al}_2\text{O}_3$  coated Monel 400 a) the coating morphology after ISOT at 800°C b) after isothermal oxidation test at 1000°C, c) point analysis of coating, d) EDS analysis of surface crack at 1000°C



Table 4 shows the EDS analysis of oxidized coated substrate at temperatures 800°C and 1000°C (Figure 5c-d) to get an understanding of oxidation mechanism at the internal surface layer. Point analysis of coating confirmed that Al<sub>2</sub>O<sub>3</sub> and NiO were present at the coating surface, but EDS analysis does not show the presence of CuO (Table 4). EDS at crack region indicates the higher concentration of Al and Ni that indicates the stability of oxides at the surface [1].

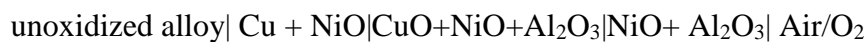
Table 6. EDS analysis of Al<sub>2</sub>O<sub>3</sub> deposited Monel 400 after isothermal oxidation test at 800°C and 1000°C a) the coating morphology after ISOT at 800°C b) At the torn off surface of coating at 1000°C

Element	EDS (a)		EDS 2 (b)	
	Weight%	Atomic%	Weight%	Atomic%
O K	55.65	68.04	59.84	67.02
Al K	43.80	31.75	31.91	21.19
Si K	0.08	0.06	--	--
Ni K	0.47	0.16	7.81	11.65
C K	--	--	0.02	0.01
Cu K	--	--	0.41	0.12
Total	100.00		100.00	

### 3.4 Discussion

The coated Monel 400 substrates show a lower oxidation rate as compared to uncoated substrates. This indicated that thick oxide scale was composed of NiO [18] [25]. The weight gain reduction for coated substrates was ½ fraction of uncoated substrates. The XRD analysis of the oxidized surface of coated substrates revealed the existence of thermodynamically stable oxide scale and spinel oxides of CuAlO<sub>2</sub>, Fe<sub>3</sub>O<sub>4</sub>, CuFe<sub>2</sub>O<sub>4</sub> and NiMn<sub>2</sub>O<sub>4</sub>. For uncoated substrates, Cu<sub>2</sub>O formation was observed and predominates the oxidation of bare substrates. At 600°C, oxidation kinetics involves the formation of Cu<sub>2</sub>O and NiO [25]. However, in this study, at 600°C to 1000°C, NiO predominated the oxidation process for coated substrates.

Coating durability depends on the thermal and mechanical response of coating to i.e. excessive oxide growth, volumetric expansion and diffusion of oxygen. During sintering process, volumetric expansion evolved residual tensile stresses and discouraged the bonding between coating and substrate. Although sintering process involved the pores' re-distribution, healing up the cracks and shifting of the grain boundaries. The excessive growth of oxide scale started to compel coating from the substrate surface and proceed towards delamination of coating [1]. Al<sub>2</sub>O<sub>3</sub> has low thermal conductivity and a very good match of coefficient of thermal expansion with the Monel 400 superalloy. At 1000°C, the formation of gaseous oxide weakened the interface and participated in the cracking of coating [26]. Volatile oxides e.g. CuO, started to evaporate at 1000°C and caused propagation of cracks at the coating surface (Table 4). The growth of oxide scale with spinel formation collectively affect the coating sustainability. During cooling, thermal expansion mismatch between coating and substrate caused residual compressive stresses that caused undulation at the surface. These all factors participate in the oxidation kinetics at high temperature. Oxidation kinetics depends on the surface microstructure and thermal conductivity of coating. Although coating prevented the surface of Monel 400 alloy from being ruptured and cracked but coating itself was cracked. Crack region shows a higher amount of oxygen, Ni but a little percentage of Cu which indicates the evaporation of CuO above 800°C. Based on above discussion, Figure 6 illustrated the oxidation mechanism at the surface of coated Monel 400. It indicates that oxide scale bonded with the Al<sub>2</sub>O<sub>3</sub> and got stabilized. Thermodynamically stable spinel oxides i.e. NiO.Al<sub>2</sub>O<sub>3</sub> and CuO.Al<sub>2</sub>O<sub>3</sub> reduced the thermal stresses [18]. Sintering at 600°C aims to promote thermodynamically NiO formation that safeguard the inner metal up-to 1300°C after this it becomes volatile. NiO formation predominated the oxidation mechanism from 500°C-800°C with Gibbs free energy  $\Delta G_b^0$  of 150 kJ/g atom oxygen (Pettit and Meier, 1984). It is inferred from the analysis that NiO oxide scale protected the alloy from further oxidation (Figure 6). The oxidation at specific temperature termed as selective oxidation [28]. Based on XRD and SEM/EDS analysis, the protective zone has following composition:





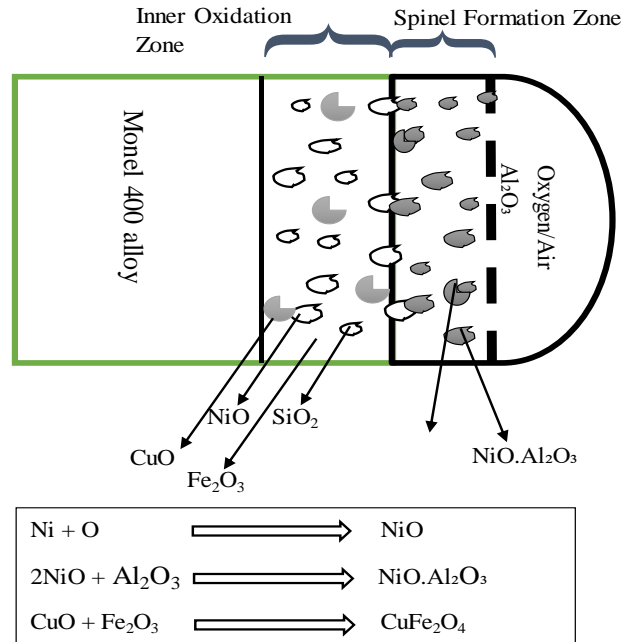


Figure 12. Schematic representation of inner oxidation mechanism and formation of spinel as an additional protective layer above the Monel 400 superalloy surface below the  $\text{Al}_2\text{O}_3$  coating. Figure 7 shows the crack free, adhering oxide layer at the surface of Monel 400 alloy. The image was taken from the cracked part of coating. As indicated that spinel oxides covered the surface and hindered the diffusion of oxygen beyond the oxide layer that was confirmed by weight gain curve. Parabolic rate law indicates the formation of oxide scale mainly consisted of  $\text{NiO}.\text{Al}_2\text{O}_3$ .  $\text{Al}_2\text{O}_3$  coating provided a sufficient protection to Monel 400 alloy.

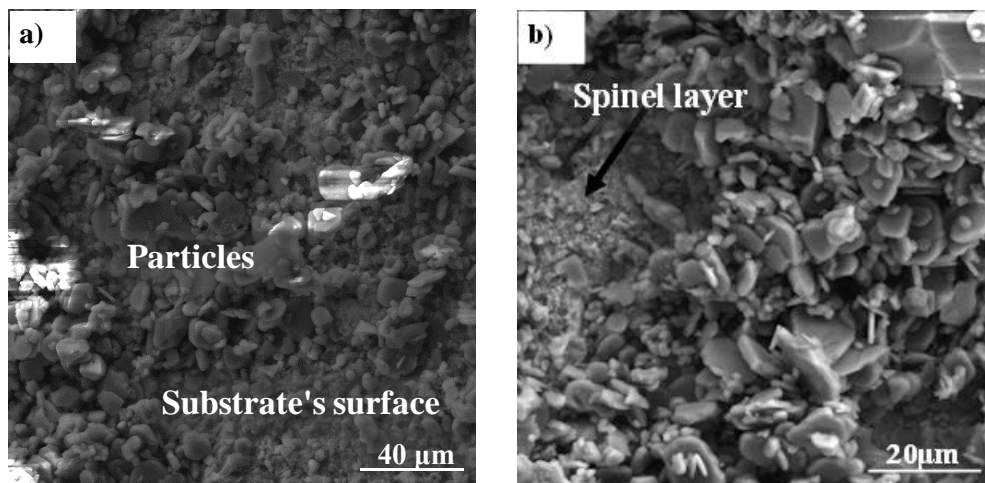


Figure 13. Monel 400 surface after removing a certain part of coating a) Spinel oxides, b) microstructure of spinel region

### 3.5 Thermal conductivity, porosity and pore distribution

Figure 8 (a-b) shows the surface microstructure of  $\text{Al}_2\text{O}_3$  coating before and after sintering respectively. Figure 8(a) shows that surface microstructure consisted of an uniform distribution of pores and microcrack. Before sintering, about 17 % surface porosity was measured via Image J software. Figure 8(b) shows a nano/microporous surface microstructure that increased the durability of coating. Thermal conductivity of coating depends on the pore fraction and morphology i.e. pore size and their shape. Higher porosity (nano/micropores) reduces the thermal conductivity while a lower porosity (macropores) increases the thermal conductivity of coating. Porous microstructure vanishes the thermal stresses generated at the interface.

Air (thermal conductivity= 0.024 W/m·K [29]) because of gravitational or surface tension forces, entrapped inside the pores and reduced the heat conduction through the coating. It is noted that surface tension effect predominates in nano/micropores while gravitational impact dominates in macropores and segmentation cracks. Although the study of heat transfer across nano/microporous coating still needs attention. For a good thermal barrier, certain fraction of pores is prerequisite. Figure 8(a) shows a large amount of microcracks those were filled with spinel oxides, i.e. NiO, CuO after sintering (Figure 8b). Sintering process reshape the surface microstructure of coating with a decrease in porosity and surface roughness from 17 % to 12% and  $7\mu\text{m}$  to  $2.5\mu\text{m}$  respectively. The average pore shape was measured to be  $1.37\mu\text{m} \pm 0.9$  via Image J software (Figure 9).

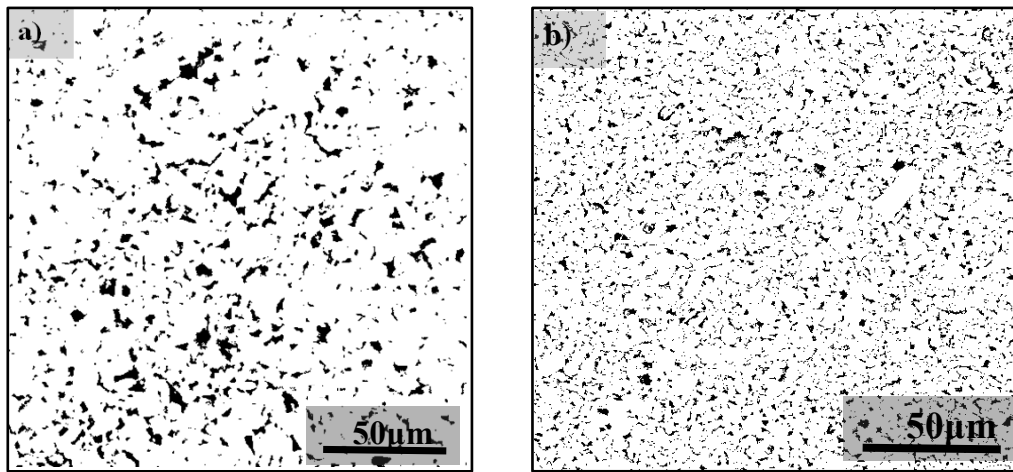


Figure 14. Pore size shrinkage and distribution, a) before sintering, b) after sintering

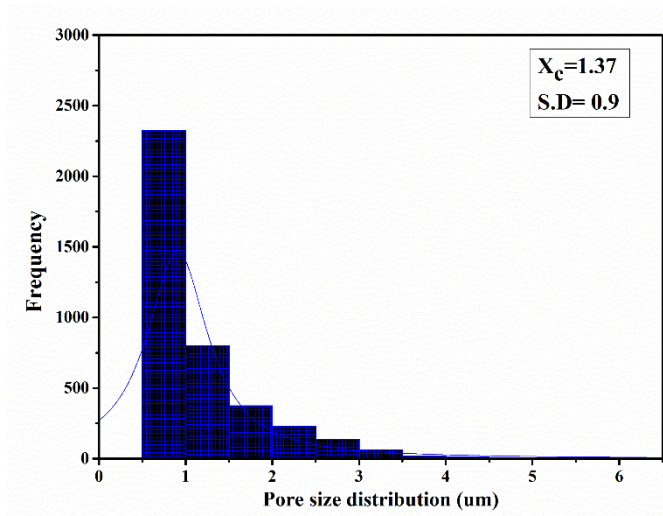


Figure 15. Pore size distribution after air-sintering at 600°C

Figure 10 indicates the inverse relation of thermal conductivity and porosity for four different porosity fractions. The porosity was determined to be 12-17% over the course of study. It is found that porosity was the dominant factor for controlling the thermal conductivity of coating. Instead of pores' characteristics, thermal conductivity also depends on the crack length, crack diameter and crack orientation [9], [30]. Heat flux is propagated through phonon (thermal energy carriers) at high temperatures via convection and radiative heat transfer. Phonons are scattered through pore spaces and conduction across nano/micropores provides high thermal insulation. This is consistent from the results that porosity provides a considerable impetus to reduce the thermal conductivity for Al<sub>2</sub>O<sub>3</sub> coatings [31]–[33]. Literature reported that pore fraction up to 40% have considerable effect on the thermal conductivity. Pore fraction greater than 40% will have direct relation with the thermal conductivity because at high temperature radiative heat transfer will be more effective [31]. Thermal conductivity of 12 % porosity Al<sub>2</sub>O<sub>3</sub> coatings was measured via Serial parallel law reported in [31], [34]

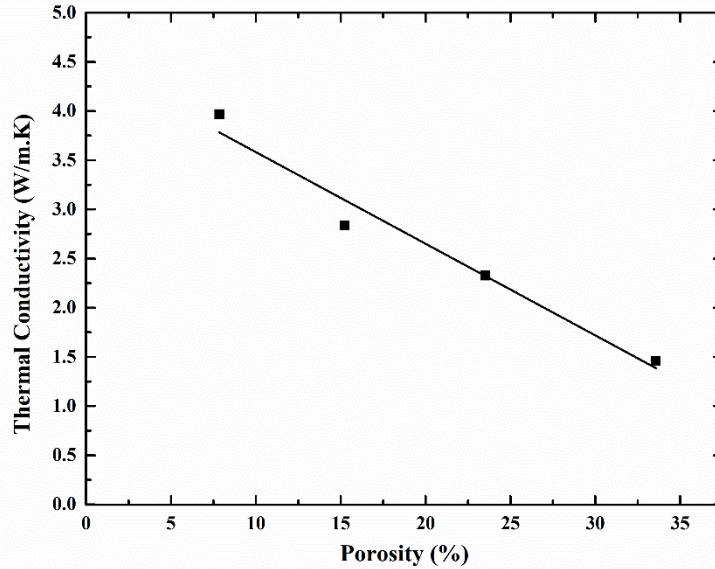


Figure 16. Effect of porosity on the thermal conductivity of Al<sub>2</sub>O<sub>3</sub> coating at 1000°C

Slurry based coatings have flatten microstructure with roughness parameter in few microns. Such kind of coatings can address the challenge of CMAS (calcium, aluminium, magnesium and silica) deposition in the columnar structure of EB-CVD, EB-PVD, etc coatings [30]. Flatten coating structure increases the heat outflow along with encounter the CMAS attack on the coating durability

## Conclusions

A single layer Al<sub>2</sub>O<sub>3</sub> based ETBC system was deposited on Monel 400 Superalloy via slurry dip coating process instead of the complex multi-layered system. The results showed that selective oxidation resulted in the transformation of single layer coating system into composite coating system. XRD analysis confirms the formation thermodynamically stable protective spinel oxides i.e. NiO.Al<sub>2</sub>O<sub>3</sub> and CuO.Al<sub>2</sub>O<sub>3</sub>, CuAlO<sub>2</sub>, Fe<sub>3</sub>O<sub>4</sub>, CuFe<sub>2</sub>O<sub>4</sub> and NiMn<sub>2</sub>O<sub>4</sub>. Based on oxidation kinetics, inner and outer zones were recognized as protective layer during sintering process. Coated substrates showed less weight gain as compared to uncoated substrates. Nano/microporous coating tended to decrease the thermal conductivity which could be controlled by particle size and sintering process.

Hence study concluded that nano/micropores coating prepared by slurry deposition are become cost effective for attaining the lower thermal conductivity at high temperature. Authors recommend the research of slurry-based coatings in terms of dip coating speed, heat transfer

via nano/microporous surface. Because these coatings exhibit high porosity and low roughness profile.

### **Acknowledgements**

The authors would like to thank Engr. Naveed Ali and Mr. Qamaruddin for their support to complete the characterization study of the project. Financial support by Higher Education Commission of Pakistan (HEC) under project NRPU-2801 is gratefully acknowledged.

## References

- [1] J. D. Osorio, A. Toro, and J. P. Hernandez-Ortiz, "Thermal barrier coatings for gas turbine applications: failure mechanisms and key microstructural features," *Dyna*, vol. 79, no. 176, pp. 149–158, 2012.
- [2] F. O. Soechting, "A Design Perspective on Thermal Barrier Coatings," *Journal of Thermal Spray Technology*, vol. 8, no. December, pp. 505–511, 1999.
- [3] R. Eriksson, "High-temperature degradation of plasma sprayed thermal barrier coating systems," Linkoping University, 2011.
- [4] K. N. Lee, "Protective coatings for gas turbines," *The gas turbine handbook*, pp. 419–437, 2006.
- [5] M. K. Chyu and S. C. Siw, "Recent Advances of Internal Cooling Techniques for Gas Turbine Airfoils," *Journal of Thermal Science and Engineering Applications*, vol. 5, no. 2, p. 21008, 2013.
- [6] J. D. Whittenberger, "HIGH-TEMPERATURE MECHANICAL PROPERTIES OF A ZIRCONIUM-MODIFIED, PRECIPITATION-STRENGTHENED NICKEL -30 PERCENT COPPER ALLOY," 1974.
- [7] K. D. Ramkumar, N. Arivazhagan, S. Narayanan, and D. Mishra, "Hot Corrosion Behavior of Monel 400 and AISI 304 Dissimilar Weldments Exposed in the Molten Salt Environment Containing  $\text{Na}_2\text{SO}_4 + 60\% \text{V}_2\text{O}_5$  at  $600^\circ\text{C}$  . Experimental Procedure," *Materials Research*, vol. 17, no. 5, pp. 1273–1284, 2014.
- [8] G. Gdowski, "Long-Term Corrosion/Oxidation Studies Under Controlled Humidity Conditions," 1997.
- [9] B. K. Jang and H. Matsubara, "Influence of rotation speed on microstructure and thermal conductivity of nano-porous zirconia layers fabricated by EB-PVD," *Scripta Materialia*, vol. 52, no. 7, pp. 553–558, Apr. 2005.
- [10] C. U. Hardwicke and Y. C. Lau, "Advances in thermal spray coatings for gas turbines and energy generation: A review," *Journal of Thermal Spray Technology*, vol. 22, no. 5, pp. 564–576, 2013.
- [11] K. Ito, H. Kuriki, H. Araki, S. Kuroda, and M. Enoki, "Detection of segmentation cracks in top coat of thermal barrier coatings during plasma spraying by non-contact

- acoustic emission method.,” *Science and technology of advanced materials*, vol. 15, no. 3, p. 35007, Jun. 2014.
- [12] P. W. Schilke, “Advanced Gas Turbine Materials and Coatings,” *GE Energy*, 2004.
- [13] M. Oksa, “Nickel and iron based HVOF thermal spray coatings for high temperature corrosion protection in biomass fired power plant boilers,” *JULKAISIJA - UTGIVARE*, 2015.
- [14] L. Wang *et al.*, “Effect of interface on the thermal conductivity of thermal barrier coatings: A numerical simulation study,” *International Journal of Heat and Mass Transfer*, vol. 79, pp. 954–967, 2014.
- [15] B. Baufeld, O. van der Biest, and H.-J. Raetzer-Scheibe, “Thermal and Mechanical Properties of Zirconia Coatings Produced By Electrophoretic Deposition,” *Advanced Ceramic Coatings and Interfaces II*, vol. 28, no. 3, pp. 3–10, 2008.
- [16] Z. S. Khan *et al.*, “Thermal cycling behavior and hot corrosion performance of the plasma sprayed Er<sub>2</sub>Si<sub>2</sub>O<sub>7</sub> coatings deposited on Cf/SiC composites,” *Journal of Asian Ceramic Societies*, vol. 3, no. 1, pp. 123–129, 2014.
- [17] S. Roy, S. R. Reddy, P. Sindhuja, D. Das, and V. V. B. Prasad, “AlPO<sub>4</sub>-C composite coating on Ni-based super alloy substrates for high emissivity applications: Experimentation on dip coating and spray coating,” *Defence Science Journal*, vol. 66, no. 4, pp. 425–433, 2016.
- [18] H. Zhang, Y. Liu, X. Chen, H. Zhang, and Y. Li, “Microstructural homogenization and high-temperature cyclic oxidation behavior of a Ni-based superalloy with high-Cr content,” *Journal of Alloys and Compounds*, vol. 727, pp. 410–418, 2017.
- [19] V. Sankar, “Thermal Barrier Coatings Material Selection , Method of Preparation and Applications - Review,” *International Journal of Mechanical Engineering and Robotics Research*, vol. 3, no. 2, pp. 510–517, 2014.
- [20] I. A. Mahmood, W. W. Jameel, & Lubna, and A. Khaleel, “Improved oxidation resistance for thermal barrier ceramic coating protect,” *International Journal of Research in Engineering & Technology*, vol. 1, no. 5, pp. 2321–8843, 2013.
- [21] A. K. Krella, A. T. Sobczyk, A. Krupa, and A. Jaworek, “Thermal resistance of Al<sub>2</sub>O<sub>3</sub> coating produced by electrostatic spray deposition method,” *Mechanics of Materials*,

- vol. 98, pp. 120–133, 2016.
- [22] X. J. Lu and P. Xiao, “Constrained sintering of YSZ/Al<sub>2</sub>O<sub>3</sub> composite coatings on metal substrates produced from electrophoretic deposition,” *Journal of the European Ceramic Society*, vol. 27, no. 7, pp. 2613–2621, 2007.
- [23] S. K. Khaja-abdul, “SLURRY BASED COATINGS ON SILICON BASED CERAMICS,” Cleveland State University, Cleveland OHIO, 2006.
- [24] S. M. Corporation, “Physical and thermal properties of Monel 400 alloy.” Special Metals Corporation, 2005.
- [25] Karl Hauffe, *Oxidation of Metals*, German Edi. Springer US, 1965.
- [26] F. S. Pettit and G. H. Meier, “Oxidation and Hot Corrosion of Superalloys,” *Superalloys 1984 (Fifth International Symposium)*, pp. 651–6877, 1984.
- [27] F. S. Pettit and G. H. Meier, “OXIDATION AND HOT CORROSION OF SUPERALLOYS.”
- [28] M. Seraffon, N. J. Simms, J. R. Nicholls, J. Sumner, and J. Nunn, “Performance of thermal barrier coatings in industrial gas turbine conditions,” *Materials at High Temperatures*, vol. 28, no. 4, pp. 309–314, 2011.
- [29] Y. Cengel, “Heat Transfer: A Pratical Approach,” *McGraw - Hill*, p. 932, 2002.
- [30] H. Zhao, F. Yu, T. D. Bennett, and H. N. G. Wadley, “Morphology and thermal conductivity of yttria-stabilized zirconia coatings,” 2006.
- [31] T. Shimizu, K. Matsuura, H. Furue, and K. Matsuzak, “Thermal conductivity of high porosity alumina refractory bricks made by a slurry gelation and foaming method,” *Journal of the European Ceramic Society*, vol. 33, no. 15–16, pp. 3429–3435, Dec. 2013.
- [32] R. Askari, S. Taheri, and S. H. Hejazi, “Thermal conductivity of granular porous media: A pore scale modeling approach,” *AIP Advances*, vol. 5, no. 9, p. 97106, Sep. 2015.
- [33] A. K. Krella, A. T. Sobczyk, A. Krupa, and A. Jaworek, “Thermal resistance of Al<sub>2</sub>O<sub>3</sub> coating produced by electrostatic spray deposition method,” *Mechanics of Materials*, vol. 98, pp. 120–133, 2016.



## Data Article

**Title:** Data on slurry deposition of alumina for oxidation protection of Monel 400 superalloy

**Authors:** Maria Sattar, Mariah Batool, Zuhair S. Khan\*

**Affiliations:** US. Pakistan Centre for advance Studies in Energy (USPCAS-E) National University of Sciences and Technology Islamabad, 44000 Pakistan

**Contact email:** zskhan@ces.nust.edu.pk\*

## Abstract

The dataset presented herein is the research summary of the “Oxidation protection study for Monel 400 Superalloy via slurry deposition of  $\text{Al}_2\text{O}_3$  coating for gas turbine engine application”. This dataset help reader in the context of oxidative weight gain of alumina coated Monel 400 superalloy at 600°C, 800°C, 1000°C in an air atmosphere. The reader can learn about the oxidation mechanism at the surface of Monel 400 superalloy after employing alumina as environmental and thermal barrier coating. Meanwhile, it will also provide the information on spinel growth as an additional thermal shield at the interface. This dataset will help the reader to address the challenge of extensive surface oxidation of Monel 400 superalloy at a High-Temperature >600°C. Weight gain cure during thermal exposure was acquired for an insight regarding designing and multifunctional use of developed coating for gas turbine engine application in surface engineering.

## Specifications Table

Subject area	Materials Engineering, Energy Systems Engineering
More specific subject area	Surface engineering
Type of data	Table, text file, graph,
How data was acquired	The coating was deposited using dip coater while following the all mentioned steps from prior surface treatment to post-deposition treatment. Surface roughness was measured by using roughness

	tester Model No. NDT 110. Weight gain was measured by using weighing balance. Deposition efficiency was obtained from the weight of coating( $G_c$ ) and expended material ( $G_p$ ) during deposition, and oxidation rate was calculated from weight gain measurements by using equations.
Data format	Raw, analyzed, etc.
Experimental factors	The substrate surface was sandblasted at 0.4 MPa air pressure to roughen the substrate surface for good deposition. After sand blasting, the roughened substrate was acetone washed and sonicated to remove the impurities entrapped at the substrate surface.
Experimental features	Dip coater speed was adjusted after performing multiple experiments. Surface roughness was measured. The weight of uncoated substrate was measured by using an analytical weighing balance with 0.05g. The coating was deposited in a duration of 5-20 min with a dip coater speed of 25mm/min at room temperature. The drying process of the coating was kept in consideration because it can affect the adherence of coating at the surface.
Data source location	USPCAS-E National University of Sciences and Technology Islamabad, Pakistan
Data accessibility	Data are available within this article
Related research article	NA

### Value of the Data

1. The data presented here can help researcher to focus on simple coating system instead of complex multilayer coating system
2. The data will give an insight to researcher about slurry deposition as cost-effective approach with high deposition efficiency
3. The data will help the research to investigate the effect of binder on the coating deposition

4. The data presented here will be prolific to evaluate the performance of alumina coating in terms of weight gain, crack propagation, deposition efficiency, etc.
5. The data can be used to understand the productive spinel formation and oxidation mechanism at the interface of coated Monel 400 superalloy.

### **Data**

Coating deposition efficiency, weight gain cure, and oxidation rate were collected, and a novel way of coating deposition has been introduced in a cost-effective manner. Surface roughness was measured about 0.42  $\mu\text{m}$ . The deposition process was performed within 5-20 min at a dip-coater speed of 25 mm/min at room temperature. Coating deposition was performed for twice to ascertain the slurry deposition from the same alumina slurry. The data acquired after isothermal oxidation testing was running twice for two separate Monel 400 alloy substrates. The variable data of dip-coater speed, weight gain, coating weight were each taken twice and then averaged for better representation of data.

### **Experimental Design, Materials, and Methods**

Dip coating method was used to deposit the  $\text{Al}_2\text{O}_3$  coating on Monel 400 superalloy substrates. Monel 400 superalloy substrate was cylinder shaped with dimensions of 1x1.3 cm. The Monel 400 superalloy substrates were sandblasted, acetone washed, and sonicated prior to coating deposition in reference to [1]-[2]. The physical and chemical properties of Monel 400 superalloy are given in table 1 & 2 respectively [9]. The alumina powder purchased from China leadmat advanced materials was used after manual grinding in mortar and pestle. The average particle size of alumina was 2.5  $\mu\text{m}$  [3]. Alumina slurry was prepared according to [4]–[8]. The deposition parameters are in line with other authors as [4], [7]. Data for oxidation at 600°C, 800°C, 1000°C will be found in Figure 1.

### **Acknowledgments**

Authors would also acknowledge the financial support by Higher Education Commission of Pakistan (HEC) under project NRPU-2801. Authors would like to thank Engr. Naveed Ali and Mr. Qamaruddin for their support to complete the characterization study of the project

### **References**

- [1] S. Das, “Study of plasma spray alumina - aluminide composite coating on metals”,

- Department of Physics, National University of Technology Rourkela, India, 2007.
- [2] J. Zhan *et al.*, “Technics and performance analysis of Monel alloy coating prepared by high velocity arc spraying,” *Mater. Res. Innov.*, vol. 8917, no. April, 2016.
  - [3] V. Meille, “Review on methods to deposit catalysts on structured surfaces,” 2006.
  - [4] S. K. Khaja-abdul, “Slurry based coatings on silicon based ceramics,” 2006.
  - [5] X. Lu, D. Yan, Y. Yang, Y. Dong, J. He, And J. Zhang, “Phase evolution of plasma sprayed  $\text{Al}_2\text{O}_3$ –13% $\text{TiO}_2$  coatings derived from nanocrystalline powders,” *Trans. Nonferrous Met. Soc. China*, vol. 23, no. 10, pp. 2951–2956, 2013.
  - [6] D. D. L. Chung, “Review: Acid aluminum phosphate for the binding and coating of materials,” *J. Mater. Sci.*, vol. 38, no. 13, pp. 2785–2791, 2003.
  - [7] T. Mori, S. Yamada, and N. Iwata, “Effects of suspension properties on the microstructure of  $\text{Al}_2\text{O}_3$  coatings deposited onto macroporous SiC substrate,” *Surf. Coat. Technol.*, vol. 326, pp. 1–10, 2017.
  - [8] B. Zou *et al.*, “Microstructure, oxidation protection and failure mechanism of  $\text{Yb}_2\text{SiO}_5/\text{LaMgAl}_{11}\text{O}_{19}$  coating deposited on C/SiC composites by atmospheric plasma spraying,” *Corros. Sci.*, vol. 62, pp. 192–200, 2012.
  - [9] USA specialmetals Corporation, “Physical Constants and Thermal Properties of Monel Alloy 400.”

# Annexure II

## **Al<sub>2</sub>O<sub>3</sub>-coated C/SiC Composite for Gas Turbine Applications: Thermal Shock Testing and Microstructural Analysis**

Authors: **Maria Sattar**, Mariah Batool, Muhammad Ijaz Tahir, Zuhair S. Khan \*

U.S. Pakistan Center for advanced studies in Energy (USPCAS-E), National University of Sciences and Technology (NUST), Islamabad, 44000, Pakistan

\*[zskhan@ces.nust.edu.pk](mailto:zskhan@ces.nust.edu.pk) Tel: +9251-90855276

### **Abstract**

This study presents the thermal shock performance of an Al<sub>2</sub>O<sub>3</sub>-coated 2D-C/SiC composite. Alumina was deposited on 2D-C/SiC composite through a cost-effective slurry-based dip-coating process. Coatings were vacuum dried and sintered at 1073 K in air for 3 h to encourage bonding between the coating and the C/SiC composite. To examine the coating adherence and integrity, the coated specimens were then subjected to thermal shock testing in air between 1273 K and room temperature for 26 cycles. The weight change rate during sintering was about 0.033 mg/s.cm<sup>2</sup>. During thermal shock testing, coating maintained its integrity, without further oxidation and peeling off. Material characterization techniques including XRD, SEM, and EDS were employed to examine the physicochemical changes in coating over the course of thermal shock testing, while porosity and surface roughness were analyzed using ImageJ software package. This study introduces a novel way to develop alumina coating capable of enduring thermal stresses during thermal shock testing. Sintering at 1073 K, resulted in an interlock interface which was beneficial to alleviate the mismatch of coefficient of thermal expansion between Al<sub>2</sub>O<sub>3</sub> coating and C/SiC composite. Coating with 8–15% surface porosity, 7-16 μm surface roughness with thickness 260 μm, provided significant thermal shock resistance without the need of any supplementary coating.

**Keywords:** Al<sub>2</sub>O<sub>3</sub>; Air-sintering; coating thickness; Slurry-dip coating; surface porosity; thermal shock resistance;

## **Introduction**

Due to their outstanding properties including low coefficient of thermal expansion (CTE), high thermal conductivity, low density, and high thermal shock resistance, carbon fibre reinforced silicon carbide matrix composites (C/SiC) are promising candidate as thermal structural materials for applications such as gas turbine engines for power/steam cogeneration, heat exchangers and advanced internal combustion engines [1–7]. The components made of C/SiC are subject to thermomechanical environment where thermal shock/transient conditions often take place. Although C/SiC exhibits high thermal shock resistance, these are prone to oxidation at temperatures approaching and exceeding 400°C. Therefore, it is the need of hour to improve the capability of C/SiC under oxidizing environment. Matrix cracking because of CTE mismatch between fibre and matrix; and thermal shock crack production are challenges in high-temperature application of C/SiC composites in aerospace, automotive, and nuclear industry. Apart from matrix cracking, thermal shocks can cause cracks growth in the coating and the interface and peeling off coating from the surface [1]. The main approaches to improve the thermal shock resistance of C/SiC in oxidizing environment include: 1) environmental and thermal barrier coatings (ETBCs); 2) cooling techniques; and 3) matrix improvements [2], [8], [9]. Among these, ETBCs are the preferred approach because it inhibits the direct contact of hot gas to the substrate's surface and protect the composites from high-temperature oxidation.

Oxide ceramics such as Al<sub>2</sub>O<sub>3</sub> [7], [10]–[14], yttrium silicate coatings [15], and yttria-partially stabilized zirconia [16], SiC/Si-Mo[4], SiC/B<sub>4</sub>C-B<sub>2</sub>O<sub>3</sub>-SiO<sub>2</sub>-Al<sub>2</sub>O<sub>3</sub>, SiC/Zr-Si-C, AlPO<sub>4</sub>-SiC-MoSi<sub>2</sub>/SiC [17], ZrO<sub>2</sub> [16]–[19], mullite and mullite based coatings[20], are some of the candidate materials for coating applications. Pure Al<sub>2</sub>O<sub>3</sub> and Al<sub>2</sub>O<sub>3</sub>-based materials are frequently used as protective and heat-resistant coatings which can undergo high thermal shock/transient conditions during their operations. Al<sub>2</sub>O<sub>3</sub> coatings are well-known for their robustness, even in oxidizing and corrosive environments, because of their high melting point (2045°C), high CTE ( $\alpha=8.4\times 10^{-6} \text{ K}^{-1}$ ), moderate thermal conductivity (20 W/m·K), phase stability, chemical inertness and hardness [19]. However, pure Al<sub>2</sub>O<sub>3</sub> coatings exhibit high porosity and low

fracture toughness that can be improved by reducing the particle size. Particles with 1-5 microns increase the ductility of coating [10]

Various deposition techniques are employed for  $\text{Al}_2\text{O}_3$  coating such as electrostatic spray deposition [10], plasma spraying [21], electron beam-chemical vapour deposition (EB-CVD) and physical vapour deposition (PVD) [22], atomic layer deposition [13], and slurry-sintering [7]. In CVD deposition, high temperature accompanied with oxygen is detrimental for the C/SiC composites [13]. In thermal spraying processes, the coating material is sprayed at a temperature that is higher than its melting point, leading to extensive mass change along with reduction in fracture strength of C/SiC composite. With these deposition techniques, it is also difficult to coat complex shaped components. Furthermore, spraying processes require surface roughening either by grit blasting or chemical etching, for enhancing the chemical interlocking of coating material and specimen. However, surface roughening process entails lowered fracture strength, e.g., fracture strength of  $\text{Si}_3\text{N}_4$  was lowered by 50% and 15% at room temperature and high temperature, respectively [23].

There is a need to develop a cost-effective, highly productive and non-energy intensive deposition process for ETBCs without altering the thermomechanical properties of C/SiC composites. Slurry-dip coating process is capable of coating ETBCs on complex shaped components with densified microstructure. When accompanied with sintering, it promotes chemical interlocking between coating and specimen and develops a strain-tolerant nano/micro-porous microstructure in thermal resistant coating [4], [14], [23-25]. Through slurry-dip coating process, coatings of 200-500  $\mu\text{m}$  thickness can be developed depending on the viscosity and deposition rate of slurry [20].

This study focussed on deposition of  $\text{Al}_2\text{O}_3$  via slurry-dip coating process followed by air-sintering at 1073 K. Air-sintering of  $\text{Al}_2\text{O}_3$ -coated C/SiC specimen resulted in the formation of refractory  $\text{SiO}_2$  layer at the interface. This thin self-healing layer protects the C/SiC from catastrophic oxidation by minimizing the diffusion of  $\text{O}_2$  and preserves the fracture toughness of C/SiC.  $\text{Al}_2\text{O}_3$  coating provides the heat and corrosion resistance, while the  $\text{SiO}_2$  offers the oxidation protection of C/SiC in an oxidizing and corrosive environment. In the present work, thermal shock resistance of  $\text{Al}_2\text{O}_3$ -coated C/SiC composite by dynamic thermal shock cycling between 1273 K and room temperature has been evaluated. Material characterization techniques including XRD, SEM, and

EDS were employed to examine the physicochemical changes in coating over the course of thermal shock testing, while porosity and surface roughness were analysed using ImageJ software package.

Table 7. Review of deposition techniques and sintering temperatures of environmental and thermal barrier coatings

Specimen-material	Material	Deposition technique	System	Sintering temp. (°C)	Medium	Thermal cycling Temp. (°C)
C/SiC [26]	SiC+TiB <sub>2</sub>	CVD	Single		Vacuum	1100
SiC [7]	Al <sub>2</sub> O <sub>3</sub> -Mullite	Slurry-dip	Single & duplex	1200	Air	1200
C/SiC [27]	SiC/Si-Mo	CVD + Slurry painting	Multilayer	1500	Air	1400
SiC & Si <sub>3</sub> N <sub>4</sub> [20]	Mullite/Gd <sub>2</sub> SiO <sub>5</sub>	Slurry	Multilayer	1300	Air	
C/C [28]	SiC	Pack cementation	Single layer	1500	Argon	1500
C/C [29]	ZrB <sub>2</sub> -SiC-Si/Yb <sub>2</sub> SiO <sub>5</sub> /LaMgAl <sub>11</sub> O <sub>19</sub>	Plasma spraying	Multilayer	2000	Air	2000
C/C [17]	ZrO <sub>2</sub> -SiC	Atmospheric plasma spraying	Multilayer	2000	Air	2700
C/SiC [30]	Si-Zr-SiC	Liquid reaction and CVD	Multilayer	1500	Air and argon	1300
X10CrAlSi18 steel [14]	Al <sub>2</sub> O <sub>3</sub> -TiO <sub>2</sub>	Electrostatic spray deposition	Multilayer	1000	Air	1000
C/SiC [15]	Y <sub>2</sub> SiO <sub>5</sub> -SiC	Dip coating	Multilayer	1600	Vacuum	1600-400
Sapphire [31]	ZrO <sub>2</sub>	EPD	Single layer	1100	Air	

## Experimental

Specimens having dimensions of 10 mm × 8 mm × 5 mm were cut from the bulk 2D-C/SiC composites using a diamond saw at a speed of 95 rpm. 2D-C/SiC prepared via reaction melt infiltration process exhibited a coefficient of thermal expansion (CTE) of  $3.5 \times 10^{-6} \text{ C}^{-1}$  and a



thermal conductivity of 120 W/m.K. Specimens were first hand-polished using a 220-grit sand paper, then cleaned with acetone, and finally sonicated at 80°C for 2 h. After surface preparation, specimens were placed in the clamp and fixed at the dip-coater rotating plate. A special water bath arrangement was made inside the dip-coater to suppress the shrinkage effect during room temperature drying.

Firstly, Al<sub>2</sub>O<sub>3</sub> powder and polyethyleneimine (as a binder) diluted in distilled water, were thoroughly mixed until a well-mixed slurry was prepared. Al<sub>2</sub>O<sub>3</sub> powder was ground in a mortar and pestle to refine the grain size in the range of 1–5 μm. The roughness of specimens was measured using a surface roughness tester (Surface roughness tester Model No. NDT 110, Hong Kong). The roughness parameter Ra (arithmetic mean of the absolute values of the profile deviations) was found to be around 0.24 μm.

The deposition process, which consisted of three steps: 1) insertion, 2) residence, and 3) exertion, was carried out using a dip-coater. Coating thickness depends on the slurry viscosity, deposition rate, and sintering process, respectively. In the present study, 1073K was selected as sintering temperature after studying the reported sintering temperatures at the ETBCs (Table 1). After an overnight drying of the coated-specimens at room temperature, they were further vacuum dried at 250°C for 2 h. Afterwards, the coated-specimens were sintered in air at 1073 K to develop a SiO<sub>2</sub> layer that provides the oxidation resistance to C/SiC composite at high temperature. The weight measurements of the specimens were conducted to evaluate the mass change using an electronic weighing balance having a sensitivity of 0.001 g. The mass change rate ( $R_m$ ) of specimens was calculated by Eq. (1) [32].

$$R_m = \left( \frac{m_1 - m_2}{A \times t} \right) \quad (3)$$

where  $m_1$  and  $m_2$  are the weight in grams before and after testing, respectively.

The isothermal oxidation tests (ISOT) were conducted in a box furnace for certain periods of time at 1273 K in an air atmosphere. After the tests, the specimens were remained inside the furnace and cool down naturally. Subsequently, specimens were weighed to measure the mass change. Coating morphology was analyzed for structural changes during oxidation process. Thermal shock test in air was performed between 1273 K and room temperature. Dynamic thermal shock cycle comprised of these segments: insertion of coated specimen inside a pre-heated tube furnace at 1273 K; letting it stay there for 5 min, and then immediate air exertion at room temperature followed by

manual cooling process at 40°C for 4 min. A total of 25 thermal cycles were performed with abovementioned procedure, however, at 26<sup>th</sup> thermal cycle, specimens were placed inside the tube furnace for 30 min and cooled down naturally at room temperature. The overall process completed in 250 min excluding the 26<sup>th</sup> cycle cooling duration. The mass change of coated specimens was measured after every 5 thermal cycles.

Phase structure of coating was studied by XRD (D8, Advance Bruker X-ray diffractometer) with Cu K $\alpha$  radiation generated at 40 KV and 30 mA. The scanning rate was 9 step/sec with a step size of 0.02° over a range of 20° to 70°. Surface and cross-sectional studies were conducted with the help of SEM/EDS (Vega3 TEScan scanning electron microscope equipped with Oxford EDS). ImageJ software was used to calculate the porosity and surface roughness of coating over the course of the study.

## **Results and discussions**

### **Oxidation mechanism of C/SiC during sintering at 1073 K**

The oxidation protection of C/SiC depends on the sintering temperature. For the selection of appropriate sintering temperature, volatility of silica needs to be accounted for. Active oxidation dominates at a temperature of ~873 K and the resulting oxidation products comprise of volatile oxides, i.e., SiO, CO and/or CO<sub>2</sub> [33]. At temperatures higher than 1373 K, SiO<sub>2</sub> becomes volatile [15]. Accordingly, a sintering temperature of 1073 K was used in this study at which the silica layer develops and deposits over the surface; this deposited SiO<sub>2</sub> provides protection against catastrophic high-temperature oxidation up to 1996 K [7]. Moreover, this sintering temperature was considered appropriate to establish interfacial bonding between the coating and the specimen. During sintering, passive oxidation dominates with the formation of amorphous SiO<sub>2</sub> layer that solidifies during cooling process after sintering. The formation of SiO<sub>2</sub> reduces the risk of coating failure because of CTE transition between composite and Al<sub>2</sub>O<sub>3</sub> coating. Al<sub>2</sub>O<sub>3</sub> has a higher CTE than C/SiC, which can cause delamination of coating. The values of  $\alpha$  for SiO<sub>2</sub>-C-SiC and SiO<sub>2</sub>/SiC are  $5.4 \times 10^{-6}$  and  $8.5 \times 10^{-6}$  respectively [33]. Fig. 1 shows that after sintering, the developed cross-section of Al<sub>2</sub>O<sub>3</sub>-SiO<sub>2</sub>-C/SiC has a CTE gradient, i.e.,  $8.5 \times 10^{-6} - 5.4 \times 10^{-6} - 3.5 \times 10^{-6}$ . The Sintering at 1073 K resulted in a densified and compact microstructure that suppressed the crack growth in the coating.

At the start of oxidation, the mas change was in terms of mass loss due to active oxidation of carbon fiber and SiC into CO/CO<sub>2</sub> and SiO respectively. Active oxidation of carbon fibers and SiC

matrix increased the nucleation sites that stimulated the passive oxidation for the formation of  $\text{SiO}_2$  and suppressed further oxidation of  $\text{SiC}$ . Zou et al. [29] reported a Gibbs free energy of  $-180$  Kcal/mol for  $\text{SiO}_2$  at  $1000$  K and a kinetic energy for the reaction of carbon with oxygen as  $28$  Kcal/mol [30]. The reactions are thermodynamically feasible because  $G_T^0 < 0$  for the whole reaction.

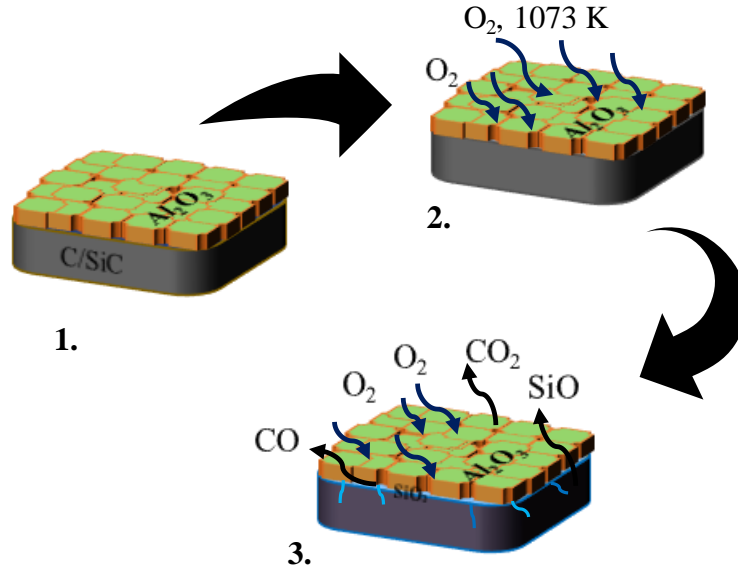
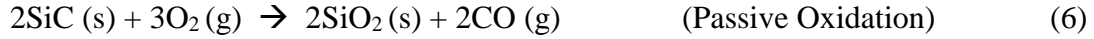


Fig. 17. Schematic representation of mass change mechanism for  $\text{Al}_2\text{O}_3$ -coated  $\text{C/SiC}$  composite during air sintering at  $1073$  K

### Factors affecting adherence of coating

The CTE of hexagonal  $\text{Al}_2\text{O}_3$  and  $\text{C/SiC}$  are about  $9.3 \times 10^{-6}$  [7] and  $3.5 \times 10^{-6}$  [34] respectively over a temperature range of  $298$  to  $1273$  K. The difference in CTE has serious impact on the coating adherence that leads to extensive thermal stresses at the interface during thermal cycling. Thus  $\text{Al}_2\text{O}_3$  coating faced shrinkage during drying process more than the  $\text{C/SiC}$  specimen [7]. Shrinkage caused tensile stresses and initiated the crack production. As deposited coating has loose aggregates of particles at the surface and retains high porosity (Fig. 5a) that requires sintering at high temperature to increase the bond-strength of coating. To behave like a ceramic body, coating needs augmentation in microstructure. During sintering, oxidation of  $\text{SiC}$  resulted in the production of  $\text{SiO}_2$  (Fig. 1). However, after sintering, coating has the best match of CTE because of  $\text{SiO}_2$  formation at the interface. The presence of  $\text{SiO}_2$  on the surface has been confirmed by XRD (Fig. 2).  $\text{SiO}_2$  acts as an industrious transition for CTE mismatch that is prerequisite for thermal resistant coatings. Formation of  $\text{SiO}$  and  $\text{SiO}_2$  depends on the oxygen pressure, at higher

pressure, a mass gain is observed with the formation of SiO<sub>2</sub> according to either equation 4 or 5 [35]



### Effect of sintering on the microstructure of coating

Fig. 2. shows the mass change rates of multiple Al<sub>2</sub>O<sub>3</sub> coated C/SiC composite specimens after air-sintering at 1073 K. After sintering, an average mass change rate of 0.033 mg/s.cm<sup>2</sup> and corresponding surface porosity of 12% (average of 3-specimens) was observed. It can be seen from Fig. 3a that the as-deposited coating was composed of hexagonal Al<sub>2</sub>O<sub>3</sub> with high-intensity peaks according to ICSD # 78-2427. Fig. 3b shows the appearance of SiO<sub>2</sub> produced by passive oxidation of SiC during sintering process according to equation 4 and 5. SiO<sub>2</sub> surrounded the alumina particles and sealed up the cracks and voids.

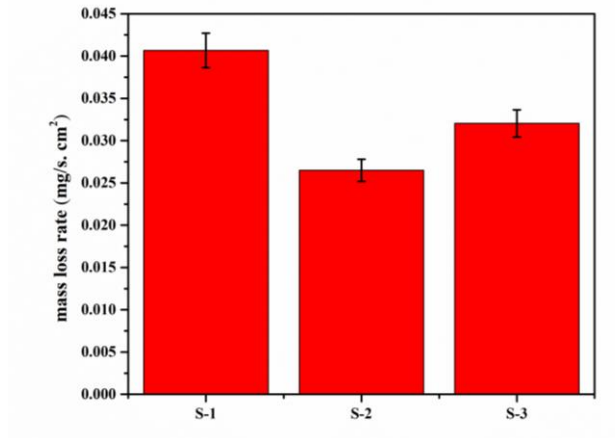


Fig. 18. Mass change rate after air-sintering of Alumina-coated C/SiC composite at 1073 K for 3

h

Fig. 3b indicates that  $\text{Al}_2\text{SiO}_5$  was formed at  $2\theta$  of  $35.66^\circ$  and  $60.04^\circ$ , confirmed by ICSD patterns 73-1763 and 74-2217 with phase structure of orthorhombic and triclinic. It is indicated that liquid  $\text{SiO}_2$  surrounded the  $\text{Al}_2\text{O}_3$  particles and gripped tightly after cooling. The presence of  $\text{SiO}_2$  at the surface indicates that the cracks were filled up with  $\text{SiO}_2$  that strengthened the interfacial bonding and enhanced the ductility of the coating.

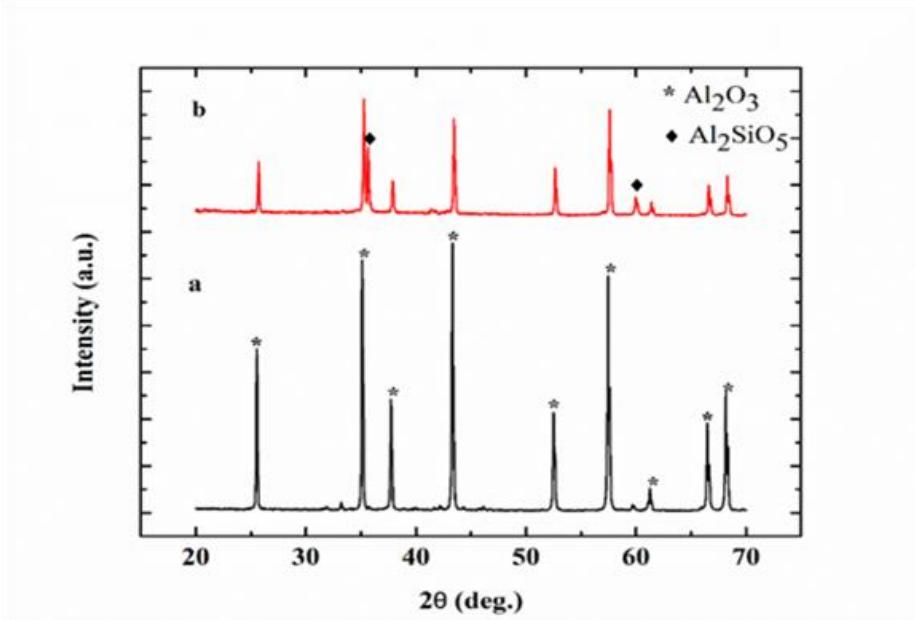


Fig. 19. XRD spectra of  $\text{Al}_2\text{O}_3$  coating (a) before and (b) after sintering at 1073 K

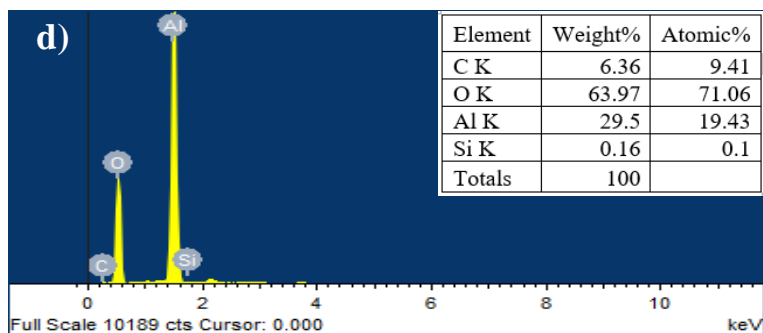
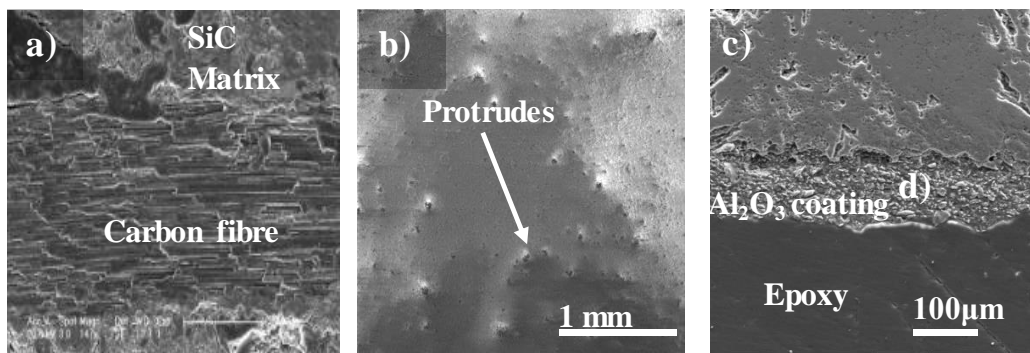


Fig. 20. SEM image of (a) C/SiC; (b) As-deposited coating; (c) cross-section of sintered coating sintered coating, and (d) EDS spectra of alumina coating after sintering

Fig. 4a is the SEM image of C/SiC composite that indicated the embedment of SiC matrix between the fibres. Fig. 4b shows the smooth surface of the as-deposited coating with some protrusions on it. The development of protrusions is attributed to agglomeration of particles at the surface. Slurry coating process resulted in smooth coatings with appropriate coating thickness (100–400  $\mu\text{m}$ ). Slurry coat and coating thickness depends on the particle loading of slurry; high particle loading results in thick coating, but it can affect the adherence of coating. In this study, successive 3–5 dip-coats of slurry resulted in coating thickness of about 250–400  $\mu\text{m}$ . Fig. 4c shows the cross-section of coating that is homogenous, crack free and densified in nature. Coating thickness was measured via ImageJ analysis software.

Fig. 5a–c and Fig. 5d–f show the microstructure of coating before and after sintering process, respectively. Fig. 5b shows the binary image of the as-deposited coating, which shows the distribution of smaller and larger pores all over the surface with an average pore size of 2.04  $\mu\text{m}$ . High solid loading of slurry-based coating resulted in dense microstructure with a thick layer. Upon sintering, the surface cracks were sealed by  $\text{SiO}_2$  thereby improving the coating microstructure. It can be seen from fig. 5e that after sintering, reduction in pore size was observed with an average pore size of 0.839  $\mu\text{m}$ . It demonstrates the effect of sintering on the grain boundary shift of  $\text{Al}_2\text{O}_3$  at 1073 K. During high-temperature sintering, ceramics went through grain boundary shift from high energy to the low energy state and decreased the porosity while increased the density of coating structure [25], [36]. Porosity and density of coating are inversely related with each other. Shrinkage of grain boundaries hindered the diffusion of oxygen to the composite surface and invigorated the interlocking of coating and specimen. Fig. 5e shows that the density of sintered coating was increased with 48 % reduction in porosity measured via ImageJ software. The reduction in porosity after sintering suggests that  $\text{SiO}_2$  was solidified and it also sealed up the cracks which were appeared during the shrinkage of coating.

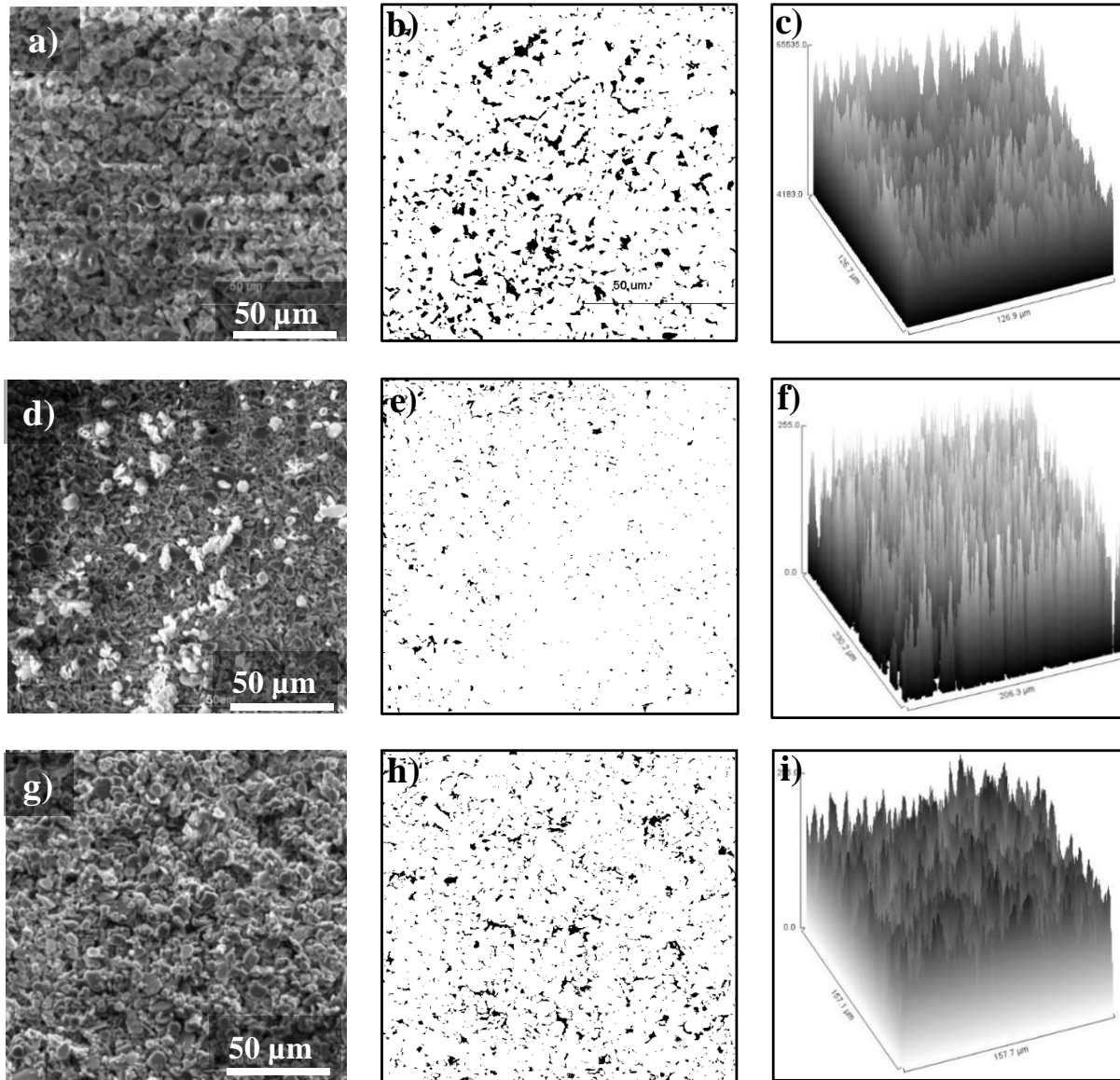


Fig. 21: SEM image, binary image, and surface plot of the: (a-c) as-deposited coating; (d-f) coating after sintering at 1073 K; and (g-i) coating after ISOT testing of 3h, respectively.

Fig. 5c depicts that as-deposited coating exhibited a surface profile with negative skewness. This indicates a surface with broad peaks and sharp valleys. Broad peaks and sharp valleys allowed heat waves to reside at maxima that triggered the grain boundary shift,  $\text{SiO}_2$  formation, and interface development with enough heat absorption. After sintering, the surface roughness ( $R_a$ ) increased from  $4.55 \mu\text{m}$  to  $7.03 \mu\text{m}$  (measured via SurfCharJ plugin of ImageJ). Surface profile indicated sharp peaks and broad valley profile that reflects surface structure as a good thermal barrier. The

developed dense microstructure of  $\text{Al}_2\text{O}_3$  ceramic layer enhanced the thermal shock resistance of the coating.

Direct sintering of the coating at 1073 K after vacuum drying resulted in less mass loss as compared to stepwise sintering approach. It was noted that heating at 873 K resulted in rapid degradation of carbon fibres and the corresponding weight loss was 29%. On the contrary, sintering at 1073 K resulted in lesser mass loss (i.e., 10.98%) which is attributed to the interface development. Isothermal oxidation test (ISOT) was conducted at 1273 K as a test for interfacial stability. No mass change was observed during the ISOT and the coating maintained its integrity with only a little change in coating thickness probably due to further densification of interface. Coating thickness varied from 259 to 258.3  $\mu\text{m}$  measured via ImageJ software. Exposure to oxidizing environment at constant temperature for several hours results in compressive stresses and microcracks. Fig. 5h shows that the dissipation of stresses results in surface microcracks. Although microcrack formation raised the surface porosity to 17%, destructive crack propagation was not observed. The  $\text{Al}_2\text{O}_3$  coating proved itself as a good barrier for application at 1273 K.

### **Thermal shock resistance of $\text{Al}_2\text{O}_3$ coating**

Fig. 6a is the camera image of as-deposited  $\text{Al}_2\text{O}_3$  coated C/SiC composite. Fig. 6b shows camera image of thermal shock tested specimens after 26 thermal cycles. Fig. 6b indicates that the surface roughness was increased after 5–26 thermal cycles. Heat-wave-impact not only altered the surface roughness but also increased the surface porosity.

Fig. 6c. shows an obvious interlock interface after 26 thermal shock cycles which is beneficial to overcome thermal stresses originated because of mismatch of CTE between coating and C/SiC specimen. Compared with the morphology of before thermal shock testing cross section, some changes are observed. As at the interface, microcracks and pores were appeared near the interface and within the coating. Although no mass loss was observed which proves that the sintering at 1073 K integrated the interface with necessary microstructure. Surface porosity before and after DTS testing was measured 2.45% and 8% (measured via ImageJ software package) respectively.



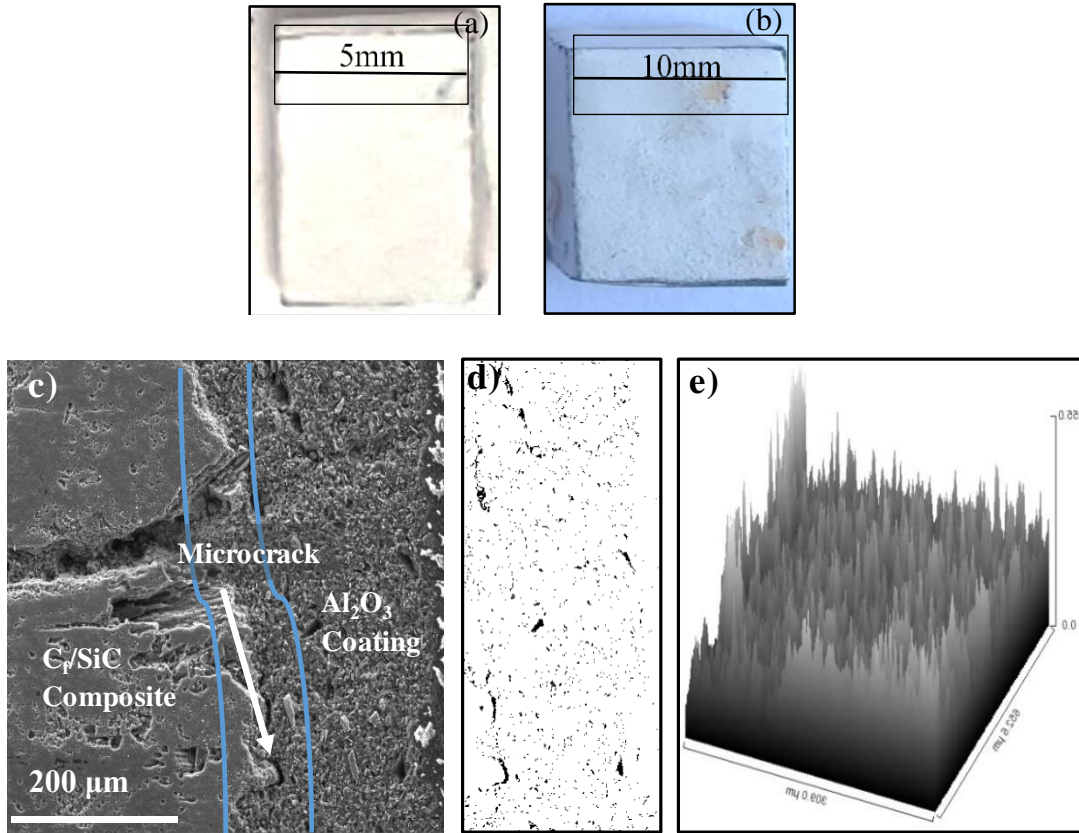


Fig 6. Camera image of coating & cross-sectional analysis: (a) as-deposited; (b) after 26 thermal shock cycles; (c) SEM of cross section after 26 thermal cycles; (d) binary image of interface; and (e) surface plot of interface, respectively.

It was noted that at high temperature, CTE mismatch resulted in tensile stresses throughout the coating structure i.e. at interface and surface. This effect became significant as the number of thermal cycles increased and promoted the production of cracks within the coating [7], [10], [16], [37], [38]. At 1273 K coefficient of thermal expansion (CTE) for  $\text{Al}_2\text{O}_3$  will become  $10.1 \times 10^{-6}/\text{K}$ , that reduces the thermal stresses due to volume expansion. The thermal conductivity of  $\text{Al}_2\text{O}_3$  decreases (from 20 W/ m·K at room temperature) as the temperature goes up (to 5 W/m·K at 1273 K); this leads to tensile stresses in the coating and originates the cracks [39]. Crack propagation and crack network control can only be possible with effective interface formation during sintering process.

Fig. 7a shows the morphology developed after 5 thermal chock cycles. Fig. 7b shows that the coating remained smooth with the development of a few micropores and microcracks. It should be in consideration that thermal cycling needs coating with moderate CTE so that it will neither peel

off nor rupture. We addressed all these challenges during the development of Al<sub>2</sub>O<sub>3</sub> coating. Slurry based coatings are dense in nature because of high solid loading of suspension. Fig. 7c shows the microstructure analysis via ImageJ of thermal shock tested specimen, it shows a porous surface with uniform distribution of pores and small microcracks.

Horizontal microcracks developed due to thermal stresses. Certain growth of microcracks is prerequisite to dissipate the thermal stresses evolved during thermal cycling. Crack formation over the surface facilitated to overcome the CTE mismatch. SurfChar J analysis showed a surface with positive skewness and kurtosis greater than 3, these features enhanced the heat rejection capability of the coating surface. Positive skewness indicates sharp peaks with broad valleys. Positive skewed surface increased the rate of heat rejection during thermal shock cycling.

During thermal cycling, coating maintained its integrity without any weight change. Although some depressions and ditches were observed on the surface, those were produced because of heat wave impact. The surface roughness was increased after thermal shock testing of specimens (i.e. Ra= 16 μm).

It has been noted that grain size and thermal stresses are interrelated with each other; coating structured with the size range of 1–5 μm have good ductility and high fracture toughness [14]. The coating retained its integrity without any observable crack formation (Fig. 6b). Densified microstructure with 15–20% porosity showed high resistance to crack growth and propagation. Meanwhile, the presence of pore spaces increases the compliance and counteracts the CTE mismatch. Wang et al. [18] developed a nanostructured YSZ coating having 9% porosity which peeled off only after 11 thermal cycles. Although, the coating thickness and thermal shock procedure also affect the thermal shock resistance. Our findings are in compliance with the coatings developed via expensive deposition techniques such as EB-CVD, APS, and PVD.

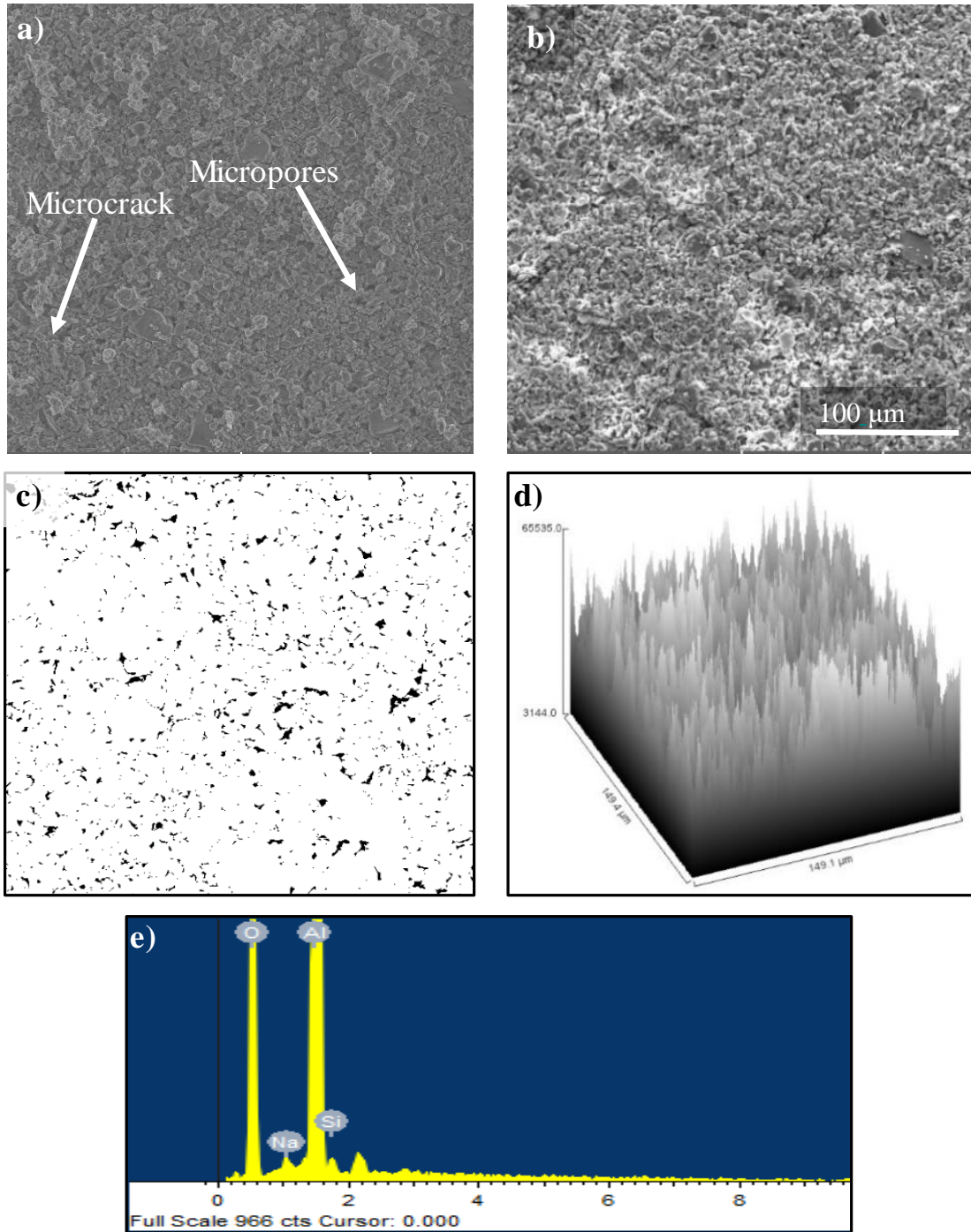


Fig. 7. Microstructure analysis of thermal shock tested  $\text{Al}_2\text{O}_3$  coated C/SiC specimen via SEM and ImageJ analysis: (a) SEM after 5 thermal cycles; (b) SEM image; (c) binary image ( $50\ \mu\text{m}$ ); (d) surface plot; (e) EDS analysis; after 26 thermal shock cycles respectively.

## **Conclusions**

Al<sub>2</sub>O<sub>3</sub>-based ETBC has been successfully applied via a versatile and inexpensive dip-coating process on C/SiC composite. A sintering temperature of 1073 K was found suitable for interface development. The mass change rate during sintering process was about 0.033 mg/s.cm<sup>2</sup> which is quite small as compared to expensive thermal spray processes. It was found that a single layer coating system with 8–17% porosity, 7–16 μm surface roughness and 250–350 μm coating thickness showed excellent thermal shock resistance over the 26 thermal cycles in air at 1273 K. The cross-sectional analysis revealed that self-healing oxide layer was developed at the interface that ensured smooth CTE transition. Hence, Al<sub>2</sub>O<sub>3</sub>-coatings can be applied for the jet engine and land-based turbines.

## **Acknowledgements**

The authors would like to thank Engr. Naveed Ali and Mr. Qamaruddin for their support to complete the characterization study of the project. Authors would also acknowledge the financial support by Higher Education Commission of Pakistan (HEC) under project NRPU-2801.

## References

- [1] C. Zhang *et al.*, “Thermal shock resistance of a 2D-C/SiC composite and its damage mechanisms,” *Advances in Applied Ceramics*, vol. 112, no. 8, pp. 499–504, Nov. 2013.
- [2] Y. Xu and T. Gao, “Optimizing thermal-elastic properties of C/C-SiC composites using a hybrid approach and PSO algorithm,” *Materials*, vol. 9, no. 4, 2016.
- [3] P. Kumar and V. K. Srivastava, “Tribological behaviour of C/C–SiC composites—A review,” *Journal of Advanced Ceramics*, vol. 5, no. 1, pp. 1–12, 2016.
- [4] Z.-Q. qiao YAN *et al.*, “Oxidation behavior of oxidation protective coatings for C/C-SiC composites at 1 500 ??C,” *Transactions of Nonferrous Metals Society of China (English Edition)*, vol. 19, no. 1, pp. 61–64, 2009.
- [5] A. Wank *et al.*, “Diffusion barrier coatings for graphite , C / C and C / SiC racks in vacuum heat treatment or high temperature brazing processes,” pp. 5–8, 2005.
- [6] Z. S. Khan *et al.*, “Thermal cycling behavior and hot corrosion performance of the plasma sprayed Er<sub>2</sub>Si<sub>2</sub>O<sub>7</sub> coatings deposited on Cf/SiC composites,” *Journal of Asian Ceramic Societies*, vol. 3, no. 1, pp. 123–129, 2014.
- [7] J. I. Federer, “Alumina base coatings for protection of SiC ceramics,” *Journal of Materials Engineering*, vol. 12, no. 2, pp. 141–149, Jun. 1990.
- [8] N. Asok Kumar and S. R. Kale, “Numerical simulation of steady state heat transfer in a ceramic-coated gas turbine blade,” *International Journal of Heat and Mass Transfer*, vol. 45, no. 24, pp. 4831–4845, 2002.
- [9] P. Prapamonthon, H. Xu, W. Yang, and J. Wang, “Numerical Study of the Effects of Thermal Barrier Coating and Turbulence Intensity on Cooling Performances of a Nozzle Guide Vane,” *Energies*, vol. 10, no. 3, p. 362, 2017.
- [10] A. K. Krella, A. T. Sobczyk, A. Krupa, and A. Jaworek, “Thermal resistance of Al<sub>2</sub>O<sub>3</sub> coating produced by electrostatic spray deposition method,” *Mechanics of Materials*, vol. 98, pp. 120–133, 2016.
- [11] T. Mori, S. Yamada, and N. Iwata, “Effects of suspension properties on the microstructure of Al<sub>2</sub>O<sub>3</sub> coatings deposited onto macroporous SiC substrate,” *Surface and Coatings Technology*, vol. 326, pp. 1–10, Oct. 2017.
- [12] S. Das, “STUDY OF PLASMA SPRAY ALUMINA - ALUMINIDE COMPOSITE COATING ON METALS Doctor of Philosophy Satrughna Das Department of Physics

STUDY OF PLASMA SPRAY ALUMINA - ALUMINIDE COMPOSITE Satrughna Das  
Department of Physics,” National University of Technology Rourkela, India, 2007.

- [13] A. Z. Abidin *et al.*, “EVALUATION OF ALUMINA AS PROTECTIVE COATING FOR CARBON FIBERS IN MAGNESIUM-BASED COMPOSITES,” 2015.
- [14] A. K. Krell, A. T. Sobczyk, A. Krupa, and A. Jaworek, “Thermal resistance of Al<sub>2</sub>O<sub>3</sub> coating produced by electrostatic spray deposition method,” *Mechanics of Materials*, vol. 98, pp. 120–133, 2016.
- [15] M. Aparicio and A. Durán, “Yttrium silicate coatings for oxidation protection of carbon-silicon carbide composites,” *Journal of the American Ceramic Society*, vol. 83, no. 6, pp. 1351–1355, Dec. 2000.
- [16] G. Di Girolamo, F. Marra, C. Blasi, E. Serra, and T. Valente, “Microstructure, mechanical properties and thermal shock resistance of plasma sprayed nanostructured zirconia coatings,” *Ceramics International*, vol. 37, no. 7, pp. 2711–2717, 2011.
- [17] J. Zhang, Q. Fu, P. Zhang, J. Qu, R. Yuan, and H. Li, “Surface & Coatings Technology Rapid heat treatment to improve the thermal shock resistance of ZrO<sub>2</sub> coating for SiC coated carbon / carbon composites,” *Surface & Coatings Technology*, vol. 285, pp. 24–30, 2016.
- [18] W. Q. Wang, C. K. Sha, D. Q. Sun, and X. Y. Gu, “Microstructural feature, thermal shock resistance and isothermal oxidation resistance of nanostructured zirconia coating,” *Materials Science and Engineering: A*, vol. 424, no. 1–2, pp. 1–5, May 2006.
- [19] Accuratus Ceramic Corporation, “99.5% Alumina Material Properties,” p. 8865, 2013.
- [20] S. Ramasamy, S. N. Tewari, K. N. Lee, R. T. Bhatt, and D. S. Fox, “Slurry based multilayer environmental barrier coatings for silicon carbide and silicon nitride ceramics - I. Processing,” *Surface and Coatings Technology*, vol. 205, no. 2, pp. 258–265, 2010.
- [21] X. LU, D. YAN, Y. YANG, Y. DONG, J. HE, and J. ZHANG, “Phase evolution of plasma sprayed Al<sub>2</sub>O<sub>3</sub>-13%TiO<sub>2</sub> coatings derived from nanocrystalline powders,” *Transactions of Nonferrous Metals Society of China*, vol. 23, no. 10, pp. 2951–2956, 2013.
- [22] A. Larsson and S. Ruppel, “Microstructure and properties of CVD  $\gamma$ -Al<sub>2</sub>O<sub>3</sub> coatings,” *International Journal of Refractory Metals and Hard Materials*, vol. 19, no. 4–6, pp. 515–522, Jul. 2001.

- [23] S. Ramasamy *et al.*, “EBC Development for Hot-Pressed Y<sub>2</sub>O<sub>3</sub>/Al<sub>2</sub>O<sub>3</sub> Doped Silicon Nitride Ceramics EBC development for hot-pressed EBC development for hot-pressed Y<sub>2</sub>O<sub>3</sub>/Al<sub>2</sub>O<sub>3</sub> doped silicon nitride ceramics doped silicon nitride ceramics EBC development for hot-pressed Y<sub>2</sub>O<sub>3</sub>/Al<sub>2</sub>O<sub>3</sub> doped silicon nitride ceramics,” *Chemical & Biomedical Engineering Faculty Publications. Materials Science & Engineering A*, vol. 6105, no. 527, pp. 21–22, 2010.
- [24] M. Zhang *et al.*, “Microstructure and oxidation resistant behavior of Er<sub>2</sub>Si<sub>2</sub>O<sub>7</sub> and Er<sub>2</sub>Si<sub>2</sub>O<sub>7</sub>/LaMgAl<sub>11</sub>O<sub>19</sub> coatings deposited on C f/SiC composites by APS at 1723 K,” *Journal of Alloys and Compounds*, vol. 709, pp. 24–30, Jun. 2017.
- [25] S. K. Khaja-abdul, “SLURRY BASED COATINGS ON SILICON BASED CERAMICS,” Cleveland State University, Cleveland OHIO, 2006.
- [26] C. Courtois, J. Desmason, H. T, and S. E. E. S. Cedex, “Protection against oxidation of C / SiC composites : oxidation behaviour of CVD TiB<sub>2</sub> coated substrates,” *Journal De Physique Iv*, vol. 3, 1993.
- [27] Z. Yan, F. Chen, X. Xiong, P. Xiao, and B. Huang, “Thermal Shock Resistance of SiC/Si—Mo Multilayer Oxidation Protective Coating for Carbon/Carbon Silicon Carbide Composites.”
- [28] C. Huo *et al.*, “Improving the oxidation resistance under thermal shock condition of SiC-coated C/C composites with refined SiC grain size using ferrocene,” *Surface and Coatings Technology*, vol. 316, pp. 39–47, Apr. 2017.
- [29] B. Zou *et al.*, “Oxidation protection of carbon/carbon composites with a plasma-sprayed ZrB<sub>2</sub>-SiC-Si/Yb<sub>2</sub>SiO<sub>5</sub>/LaMgAl<sub>11</sub>O<sub>19</sub> coating during thermal cycling,” *Journal of the European Ceramic Society*, vol. 35, no. 7, pp. 2017–2025, 2015.
- [30] L. Cheng, Y. Xu, L. Zhang, and R. Gao, “Oxidation Behaviour of C/SiC Composites with a Si-Zr Coating from Room Temperature to 1500 °C,” in *High Temperature Ceramic Matrix Composites*, FRG: Wiley-VCH Verlag GmbH & Co. KGaA, 2006, pp. 268–273.
- [31] B. Baufeld, O. van der Biest, and H.-J. Raetzer-Scheibe, “Thermal and Mechanical Properties of Zirconia Coatings Produced By Electrophoretic Deposition,” *Advanced Ceramic Coatings and Interfaces Ii*, vol. 28, no. 3, pp. 3–10, 2008.

- [32] J. P. Zhang, Q. G. Fu, J. L. Qu, L. Zhuang, P. P. Wang, and H. J. Li, "An inlaid interface of carbon/carbon composites to enhance the thermal shock resistance of SiC coating in combustion environment," *Surface and Coatings Technology*, vol. 294, pp. 95–101, 2016.
- [33] J. Roy, S. Chandra, S. Das, and S. Maitra, "OXIDATION BEHAVIOUR OF SILICON CARBIDE - A REVIEW," *Review Advance Materials Sciences*, vol. 38, pp. 29–39, 2014.
- [34] I. Krenkel, "Carbon fibre reinforced silicon carbide composites (C/SiC, C/C-SiC)," *Handbook of ceramic composites*, pp. 117–148, 2005.
- [35] H. P. Oxidation, C. Vapor, and D. Silicon, "of Carbide," vol. 90, pp. 1386–1390, 1989.
- [36] X. J. Lu and P. Xiao, "Constrained sintering of YSZ/Al<sub>2</sub>O<sub>3</sub> composite coatings on metal substrates produced from eletrophoretic deposition," *Journal of the European Ceramic Society*, vol. 27, no. 7, pp. 2613–2621, 2007.
- [37] M. Oksa, "Nickel and iron based HVOF thermal spray coatings for high temperature corrosion protection in biomass fired power plant boilers," *JULK AISIJA - UTGIVARE*, 2015.
- [38] P. K. Panda, T. S. Kannan, J. Dubois, C. Olagnon, and G. Fantozzi, "Thermal shock and thermal fatigue study of ceramic materials on a newly developed ascending thermal shock test equipment," *Science and Technology of Advanced Materials*, vol. 3, no. 4, pp. 327–334, 2002.
- [39] J. F. Justin and A. Jankowiak, "AL03-08 1 High Temperature Materials Ultra High Temperature Ceramics: Densification, Properties and Thermal Stability."